Institut für Angewandte Photophysik

Fachrichtung Physik

Fakultät Mathematik und Naturwissenschaften

Technische Universität Dresden

Electronic Coupling Effects and Charge Transfer between Organic Molecules and Metal Surfaces

Dissertation

zur Erlangung des akademischen Grades

Doktor der Naturwissenschaften

(Doctor rerum naturalium)

vorgelegt von

Roman Forker

geboren am 15. Mai 1981 in Räckelwitz

Dresden 2010

**TECHNISCHE
UNIVERSITÄT
DRESDEN**

Eingereicht am 15.09.2009

1. Gutachter: Prof. Dr. Karl Leo

2. Gutachter: Prof. Dr. Moritz Sokolowski

Verteidigt am 12.01.2010

Abstract

We employ a variant of optical absorption spectroscopy, namely *in situ* differential reflectance spectroscopy (DRS), for an analysis of the structure–properties relations of thin epitaxial organic films. Clear correlations between the spectra and the differently intense coupling to the respective substrates are found. While rather broad and almost structureless spectra are obtained for a quaterrylene (QT) monolayer on Au(111), the spectral shape resembles that of isolated molecules when QT is grown on graphite. We even achieve an efficient electronic decoupling from the subjacent Au(111) by inserting an atomically thin organic spacer layer consisting of hexa-*peri*-hexabenzocoronene (HBC) with a noticeably dissimilar electronic behavior. These observations are further consolidated by a systematic variation of the metal substrate (Au, Ag, and Al), ranging from inert to rather reactive. For this purpose, 3,4,9,10-perylene-tetracarboxylic dianhydride (PTCDA) is chosen to ensure comparability of the molecular film structures on the different metals, and also because its electronic alignment on various metal surfaces has previously been studied with great intensity. We present evidence for ionized PTCDA at several interfaces and propose the charge transfer to be related to the electronic level alignment governed by interface dipole formation on the respective metals.

Kurzfassung

Zur Analyse der Struktur–Eigenschafts-Beziehungen dünner, epitaktischer Molekülfilme wird *in situ* differentielle Reflexionsspektroskopie (DRS) als Variante der optischen Absorptionsspektroskopie verwendet. Klare Zusammenhänge zwischen den Spektren und der unterschiedlich starken Kopplung zum jeweiligen Substrat werden gefunden. Während man breite und beinahe unstrukturierte Spektren für eine Quaterrylen (QT) Monolage auf Au(111) erhält, ist die spektrale Form von auf Graphit abgeschiedenem QT ähnlich der isolierter Moleküle. Durch Einfügen einer atomar dünnen organischen Zwischenschicht bestehend aus Hexa-*peri*-hexabenzocoronen (HBC) mit einem deutlich unterschiedlichen elektronischen Verhalten gelingt sogar eine effiziente elektronische Entkopplung vom darunter liegenden Au(111). Diese Ergebnisse werden durch systematische Variation der Metallsubstrate (Au, Ag und Al), welche von inert bis sehr reaktiv reichen, untermauert. Zu diesem Zweck wird 3,4,9,10-Perylentetracarbonsäuredianhydrid (PTCDA) gewählt, um Vergleichbarkeit der molekularen Filmstrukturen zu gewährleisten, und weil dessen elektronische Anordnung auf verschiedenen Metalloberflächen bereits eingehend untersucht worden ist. Wir weisen ionisiertes PTCDA an einigen dieser Grenzflächen nach und schlagen vor, dass der Ladungsübergang mit der elektronischen Niveauanpassung zusammenhängt, welche mit der Ausbildung von Grenzflächendipolen auf den entsprechenden Metallen einhergeht.

Für Andrea.

Contents

1   Introduction and Motivation

Research carried out in the field of organic thin films is essentially stimulated by their potential applications in molecular electronics. Layers a few nanometers thick piled up in sequential structures are especially interesting since organic photovoltaic devices (OPVDs) [1, 2] and organic light-emitting diodes (OLEDs) [3] based on this architecture have already been realized and are expected to gain market share rapidly [4].* Present devices comprise a multitude of junctions between molecular layers and metal or conductive polymer electrodes as well as between adjacent layers consisting of different molecular species [5–9]. One declared goal is to keep the thickness(es) of the active region(s) reasonably low since the operational capabilities are determined, amongst other things, by the rather inefficient charge carrier transport [10] and by the creation and separation of excitons whose diffusion lengths are rather small [11–13]. Consequently, interface effects compete with the bulk properties of the utilized substances to a large extent. Epitaxial growth [14–21] facilitates the formation of well-defined interfaces allowing one to explore processes that are specifically hard to address by other fabrication procedures, typically leading to polycrystalline or even amorphous structures. The resulting structural imperfections, especially grain boundaries, can obscure the underlying physical interface effects.

The examples named above for up-to-date devices rely on the conversion between light and free charge carriers. The interplay of electronic and optical properties of organic semiconductors is therefore of accentuated importance. While the lowest unoccupied molecular orbital (LUMO) and the highest occupied molecular orbital (HOMO) of the respective molecular compounds can be examined using photoelectron spectroscopies [22–26], optical spectroscopy can clarify the light absorption and emission behavior.

In addition, optical techniques are especially suitable for structural examinations, as they are mostly non-intrusive and can hence be applied *in situ* as a real-time monitoring method for the growth of molecular thin films, even in the case where the optical properties of the organic materials are not of great significance, such as in organic field effect transistors (OFETs) [27, 28].

---

*The actual state of affairs on "market strategies for organic and printable electronics" can be found, e.g., in the magazine '+PlasticELECTRONICS' (IntertechPira, ISSN 1755-9693).

The alignment of conjugated disk-like (i.e., planar) molecules is one of the key factors for the performance of associated organic electronics devices. As a consequence of the anisotropic growth behavior of many molecules, it is often observed that the physical properties, such as the conductivity or the absorption of light, are also highly anisotropic and can differ substantially between ordered arrays and amorphous structures of the same compound. Let us consider here the formation of molecular stacks being arranged either parallel or perpendicular to the substrate surface, as visualized in Figure 1.1. If the conductivity (enhanced by an efficient orbital overlap) along such stacks is greater than in the other directions, the desired molecular arrangement would be upstanding (i.e., "edge-on") for a conducting channel in an OFET with source and drain electrodes at both ends of the stacks, whereas flat-lying (i.e., "face-on") molecules sandwiched between top- and bottom-electrodes would be preferred for an OPVD [29]. Yet, in all scenarios contacts between the active organic region(s) and metal or conductive polymer electrodes for charge injection are inevitable.
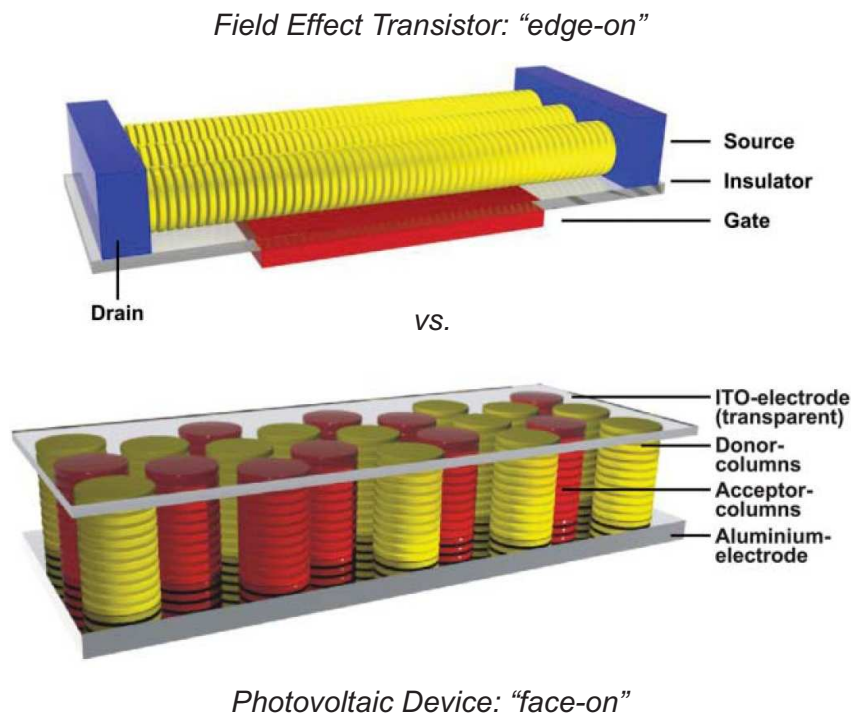
Figure 1.1: Schematic illustration of two prototypical organic electronics devices. Disks represent the planar molecules which are assumed to exhibit a cofacial stacking growth behavior in these examples. Reproduced from Ref. [29].

When molecules are adsorbed on metals, several processes may occur that originate from the interaction of the molecular orbitals with the electron distribution in the proximity of the surface [22]. These processes are often summarized as metal–organic "coupling" and can take one or more of the following forms:

- Rearrangement of the electron cloud right outside the metal surface, i.e., metal electrons are "pushed back",

- Chemical interaction, i.e., strong influence on the molecular and surface geometries resulting in the formation of (covalent) bonds,

- Formation of interface states that can emerge in the previously forbidden energy gap of the molecule,

- Charge transfer (CT) between substrate and adsorbate,

and possibly a few more [22]. The strength and in part also the direction of these effects as well as the interplay between them strongly depend on the molecule–metal combination and, additionally, on the specific structure(s) formed.

In this thesis, we intend to convince the reader that the impact of these phenomena can be probed by means of surface-sensitive optical absorption spectroscopy. After a short introduction of the molecular substances and a review of the basic principles of the methods and devices employed (Chapter 2) we will present and discuss our experimental results. In Chapter 3, particular attention will be paid to the interface formation between a planar polycyclic aromatic hydrocarbon (PAH) and a variety of surfaces ranging from conductive to insulating. A hierarchical order shall be established for the observed electronic coupling strength, and we will provide evidence that this coupling can be efficiently suppressed by an atomically thin spacer layer comprising exclusively organic molecules of a different kind. A consequent extension of the optical observation of electronic coupling shall be provided in Chapter 4 for a variety of metal surfaces ranging from inert to rather reactive. There, we present clear optical evidence for ionized aromatic molecules at several interfaces and propose the CT to be related to the electronic level alignment governed by interface dipole formation on the respective metals. Finally, general conclusions drawn from our results will be summarized in Chapter 5.

2   Materials, Methods, and Devices

At the beginning of this chapter, the molecular species used in this thesis shall be briefly introduced. The optical properties of organic molecules composed of benzene units will further be explained. Given that the primary technique used in this work is the optical differential reflectance spectroscopy (DRS), we will provide a basic description of thin film optics. Some mathematical derivations will be inevitable in order to establish a link between the DRS and the complex dielectric function of a thin organic film deposited on some sort of substrate. The experimental realization will be specified in detail and briefly compared to related techniques. Supporting methods for the structural and electronic characterization of thin organic films will also be introduced. Epitaxial thin film growth will be elucidated and classified at the end.

2.1   Molecular Substances Used

Since the frequent use of acronyms is inconsistent among different communities and sometimes rather arbitrary, a compilation of the chemical formulas as well as of the most important classifiers for the molecular species used here is shown in Table 2.1.
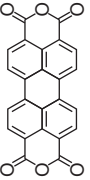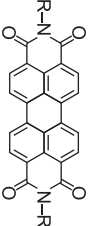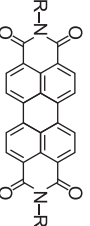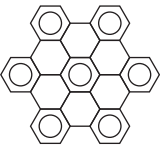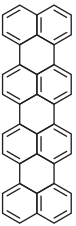
From the vast number of organic molecules, these examples were chosen due to their outstanding ability to form epitaxial thin films on a variety of substrates. Especially 3,4,9,10-perylenetetracarboxylic dianhydride (PTCDA)* has emerged as *the* prototypical compound for many researchers working in the field of organic epitaxy [15, 19, 32–40]. Likewise, hexa-*peri*-hexabenzocoronene (HBC)[†] and quaterrylene (QT)[‡] are known to grow as highly ordered films, which is strongly desired for the investigation of specific interface effects, but also for the fabrication of organic–organic heterostructures [41–43]. All three of them exhibit dissimilar optical and electronic properties and very different crystal structures [44–46], which is particularly beneficial for the investigation

---

*Purchased from Sigma-Aldrich.

[†]Supplied by Prof. K. Müllen, MPI für Polymerforschung, Mainz, Germany.

[‡]Purchased from Dr. W. Schmidt, Institut für PAH-Forschung, Greifenberg, Germany.

Table 2.1: List of the molecular substances used in this work. Some of the principle classifiers are given in order to help identify the molecules in a variety of databases. The nomenclature is sometimes inconsistent, thus only selected full names are listed. In contrast, CAS* numbers are unique.

Acronym	Full Name(s)	CAS* Number	Sum Formula	Molecular Weight	Skeletal Formula
PTCDA	3,4,9,10-perylenetetracarboxylic dianhydride	128-69-8	$C_{24}H_8O_6$	$392.3 \, \mathrm{g \cdot mol^{-1}}$	
PBI†	N,N'-bis(1-hexylheptyl)-3,4:9,10-perylene-bis(dicarboximide)	110590-84-6	$C_{50}H_{62}N_2O_4$	$755.0 \, \mathrm{g \cdot mol^{-1}}$	R = 1-hexylheptyl
DBPI‡	N,N'-bis(2,5-di-*tert*-butylphenyl)-3,4:9,10-perylenebis(dicarboximide)	83054-80-2	$C_{52}H_{50}N_2O_4$	$767.0 \, \mathrm{g \cdot mol^{-1}}$	R = 2,5-di-*tert*-butylphenyl
HBC	hexa-*peri*-hexabenzocoronene hexabenzo[bc,ef,hi,kl,no,qr]coronene 1,12:2,3:4,5:6,7:8,9:10,11-hexabenzocoronene	190-24-9	$C_{42}H_{18}$	$522.6 \, \mathrm{g \cdot mol^{-1}}$	
QT	quaterrylene benzo[1,2,3-cd:4,5,6-c'd']diperylene	188-73-8	$C_{40}H_{20}$	$500.6 \, \mathrm{g \cdot mol^{-1}}$	

*The Chemical Abstracts Service (CAS) is a division of the American Chemical Society (ACS). See also http://www.chemicalbook.com/.
†From Kircher *et al.* (Ref. [30]) for comparison.
‡From Ford *et al.* (Ref. [31]) for comparison.

of the structure–properties-relations, being one of the central aspects of surface science. Two molecules derived from PTCDA, namely PBI and DBPI, are also shown in Table 2.1 for the sake of completeness, since their previously published optical absorption spectra are later shown in comparison.

PTCDA and HBC were purified prior to usage via several cycles of temperature-gradient vacuum sublimation (CreaPhys GmbH, Dresden, Germany). QT was used as provided. After transferring the materials to the growth chamber, they were thoroughly degassed *in vacuo* for several hours slightly below the sublimation temperature. This procedure allows for an efficient and reliable removal of remaining contaminants with smaller molecular weight.

2.2   Optical Properties of Organic Molecules

2.2.1   Aromatic Compounds

An outstanding property of carbon (electron configuration: $1s^2\ 2s^2\ 2p^2$) is its ability to form hybrid orbitals that can be described as a mixture of the $2s$ and $2p$ atomic orbitals, possibly with different respective contributions. In "sp^2-hybridization", a total of 3 sp^2-orbitals per C atom is formed which are all aligned in one plane, while 1 p-orbital perpendicular to this plane is left over (therefore named p_z-orbital). The sp^2-orbitals of adjacent atoms in a molecule overlap, thereby forming σ-bonds (Figure 2.1). The electrons in the p_z-orbital may also overlap, thereby forming π-bonds which can delocalize across adjacent sp^2-hybridized atoms ("conjugation"). Due to the degeneracy of the p_z- and sp^2-orbitals of adjacent C atoms, energy level splitting occurs in a conjugated molecule (Figure 2.2). The energy gap between bonding and antibonding σ-orbitals is rather large. In contrast, the energy level splitting of the π-orbitals
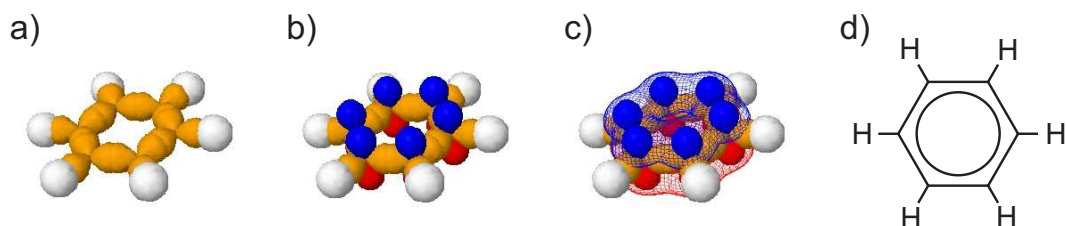
Figure 2.1: Schematic depiction of the aromaticity of benzene, C_6H_6, in pseudo-3D perspective. **a)** The 18 sp^2-hybridized orbitals of the 6 C atoms in hexagonal (planar) alignment. These so-called σ-bonds are drawn in yellow, while H atoms are sketched as white spheres. **b)** The 6 remaining p_z-orbitals of the C atoms are perpendicular to the molecular plane and drawn here in red and blue, representing different signs of the wavefunctions. **c)** Illustration of the delocalization of the p_z-orbitals forming so-called π-bonds. **d)** Simplified chemical formula where the ring in the hexagon symbolizes the delocalized π-electron system. The images (a) - (c) were created using the open-source software Jmol [47], available at `http://jmol.sourceforge.net/`.
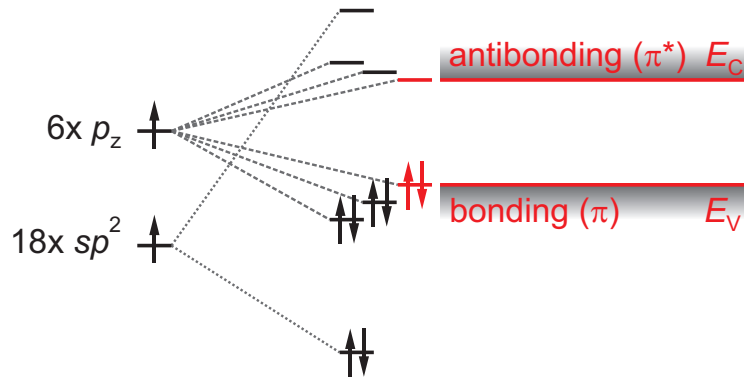
Figure 2.2: Schematic energy diagram of benzene, cf. Ref. [48]. The 6 C atoms possess 1 p_z-orbital and 3 sp^2-hybridized orbitals each. Due to the degeneracy of these states, energy level splitting occurs when orbitals of adjacent C atoms overlap, thereby forming bonds. The lowest-energy (bonding) molecular orbitals are occupied with electrons, while higher-energy (antibonding) orbitals are unoccupied. E_V and E_C indicate the analogy to the valence band energy and the conduction band energy, respectively, in extended conjugated systems.

is much smaller and noticeably closer to the visible spectral range. In general, this energy gap becomes even smaller for increasing conjugation, i.e., for larger, more delocalized π-systems [48]. A conjugated "chain" of 6 C atoms may form a closed hexagon saturated by 6 hydrogen atoms. Such a planar C_6H_6 molecule (benzene, cf. Figure 2.1) is the basic building block of "aromatic" dyes, compare Table 2.1. Many characteristics of aromatic compounds can be attributed to the behavior of semiconductors because of their characteristic energy level structure forming bands in extended systems. Especially planar molecules are often characterized by a preferential arrangement of the conjugated framework in molecular aggregates, i.e., in the bulk crystal structure. This may lead to a coplanar alignment of the π-electron system with the possibility to enhance the intermolecular coupling, causing remarkable electronic and optical properties. For instance, the charge transport is often band-like in organic crystals, with high mobilities even at room temperature [10, 49]. The corresponding optical properties shall be explained in the following, where we establish a link between the behavior of single molecules and aggregates.

2.2.2   Single Molecules

A first approach to a thorough optical characterization of a molecular compound would be the determination of its "single" molecule properties. When we speak of *single* molecules or *monomers*, we actually mean an ensemble of *isolated* units. Isolation can be obtained, for example, by embedment in a liquid droplet or in a solid matrix at very low temperatures [50, 51], or in standard solvents at moderate temperatures and low concentrations [52, 53]. Even

in very dissimilar environments, one often observes a characteristic spectral "fingerprint" of the molecular absorption (cf. Figure 2.3) whose origin shall be explained in the following. The argumentation given here follows closely the reasoning proposed in Ref. [49].
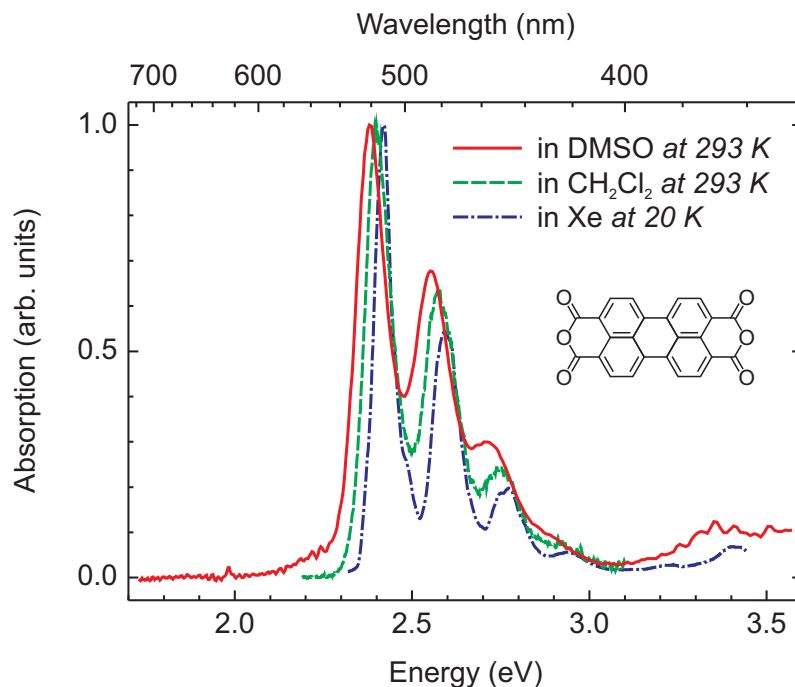
Figure 2.3: Normalized optical absorption data of PTCDA (inset: skeletal formula) in different environments, as reported before: *(i)* dissolved in dimethyl sulfoxide (DMSO) at $293\,\mathrm{K}$ [52], *(ii)* dissolved in dichloromethane (DCM, CH_2Cl_2) at $293\,\mathrm{K}$ [53], and *(iii)* embedded in a Xe-matrix at $20\,\mathrm{K}$ (photoluminescence excitation spectrum) [51]. The corresponding peak positions are shifted with respect to each other on the energy scale ("solvent shift"). Furthermore, one can see that here the full width at half maximum (FWHM) in standard solvents at room temperature is comparable to that in a noble gas matrix at a much lower temperature. This confirms that the respective experimental data shown here represent the spectral fingerprint of *isolated* molecules.

Born-Oppenheimer Approximation.   Due to their much lower mass, the electrons are able to almost immediately follow the movements (oscillations) of the nuclei in an atom or a molecule. For this reason, one can separate the total wavefunction Ψ_{total} into its electronic ψ_{e} and nuclear (vibrational χ_{v}, and rotational φ_{r}) components:

$$\Psi_{\mathrm{total}} = \psi_{\mathrm{e}}\chi_{\mathrm{v}}\varphi_{\mathrm{r}} \quad . \tag{2.1}$$

The total energy can thus simply be expressed as a summation:

$$\begin{aligned} E_{\mathrm{total}} &= \langle\Psi_{\mathrm{total}}|\,\mathcal{H}_{\mathrm{e}} + \mathcal{H}_{\mathrm{v}} + \mathcal{H}_{\mathrm{r}}\,|\Psi_{\mathrm{total}}\rangle \\ &= E_{\mathrm{e}} + E_{\mathrm{v}} + E_{\mathrm{r}} \quad . \end{aligned} \tag{2.2}$$

This is a basic expression of the Born-Oppenheimer approximation. For the molecules used in this work, the magnitudes of these energies are roughly $E_e : E_v : E_r \approx 1\,\mathrm{eV} : 0.1\,\mathrm{eV} : 0.001\,\mathrm{eV}$ [49]. The vibrational oscillations will hence be visible as additional features in the optical spectra.

Molecular Orbitals and Excitons. The molecular orbitals are derived from the square of the electron wavefunctions. In the view of the probability interpretation, they represent the spatial distribution density of the electrons. In the electronic ground state the orbitals are filled, or occupied, beginning with the energetically lowest levels (compare Hund's rules). The highest occupied molecular orbital is denoted HOMO, the lowest unoccupied molecular orbital is abbreviated LUMO. If one electron is added to (or removed from) a molecule in closed-shell configuration, the resulting singly occupied molecular orbital is labeled SOMO, meaning that the unpaired electron causes the molecule to be a free radical. HOMO and LUMO are also called the frontier orbitals, and their difference in energy $E_{\mathrm{LUMO}} - E_{\mathrm{HOMO}} = E_{\mathrm{gap}}$ is sometimes called electronic band gap, although strictly speaking, bands do not occur until a spatially extended solid is formed. Here, we would like to emphasize that the optical absorption process involves the creation of an exciton, i.e., a quasi-particle consisting of an excited electron and a hole that exhibit a binding energy via attractive Coulomb forces [48]. Hence, the electronic gap E_{gap} and the optical gap E_{opt} differ by the exciton binding energy E_{exc} which can sometimes be as large as $1\,\mathrm{eV}$ [54]. Moreover, diffusion, confinement, and dielectric screening of excitons in a solid are naturally to be distinguished from those of electrons and holes, rendering a direct comparison of electronic and optical properties rather difficult if not impossible.

Franck-Condon Principle and Stokes Shift. The schematic potential energy curves of a molecular ground state S_0 and excited state S_1 are depicted in Figure 2.4. In the quantum mechanical picture, vibrational levels are associated with these potential energies and their wavefunctions are those of harmonic oscillators. Electronic transitions (absorption or emission, respectively) occur on very fast time scales of usually $\lesssim 10^{-15}\,\mathrm{s}$. During the transition, the nuclei essentially remain at their initial positions, as their rearrangement typically lasts $10^{-13}\,\mathrm{s}$ due to their much greater mass. After the transition, the equilibrium positions of the nuclei may be shifted, indicated by a displacement of the potential energy curves with respect to the configuration coordinate Q in Figure 2.4. For ordinary diatomic molecules, Q simply refers to the internuclear separation. Since electronic transitions are usually completed before the rearrangement of the nuclei (i.e., ΔQ is practically zero), they are denoted as vertical transitions, cf. Figure 2.4. This rule is known as the Franck-Condon principle [49]. The absolute squared values of the overlap integral $|\langle \chi_{v'} | \chi_{v''} \rangle|^2$
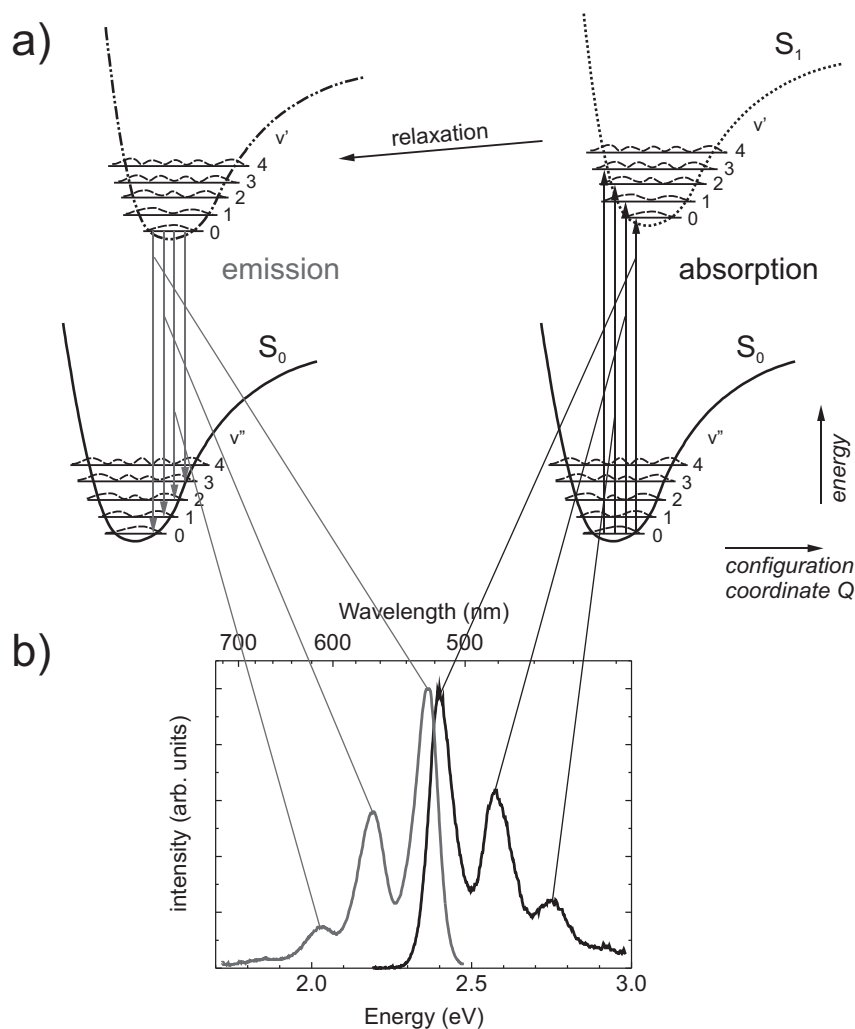
Figure 2.4: Illustration of the Franck-Condon principle for the $S_0 \rightarrow S_1$ transition, after Ref. [49]. **a)** Simplified scheme of the absorption and emission processes. The vibrational levels are denoted by v′ and v″, respectively, and the corresponding probability functions are sketched. The excited potential S_1 is shifted in the configuration coordinate(s) with respect to the ground state S_0. After excitation, a geometrical relaxation of the nuclei (and hence S_1) takes place, yielding slightly different potential energy curves and causing a Stokes shift (energy difference between 0–0 transitions in absorption and emission). **b)** Resulting optical spectra with one *effective* vibronic progression measured for PTCDA dissolved in CH_2Cl_2 [53]. Note the almost perfect mirror symmetry between absorption and emission. Compared to the absorption energies, the Stokes shift of $\approx 0.035\,eV$ is rather small and typical for such perylene derivatives.

between the wavefunctions of initial and final vibrational levels v′ and v″, respectively, are proportional to the intensity of each particular transition. They are called Franck-Condon factors and determine the intensity distribution of the vibronic progression. According to Kasha's rule, the electronic distribution quickly relaxes to the lowest vibrational level, so that 0–N transitions are actually observed, with N being an integer number. By combining these two

principles, one can readily explain that absorption and emission are often symmetric in energy, presuming (almost) equal shapes of the ground and excited state potential energy curves, as seen in Figure 2.4.

The vibrational structure of PTCDA monomers isolated in helium nanodroplets ($T \approx 0.38$ K) has been spectrally resolved in laser-induced fluorescence experiments [50]. The $S_1 \leftarrow S_0$ transition was shown to consist of a large number of peaks with different intensities. A convolution of these lines with Gaussian functions and a shift on the energy scale yielded a spectral shape similar to the room temperature absorption measurements depicted in Figure 2.3. Thereby the origin of the apparent single *effective* vibrational mode of $\Delta E_{\text{vibron}} \approx 0.17$ eV of dissolved PTCDA monomers could be explained.

The lifetime of the excited states is typically in the range of 10^{-11} to 10^{-7} s. During this time, the nuclei can relax geometrically toward their new equilibrium positions, thereby reducing the total energy. For this reason, the 0–0 transition of the emission is usually at a slightly lower energy than that of the absorption, and the energy difference between both is called Stokes shift.

2.2.3   Molecular Aggregates

In this section, we will qualitatively elucidate the principles of molecular aggregation on the basis of a *physical dimer*, i.e., a pair of (identical) molecules close to each other that do not form chemical bonds between themselves.

The Hamiltonian of a physical dimer consists of the separate Hamiltonians for each isolated molecule $\mathcal{H}_1$ and $\mathcal{H}_2$ plus a term V_{12} representing the intermolecular interaction potential:

$$\mathcal{H} = \mathcal{H}_1 + \mathcal{H}_2 + V_{12} \quad . \tag{2.3}$$

Assuming only weak interaction between both molecules, one can assume the dimer wavefunction to be the product of the respective monomer wavefunctions. The ground state can be approximated as:

$$\Psi_{\text{g}} = \psi_1 \psi_2 \quad . \tag{2.4}$$

Consequently, the ground state energy is just:

$$
\begin{aligned}
E_{\text{g}} &= \langle \psi_1 \psi_2 | \, \mathcal{H} \, | \psi_1 \psi_2 \rangle \\
&= E_1 + E_2 + \langle \psi_1 \psi_2 | \, V_{12} \, | \psi_1 \psi_2 \rangle \\
&= E_1 + E_2 + W \quad ,
\end{aligned}
\tag{2.5}
$$

where E_1 and E_2 are the corresponding monomer ground state energies. W denotes the Coulomb binding energy, which is negative for dimers, but positive for excimers, i.e., a physical dimer with one of the molecules being electronically excited and the other one in the ground state.
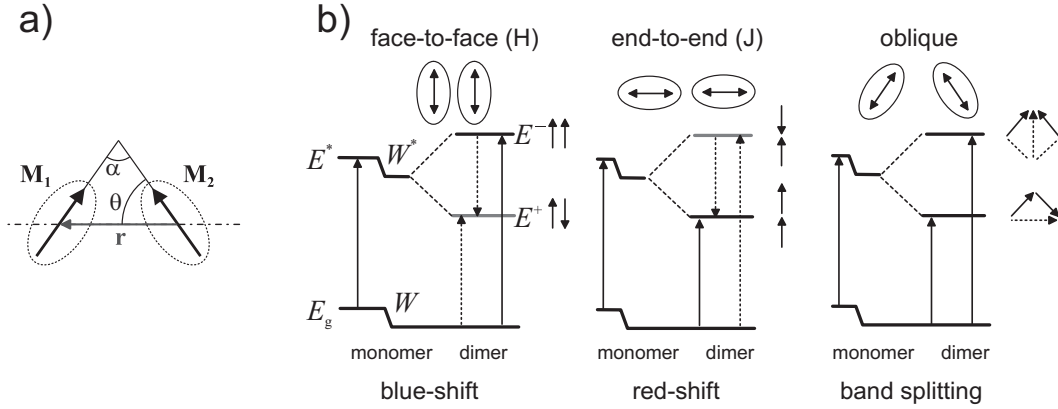
Figure 2.5: Physical dimer according to the Kasha model (schematic). **a)** Geometrical description of the orientations of the two transition dipole moments $\mathbf{M}_1$ and $\mathbf{M}_2$ with respect to each other. **b)** Energy shifts for different orientations of the transition dipole moments of the dimer. The exciton band splitting energy is given by $|E^+ - E^-| = 2|\beta|$. The dimer state Ψ_+ is lower in energy when $\beta < 0$. A parallel alignment of $\mathbf{M}_1$ and $\mathbf{M}_2$ leads to only one dipole allowed transition (solid arrows). This causes an effective blue-shift (H-aggregate) or red-shift (J-aggregate), respectively, compared to the monomer. Non-parallel alignment leads to band splitting. After Refs. [49, 55–57].

A particular excited state of molecule i shall be called ψ_i^*. Because of the interaction energy V_{12}, the excitation energy is shared by both molecules, and the excited wavefunction of the dimer can be written as:

$$\Psi_\pm = c_1 \cdot \psi_1^* \psi_2 \pm c_2 \cdot \psi_1 \psi_2^* \quad . \tag{2.6}$$

For indistinguishable molecules, the normalization conditions are fulfilled by $c_1 = c_2 = 1/\sqrt{2}$, and the monomer excitation energies are identical ($E_1^* = E_2^*$). The excited state energies of the dimer are given by

$$E^\pm = E_1^* + E_2 + W^* \pm \beta \quad , \text{with} \tag{2.7}$$

$$W^* = \langle \psi_1^* \psi_2 | V_{12} | \psi_1^* \psi_2 \rangle \quad , \tag{2.8}$$

$$\beta = \langle \psi_1^* \psi_2 | V_{12} | \psi_1 \psi_2^* \rangle \quad . \tag{2.9}$$

The exciton band splitting energy follows from

$$\left| E^+ - E^- \right| = 2 \left| \beta \right| \quad , \tag{2.10}$$

$$2\beta = \frac{2 \left| \mathbf{M} \right|}{r^3} \left(\cos \alpha + 3 \cos^2 \theta \right) \quad , \tag{2.11}$$

with the geometrical parameters illustrated in Figure 2.5 and a transition dipole moment $\mathbf{M}$ of the dimer expressed by $\mathbf{M}^\pm = 1/\sqrt{2} \, (\mathbf{M}_1 \pm \mathbf{M}_2)$ [49, 55]. Thus, positive and negative values of β are possible, and the splitting may even vanish for specific orientations.

In this simplified reflection of the physical dimerization, we have neglected configuration interactions. It becomes nevertheless obvious that the specific

geometrical arrangement of molecular transition dipole moments considerably affects the optical response of dimers and higher oligomers.

As a consequent further step it is necessary to provide a description of excitations in molecular crystals. However, due to the manifold possibilities of crystal structures and molecular orientations in the respective unit cells, a general extension of the above argumentation to larger aggregates is not trivial. However, a convenient approach to the understanding of optical processes in a molecular bulk is offered by the class of quasi-one-dimensional crystals, which in fact applies to a variety of planar aromatic molecules.

Monomer–Dimer–Oligomer Transition; Quasi-One-Dimensional Crystals.
For certain molecular species, such as PTCDA, the π-orbital overlap and hence the intermolecular interactions along one crystal direction are significantly stronger than along others. Consequently, the crystal can be regarded as a two-dimensional array of one-dimensional stacks. In this special case we speak of quasi-one-dimensional crystals with strong intermolecular orbital overlap, which can be favorably addressed by established exciton theories [52, 58–61]. From the simple Kasha model, it already follows that a linear chain of N identically oriented molecules leads to N-fold degenerate excited levels in the non-interacting case. This degeneracy is lifted when an interacting term $V \neq 0$ is introduced for the crystal phase, causing the formation of a band of N states with a maximum energy spread of $4\,|\beta|$, where β is the interaction energy between adjacent molecules (compare Equation (2.9)) [49]. In comparison with the band splitting energy of the dimer being $2\,|\beta|$, we see that half the splitting of an infinite chain is already present in the dimer. Other classical molecular crystals, such as anthracene, possess completely different structures with a pronounced three-dimensional character exhibiting much weaker intermolecular overlap [62]. The resulting lowest excited states are called Frenkel excitons, being essentially localized on one molecule, while charge transfer (CT) excitons are only needed for the description of higher excited states or charge carrier generation processes. For larger overlap, such as in quasi-one-dimensional crystals, the Frenkel and CT exciton energies come closer to each other and can mix rather strongly. This situation has been investigated in linear molecular chains of variable length [61], in which exciton confinement effects are provided by the surface states, i.e., states localized at the outermost molecules of the chains. The calculations revealed that for comparatively small numbers of chain links ($N \geq 5$) the bulk contribution dominates the surface states.

These theoretical considerations found an excellent experimental confirmation in the direct observation of the formation of solid state excitons in ultrathin PTCDA films grown on cleaved mica by Holger Proehl *et al.* [32]. Figure 2.6 depicts an *in situ* differential reflectance spectroscopy (DRS) measurement for various film thicknesses of PTCDA, recorded during film growth.

As DRS is a variant of optical absorption spectroscopy (compare Section 2.3), the spectra can be directly attributed to the absorption behavior.

Up to a surface coverage of 1 monolayer (ML) the spectra posses monomeric character, comparable to absorption spectra of PTCDA in solution (cf. Figure 2.3), and simply rise in magnitude with increasing film thickness. The three visible peaks (at 2.34, 2.52, and $\approx 2.70\,\text{eV}$, respectively) are attributed to the energetically lowest (i.e., $S_0 \rightarrow S_1$) transition, separated by a vibronic progression of $\Delta E_{\text{vibron}} \approx 0.18\,\text{eV}$. Above 1 ML, a significant development sets in: The ratio of the heights of Peak 1 ($2.34\,\text{eV}$) and Peak 2 ($2.52\,\text{eV}$) changes considerably and the entire spectrum broadens noticeably. From there on, the spectral shape transforms into that of the well-known (polycrystalline) film structure. Beside those spectral modifications, it is intriguing to highlight the occurrence of two isosbestic points in the set of DR spectra in the thickness range from 1.0 to 1.9 ML. Isosbestic points indicate a characteristic equilibrium between two absorbing species [63], thereby yielding valuable information about the growth mode of PTCDA: In a layer-by-layer growth regime, these two species represent the monomer and the stacked dimer, respectively.

An explanatory approach requires the comprehension of the anisotropy of the PTCDA crystal. The herringbone structure typically found in ultrathin PTCDA films corresponds to the (102) crystal plane (often with a rather in-
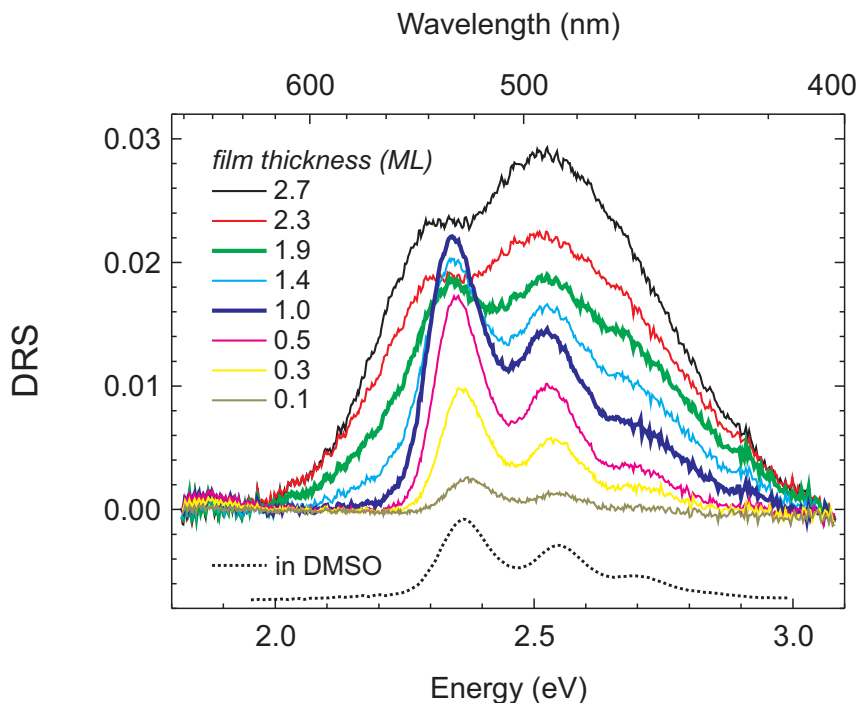

Figure 2.6: Thickness-dependent *in situ* differential reflectance spectra (DRS) of PTCDA on mica illustrating the monomer–dimer transition. For comparison, an absorption spectrum of PTCDA dissolved in DMSO [52] is shown (dotted curve, not to scale). Adapted from Ref. [32].

significant misfit) in which the molecules lie flat [44]. The distance between the nearest in-plane neighbors' centers of gravity is quite large (≈ 12 Å). Therefore, the interactions between the transition dipoles are rather weak and even a densely packed PTCDA monolayer behaves optically like an ensemble of monomers. Consequently, monomeric spectra are observed up to 1 ML coverage. On the other hand, strong interactions of the overlapping π-electron systems occur in the stacking direction, because the adjacent molecular planes are separated by as little as 3.2 Å [44]. This π–π-interaction is overwhelmingly stronger than the in-plane interaction, and hence PTCDA can be described as a quasi-one-dimensional crystal. These circumstances readily explain the observed spectral changes once the second PTCDA layer starts to grow: Every molecule added to the second layer will contribute a dimeric signature to the spectrum while simultaneously eliminating a monomeric signature. From ≈ 2 ML on, the DR spectra grow proportionally to the thickness again, now being appreciably broadened. Peak 1 rapidly undergoes a rather strong redshift which is accomplished at a coverage of ≈ 4 ML (not shown here). The comparatively broad Peak 2 splits into two bands (at 2.48 and 2.57 eV, respectively) which remain at nearly constant energetic positions with further increasing film thickness above 4 ML. Starting from a thickness of ≈ 2.3 ML, the high energy shoulder of the spectra at 2.7 eV becomes less pronounced and completely smears out when a coverage of 4 ML is reached. Thus, the dimer–oligomer transition is essentially completed at 4 ML coverage. With further increasing film thickness, the spectral shape is fully comparable to the spectra known for much thicker PTCDA films (compare Refs. [15, 58, 64, 65]).

In summary, the PTCDA film growth on mica is a well-understood prototype of the physical monomer–dimer–oligomer transition in the solid state, which is considered to be a reference for the interpretation of the optical behavior of other molecular systems, as well.

2.3   Differential Reflectance Spectroscopy (DRS)

The differential reflectance spectroscopy (DRS) compares the reflected intensity of a substrate covered with an adsorbate of thickness d ($R(E, d)$) to that of the uncovered substrate ($R(E, 0)$) via

$$\mathrm{DRS}(E, d) := \frac{R(E, d) - R(E, 0)}{R(E, 0)} \quad . \tag{2.12}$$

For the motivation of DRS as a useful measuring quantity we would like to follow the derivation proposed by McIntyre and Aspnes [66]. We will demonstrate mathematically for the special case of transparent substrates that the DRS is a variant of optical absorption spectroscopy. With this goal in mind, we will express the above definition in terms of Fresnel coefficients. Subsequently,

we will make some useful approximations that allow for a separation of the real and imaginary part of the adsorbate dielectric function and henceforth a more convenient interpretation of the DRS.

2.3.1   Optical Functions and Fresnel Coefficients

The classical description of the interaction between electromagnetic waves and matter is realized by Maxwell's equations [67, 68], given here in SI units:

$$\nabla \cdot \mathbf{D} = \rho_{\text{free}} \qquad or \qquad \nabla \cdot \mathbf{E} = \frac{\rho_{\text{total}}}{\epsilon_0} \quad , \tag{2.13}$$

$$\nabla \cdot \mathbf{B} = 0 \quad , \tag{2.14}$$

$$\nabla \times \mathbf{E} = -\frac{\partial \mathbf{B}}{\partial t} \quad , \tag{2.15}$$

$$\nabla \times \mathbf{H} = \frac{\partial \mathbf{D}}{\partial t} + \mathbf{j}_{\text{free}} \qquad or \qquad \nabla \times \mathbf{B} = \mu_0 \epsilon_0 \frac{\partial \mathbf{E}}{\partial t} + \mu_0 \mathbf{j}_{\text{total}} \quad . \tag{2.16}$$

Here, ρ_{free} means the *free* charge density ($\rho_{\text{total}} = \rho_{\text{bound}} + \rho_{\text{free}}$), and $\mathbf{j}_{\text{free}}$ denotes the *free* current density ($\mathbf{j}_{\text{total}} = \mathbf{j}_{\text{bound}} + \mathbf{j}_{\text{free}}$). For small field strengths (linear optics), the electric displacement field $\mathbf{D}$ can be related to the electric field $\mathbf{E}$ via

$$\mathbf{D} \stackrel{\text{general}}{=} \epsilon_0 \mathbf{E} + \mathbf{P} \stackrel{\text{linear, isotropic}}{=} \epsilon_0 \epsilon_r \mathbf{E} \quad , \tag{2.17}$$

where $\mathbf{P} = \epsilon_0 (\epsilon_r - 1) \mathbf{E}$ is called the polarization of the material. The magnetic flux density $\mathbf{B}$ can be expressed in terms of the magnetic field $\mathbf{H}$ and the magnetization $\mathbf{M}$ as:

$$\mathbf{B} \stackrel{\text{general}}{=} \mu_0 (\mathbf{H} + \mathbf{M}) \stackrel{\text{linear, isotropic}}{=} \mu_0 \mu_r \mathbf{H} \quad . \tag{2.18}$$

With the help of the following expressions

$$\rho_{\text{bound}} = -\nabla \cdot \mathbf{P} \quad , \tag{2.19}$$

$$\mathbf{j}_{\text{bound}} = \nabla \times \mathbf{M} + \frac{\partial \mathbf{P}}{\partial t} \tag{2.20}$$

one can prove that the alternatively derived formulation of Maxwell's equations in terms of *total* charge and current densities given in Equations (2.13) and (2.16) are indeed equivalent. Inserting Equation (2.17) into Equation (2.16) yields:

$$\nabla \times \mathbf{H} = \epsilon_0 \epsilon_r \frac{\partial \mathbf{E}}{\partial t} + \mathbf{j}_{\text{free}}$$

$$= \epsilon_0 \epsilon_r \frac{\partial \mathbf{E}}{\partial t} + \sigma \mathbf{E} \quad , \tag{2.21}$$

$$\text{with} \quad \mathbf{j}_{\text{free}} = \sigma \mathbf{E} \quad . \tag{2.22}$$

In the last step we have introduced Ohm's law. For the sake of simplicity, we consider here linear, isotropic materials whose permittivity $\epsilon = \epsilon_0\epsilon_r$ and permeability $\mu = \mu_0\mu_r$ are constant scalars. A more rigorous treatment of anisotropic molecular crystals would of course require a tensorial formulation. As an *ansatz* for Equation (2.21) we choose the (macroscopic) electric field of a plane wave with frequency ω and complex wave vector $\hat{\mathbf{k}}$:

$$\mathbf{E}\left(\mathbf{r}, t\right) = \mathbf{E}_0 \cdot \exp\left(-i\left[\hat{\mathbf{k}} \cdot \mathbf{r} - \omega t\right]\right) \quad . \tag{2.23}$$

Since $\partial\mathbf{E}/\partial t = i\omega\mathbf{E}$ (and likewise $\partial\mathbf{B}/\partial t = i\omega\mathbf{B}$ from a similar *ansatz* for the magnetic field) is evidently fulfilled, we have

$$\begin{aligned}
\nabla \times \mathbf{H} &= \left(\epsilon_0\epsilon_r i\omega + \sigma\right)\mathbf{E} \\
&= i\omega\epsilon_0\left(\epsilon_r - i\frac{\sigma}{\omega\epsilon_0}\right)\mathbf{E} \\
&= i\omega\epsilon_0\left(\varepsilon' - i\varepsilon''\right)\mathbf{E} \\
&= i\omega\epsilon_0\hat{\varepsilon} \cdot \mathbf{E} \quad .
\end{aligned} \tag{2.24}$$

Here, we have introduced the (photon energy-dependent) complex dielectric function $\hat{\varepsilon}(\omega) = \varepsilon'(E) - i\varepsilon''(E)$. One can directly see that for a non-vanishing conductivity $\sigma \neq 0$ the imaginary part of the dielectric function ε'' is non-zero. Hence, in a conductive medium energy dissipates from the electromagnetic wave, which is called absorption. Applying the *curl* operator ($\nabla\times$) once more to Equation (2.15) leads to

$$\nabla \times \left(\nabla \times \mathbf{E}\right) = \nabla \times \left(-\frac{\partial\mathbf{B}}{\partial t}\right) = -i\omega\nabla \times \mathbf{B} \quad , \tag{2.25}$$

or, with Equations (2.18) and (2.24):

$$\nabla \cdot \left(\nabla \cdot \mathbf{E}\right) - \Delta \cdot \mathbf{E} = \omega^2\epsilon_0\hat{\varepsilon}\mu_0\mu_r\mathbf{E} \quad . \tag{2.26}$$

Assuming that $\rho_{\text{total}} = 0$ and hence $\nabla \cdot \mathbf{E} = 0$ (from Equation (2.13)) we can rearrange Equation (2.26):

$$\Delta \cdot \mathbf{E} + \omega^2\epsilon_0\hat{\varepsilon}\mu_0\mu_r\mathbf{E} = 0 \quad , \tag{2.27}$$

which is also referred to as Helmholtz's equation. In combination with the *ansatz* (2.23) we get

$$\hat{\mathbf{k}}^2 = \omega^2\epsilon_0\hat{\varepsilon}\mu_0\mu_r \quad . \tag{2.28}$$

The complex wave vector $\hat{\mathbf{k}}$ can be related to the complex index of refraction $\hat{n}$ via

$$\left|\hat{\mathbf{k}}\right| = \omega\sqrt{\epsilon_0\hat{\varepsilon}\mu_0\mu_r} = \frac{\omega}{c}\sqrt{\hat{\varepsilon}\mu_r} \overset{\mu_r=1}{=} \frac{2\pi}{\lambda}\hat{n} \quad . \tag{2.29}$$

Here, we consider media with a relative magnetic permeability of $\mu_r = 1$ being the usual case in the optical frequency range. The relation between $\hat{n}$ and $\hat{\varepsilon}$ can simply be expressed as follows:

$$\hat{n} = n - ik \tag{2.30}$$

$$\hat{\varepsilon} = \hat{n}^2 = \underbrace{n^2 - k^2}_{\varepsilon'} - i \cdot \underbrace{2nk}_{\varepsilon''} \quad . \tag{2.31}$$

In these equations $n \neq |\hat{n}|$ is the refractive index indicating the phase velocity, and $k \neq |\hat{\mathbf{k}}|$ is the (real) extinction coefficient, sometimes also called κ. Although this nomenclature is in some degree unfavorable as it might cause confusion, it seems to be more common in the literature and will hence be used throughout this work.

Despite the rather simple conversion between $\hat{n}$ and $\hat{\varepsilon}$, those two quantities are not quite identical. While *reflection* and *refraction* are commonly expressed in terms of $\hat{n}(\omega)$, the material's *absorption* behavior shall be described by $\hat{\varepsilon}(\omega)$. As we deal with driven harmonic oscillators as model systems in thin film optics (driving force = electromagnetic wave, oscillation = polarization of the material), their differential equations have to be treated according to Ref. [69]. They yield solutions in $\hat{\varepsilon}(\omega)$, and not in $\hat{n}(\omega)$. Thus, the discussion of the material's properties will focus on the complex dielectric function.

Having derived the primary quantities that describe the propagation of light in a medium, we can now move on to the description of electromagnetic waves traversing different media. Let us consider an *ideal*, i.e., entirely planar and abrupt interface between medium 1 and medium 2 being of different complex index of refraction $\hat{n}$. When electromagnetic waves cross this interface at an angle φ_1, as illustrated in Figure 2.7, several processes may occur: Part of
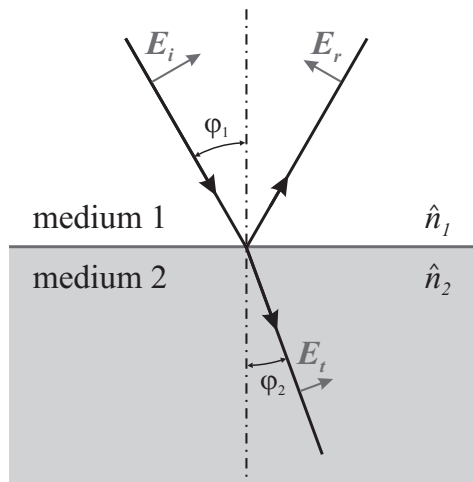

Figure 2.7: Two-dimensional sketch of the optical processes at an ideally planar interface between two media of different complex index of refraction $\hat{n}$. Electric field vectors are shown in *p*-polarization: E_i incident, E_r reflected, and E_t transmitted.

the intensity can be reflected (reflection R at the same angle φ_1) and refracted (transmission T at a different angle φ_2) at the interface, or henceforth absorbed (absorption A) in non-transparent media.[§] A mathematical description of these processes is obtained from the complex Fresnel coefficients for reflection ($\hat{r}$) and transmission ($\hat{t}$) between medium 1 and medium 2, given here for perpendicular incidence:

$$\hat{r}_{12} = \frac{\hat{n}_2 - \hat{n}_1}{\hat{n}_2 + \hat{n}_1} = -\hat{r}_{21} \quad , \tag{2.32}$$

$$\hat{t}_{12} = \frac{2\hat{n}_1}{\hat{n}_2 + \hat{n}_1} \neq \hat{t}_{21} \quad . \tag{2.33}$$

The first equation describes the ratio between reflected and incident, the second between transmitted and incident electric field. As we measure light intensities, we need to consider absolute squared values

$$\hat{R}_{12} = |\hat{r}_{12}|^2 = \hat{r}_{12}^* \cdot \hat{r}_{12} \quad , \tag{2.34}$$

$$\hat{T}_{12} = \left|\frac{\hat{n}_2}{\hat{n}_1}\right| \cdot |\hat{t}_{12}|^2 \quad . \tag{2.35}$$

The term $|\hat{n}_2/\hat{n}_1|$ in Equation (2.35) stems from the definition of the Poynting vector, given in SI units by:

$$\mathbf{S} = \mathbf{E} \times \mathbf{H} \quad . \tag{2.36}$$

$\mathbf{S}$ describes the energy flux in a medium. When an electromagnetic wave travels from medium 1 to medium 2, the amplitude of the Poynting vector scales as $S_1/S_2 = n_1/n_2$ because of energy conservation.[¶] The transmittance is symmetric ($T_{12} = T_{21}$), i.e., independent of the beam direction.

In the case of non-perpendicular incidence, the Fresnel coefficients are given by

$$\hat{r}_{\perp 12} = \frac{\hat{n}_1 \cos\varphi_1 - \hat{n}_2 \cos\varphi_2}{\hat{n}_1 \cos\varphi_1 + \hat{n}_2 \cos\varphi_2} \tag{2.37}$$

$$\hat{t}_{\perp 12} = \frac{2\hat{n}_1 \cos\varphi_1}{\hat{n}_1 \cos\varphi_1 + \hat{n}_2 \cos\varphi_2} \tag{2.38}$$

for s-polarization (TE), and

$$\hat{r}_{\parallel 12} = \frac{\hat{n}_2 \cos\varphi_1 - \hat{n}_1 \cos\varphi_2}{\hat{n}_2 \cos\varphi_1 + \hat{n}_1 \cos\varphi_2} \tag{2.39}$$

$$\hat{t}_{\parallel 12} = \frac{2\hat{n}_1 \cos\varphi_1}{\hat{n}_2 \cos\varphi_1 + \hat{n}_1 \cos\varphi_2} \tag{2.40}$$

[§]The general law of energy conservation is then $R + T + A = 1$. Note that A is not the optical density O.D. $= -\log(T/T_0)$ which is sometimes also called absorbance in the literature.

[¶] This can easily be checked for the absorption-free case (real quantities and $A = 0$):
$$R_{12} = \left(\frac{n_2 - n_1}{n_2 + n_1}\right)^2 . \qquad T_{12} = 1 - R_{12} = \frac{4n_2 n_1}{(n_2 + n_1)^2} = \frac{n_2}{n_1} \cdot \left(\frac{2n_1}{n_2 + n_1}\right)^2 = \left|\frac{n_2}{n_1}\right| \cdot |t_{12}|^2 .$$

for *p*-polarization (TM). If medium j is absorbing, the angle φ_j is actually complex [66]. However, an exact explanation of the physical meaning of complex angles seems to be generally avoided in the literature. Due to the cosine dependence in these expressions only minor deviations from Equations (2.32) and (2.33) arise from the small angle of incidence of $\varphi = 20\,^\circ$ ($\cos 20\,^\circ \approx 0.94$) in our setup, compare Section 2.3.5. We will therefore use the analytically simple formulas for perpendicular incidence.

2.3.2 Fabry-Pérot Interferometer and Linearization of DRS

An adequate description of the idealized three-phase system "vacuum / thin film / substrate" exhibiting planar and parallel interfaces is represented by the Fabry-Pérot interferometer depicted in Figure 2.8. Here, the substrate is regarded as semi-infinite, which means in practice that its extinction coefficient is sufficiently high to prevent the incident light from reaching the substrate back side.

On its way through medium 2 of thickness d, the electromagnetic wave is shifted in phase by

$$\hat{\beta} = 2\pi \frac{d}{\lambda} \hat{n}_2 \cos \varphi_2 \quad , \tag{2.41}$$

where λ is the vacuum wavelength. The summation of every single light path going back into medium 1 yields the "total" Fresnel coefficient

$$
\begin{aligned}
\hat{r} &= \hat{r}_{12} + \hat{t}_{12} \hat{t}_{21} \left[\hat{r}_{23} e^{-2i\hat{\beta}} + \hat{r}_{23}^2 \hat{r}_{21} e^{-4i\hat{\beta}} + \hat{r}_{23}^3 \hat{r}_{21}^2 e^{-6i\hat{\beta}} + \dots \right] \\
&= \hat{r}_{12} + \hat{t}_{12} \hat{t}_{21} \frac{\hat{r}_{23} \exp\left(-2i\hat{\beta}\right)}{1 + \hat{r}_{21} \hat{r}_{23} \exp\left(-2i\hat{\beta}\right)} \\
&= \frac{\hat{r}_{12} + \hat{r}_{23} \exp\left(-2i\hat{\beta}\right)}{1 + \hat{r}_{12} \hat{r}_{23} \exp\left(-2i\hat{\beta}\right)} \quad ,
\end{aligned}
\tag{2.42}
$$

since at an interface the law of energy conservation is simply

$$\hat{t}_{12} \hat{t}_{21} = 1 - \hat{r}_{12} \hat{r}_{21} \quad . \tag{2.43}$$

The Fresnel coefficients $\hat{t}_{12}$, $\hat{t}_{21}$, $\hat{r}_{12}$, $\hat{r}_{21}$ and $\hat{r}_{23}$ can be calculated using Equations (2.32) and (2.33). It is evident from Equation (2.42) that the exponential term results in an oscillating behavior of $\hat{r}$. Employing Equations (2.30) and (2.41) leads to

$$\exp\left(-2i\hat{\beta}\right) = \exp\left(-i \cdot 4\pi \frac{d}{\lambda} n_2 \cos \varphi_2\right) \cdot \exp\left(-4\pi \frac{d}{\lambda} k_2 \cos \varphi_2\right) \quad . \tag{2.44}$$
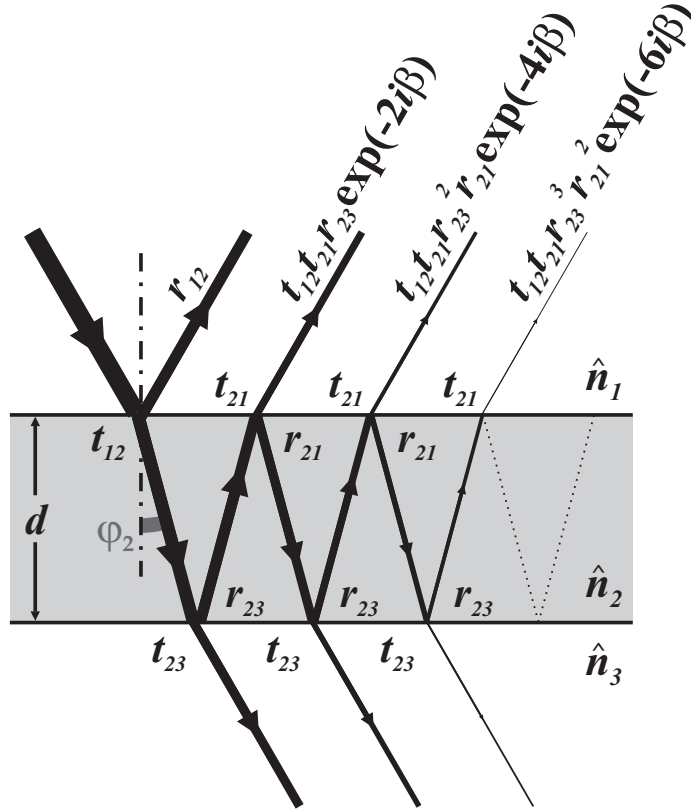
Figure 2.8: Multiple reflection and transmission at two parallel interfaces (Fabry-Pérot interferometer). The incident light beam is partially reflected and transmitted at the interfaces. The resulting reflected amplitude is then the summation of every single light path going back into medium 1. The gray shaded area represents the thin film with $\hat{n}_2$ and thickness d evaporated on a substrate with $\hat{n}_3$. Usually, $\hat{n}_1$ equals 1 (void). The complex character of $\hat{r}$, $\hat{t}$, and $\hat{\beta}$ is not explicitly indicated.

The first factor is responsible for interference effects as it is purely imaginary. It will cause $\cos(n_2 d)$ terms (or higher orders) in the total reflectance R. The visibility of interferences strongly depends on both, the coherence of the incident light and the quality of the thin film. As the product $n_2 \cdot d$ is very small for thin films, the oscillating frequency becomes very high and is in practice not observable. The second factor in Equation (2.44) is also known from the Beer-Lambert-Bouguer law. This exponential decay describes the dissipation of energy in an absorbing medium.

So far, no approximations were made in the above equations. However, an analytical expression of the total reflected intensity R would become quite complicated because absolute squared values are required. To overcome this problem it is useful to find an adequate simplification of Equation (2.42). For this purpose we expand the exponential term into a Taylor series:

$$\exp\left(-2i\hat{\beta}\right) \approx 1 - 2i\hat{\beta} + \dots \quad . \tag{2.45}$$

This expansion to terms of first order in $\hat{\beta}$ is in fact rather accurate provided that the thickness d of the adsorbate film is small in comparison to the incident wavelength (compare Equation (2.41)). Since our film thicknesses are typically in the range of $d \approx 0.3\,\text{nm}$ (nominal monolayer thickness), while wavelengths are normally $\lambda \gtrsim 300\,\text{nm}$, we can estimate their ratio as $d/\lambda \approx 1/1000 \ll 1$. Accordingly, Equation (2.42) simplifies to

$$\hat{r} \approx \frac{\hat{r}_{12} + \hat{r}_{23}\left(1 - 2i\hat{\beta}\right)}{1 + \hat{r}_{12}\hat{r}_{23}\left(1 - 2i\hat{\beta}\right)} \quad . \tag{2.46}$$

The reflectivity coefficient $\hat{r}_0$ of the bare substrate is obtained from Equation (2.42) by setting the adsorbate film thickness d to zero (i.e., $\hat{\beta} = 0$):

$$\hat{r}_0 = \frac{\hat{r}_{12} + \hat{r}_{23}}{1 + \hat{r}_{12}\hat{r}_{23}} \quad . \tag{2.47}$$

The ratio $\hat{r}/\hat{r}_0$ follows from Equations (2.46) and (2.47) by neglecting terms of second and higher orders in $\hat{\beta}$:

$$\frac{\hat{r}}{\hat{r}_0} \approx 1 + \frac{2i\hat{\beta}\hat{r}_{23}\left(\hat{r}_{12}^2 - 1\right)}{\left(\hat{r}_{12} + \hat{r}_{23}\right)\left(\hat{r}_{12}\hat{r}_{23} + 1\right)} \quad . \tag{2.48}$$

We can now come back to the Definition (2.12) of the DRS by inserting Equation (2.48). One has to multiply $\hat{r}/\hat{r}_0$ with its complex conjugate neglecting once more terms of second and higher orders in $\hat{\beta}$ (same approximation as above):

$$\text{DRS} = \frac{R - R_0}{R_0} = \frac{R}{R_0} - 1 = (\hat{r}/\hat{r}_0) \cdot (\hat{r}/\hat{r}_0)^* - 1 \tag{2.49}$$

$$\approx -8\pi \frac{d}{\lambda} \cdot \frac{\varepsilon_3'' \cdot (\varepsilon_2' - 1) + (1 - \varepsilon_3') \cdot \varepsilon_2''}{\varepsilon_3''^2 + (\varepsilon_3' - 1)^2} \quad , \tag{2.50}$$

or, equivalently:

$$\boxed{\text{DRS} \approx -8\pi \frac{d}{\lambda} \cdot \left[A \cdot \varepsilon_2'' + B \cdot (\varepsilon_2' - 1)\right]} \tag{2.51}$$

with the two spectral coefficients $A(E)$ and $B(E)$ determined solely by the substrate bulk dielectric function

$$A = \frac{(1 - \varepsilon_3')}{\varepsilon_3''^2 + (\varepsilon_3' - 1)^2} \quad , \tag{2.52}$$

$$B = \frac{\varepsilon_3''}{\varepsilon_3''^2 + (\varepsilon_3' - 1)^2} \quad . \tag{2.53}$$

Again, there is room for confusion concerning this nomenclature as it is not treated uniformly in the literature. Differences arise, e.g., from including or

leaving out the prefactor $8\pi d/\lambda$ (cf. Ref. [70]), but do generally not lower the significance of this linear approximation. Our Equations (2.52) and (2.53) are in accordance with Ref. [71], where $A(E)$ and $B(E)$ are also plotted versus photon energy E for various substrate materials.

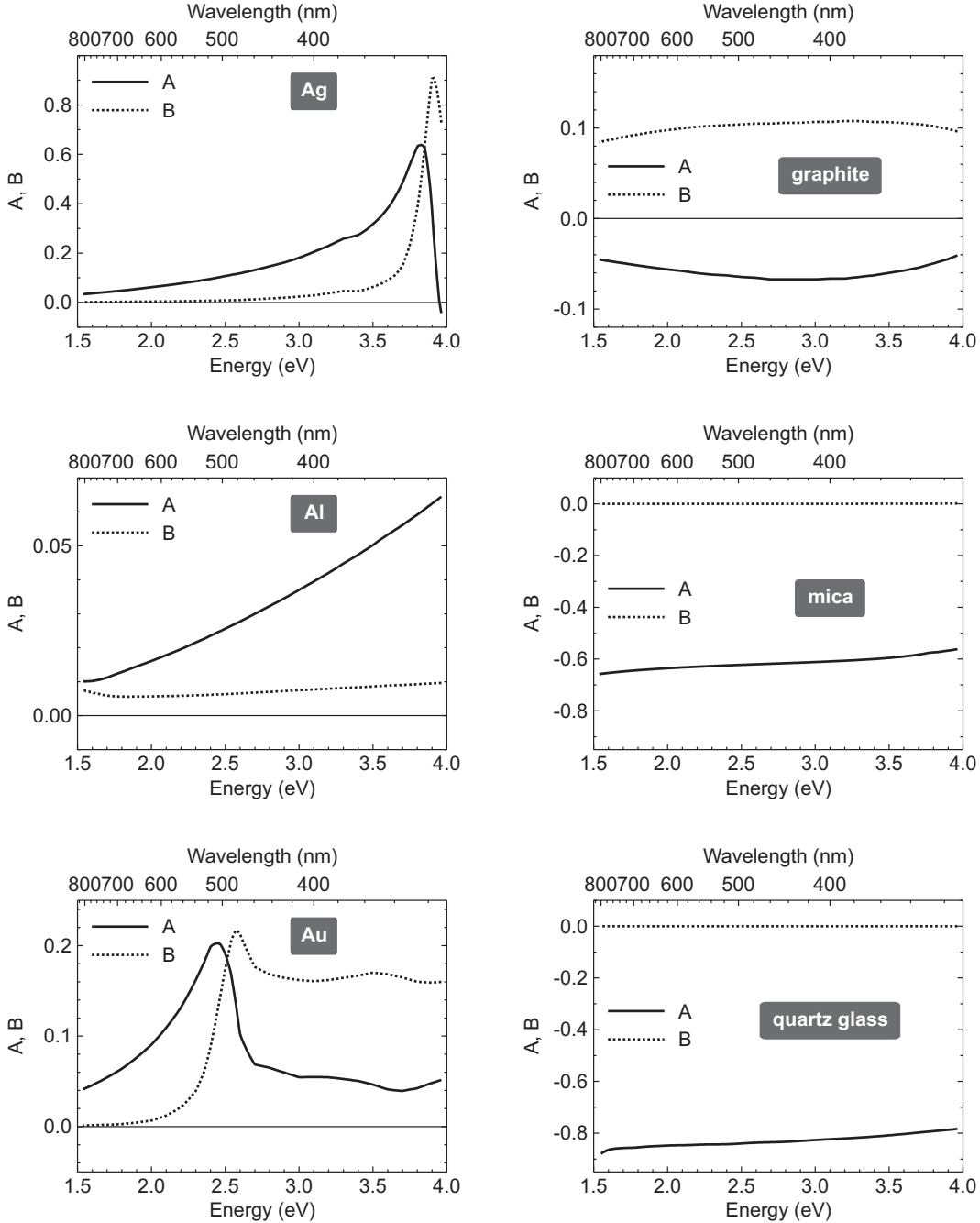**Figure 2.9:** The spectral coefficients A and B for the substrates used in this work based on experimental n and k values [72–75]. Note the different signs and magnitudes on the respective ordinate axes. For mica and quartz glass the condition $|B| \ll |A|$ holds in the entire spectral range shown here, while this is not necessarily valid for opaque substrates (with the exceptions of Ag and Au at low energies).

The spectral coefficients $A(E)$ and $B(E)$ for the substrates used in this work are depicted in Figure 2.9. One can immediately see that the condition $|B| \ll |A|$ is fulfilled in the optical frequency range for transparent substrates, such as mica and quartz glass, while this is not necessarily valid for opaque substrates. Consequently, Equation (2.51) can further be simplified to

$$\text{DRS} \approx -8\pi \frac{d}{\lambda} A \cdot \varepsilon_2'' \quad , \text{ for } |B| \ll |A| \quad . \tag{2.54}$$

Admittedly, the prerequisite of semi-infinite substrates is not met by transparent materials, and hence Equation (2.54) is not valid without restrictions. It can be shown, however, that the additional contribution of the substrate back side reflection leads to a reduction of the DRS which can be described by a scaling factor $\mathfrak{f}(E)$ [57], according to:

$$\text{DRS}_{\text{finite}} \approx \text{DRS}_{\text{semi-finite}} \cdot \mathfrak{f}(E) \quad , \tag{2.55}$$

with

$$\mathfrak{f}(E) = \frac{5 - n_3 + 7 \cdot n_3^2 - 3 \cdot n_3^3}{4 \cdot (1 + n_3) \cdot (1 + n_3^2)} \tag{2.56}$$

being derived from the substrate index of refraction $n_3 = n_3(E)$ [57]. As n_3 depends only weakly on the energy E for the special case of transparent materials considered here, it turns out that $\mathfrak{f}(E)$ is merely a constant factor, especially if not too broad spectral ranges are regarded. Note that $\mathfrak{f}(E)$ is independent of the substrate thickness as k_3 is assumed to be zero (transparent substrate).

Equation (2.54) further reveals that in principle DRS $\propto A$ for a given material (again for negligible B). Therefore, $|A|$ is a determining factor for the sensitivity of the DRS technique which will vary for different substrates. One can see in Figure 2.9 that $|A|$ can differ by an order of magnitude, even among the highly reflective metals. This makes aluminum a less favorable candidate for a high DRS sensitivity than silver or gold (cf. Section 4.4).

We have shown that for a given film thickness d and substrate dielectric function $\hat{\varepsilon}_3$ it may be possible to directly extract the imaginary part ε_2'' of the dielectric function of the adsorbate film. Since the latter characterizes the energy dissipation in a medium, the DRS is in fact a variant of optical absorption spectroscopy with the distinct advantage to be actually applicable to opaque substrates. Unfortunately, Equation (2.51) also demonstrates that the two optical functions ε_2' and ε_2'' can not be separated and extracted analytically whenever B is not negligible in comparison with A.

Consequently, a numerical extraction of ε_2' and ε_2'' (or, equivalently, n_2 and k_2) is the remaining option for opaque substrates. In the following, we will briefly introduce a model-free numerical algorithm recently developed in

our group for the purpose of a simultaneous determination of the adsorbate
optical functions on the basis of the measured DRS. Beside its general appli-
cability to transparent and opaque substrates, it uses the exact formulas for
the four-phase system "vacuum / thin film / substrate / vacuum" and is hence
independent of the above linear approximation of the DRS.

   The difference between p- and s-polarized light in the above equations due
to the small angle of incidence of $20\,°$ in our experimental setup was estimated
to be smaller than $1.5\,\%$ for the entire absorption range of PTCDA on various
substrates [76]. In principle, two polarizers (polarizer and analyzer) can be
mounted to the DRS setup to check for lateral film anisotropy. Yet, most
of our molecular films being discussed here exhibit uniaxial anisotropy since
there are many differently oriented domains. For this reason, the complex
dielectric function should be treated as a tensor [77]. However, we can only
consider those components that couple with our randomly polarized incident
light (transverse waves). Since we work under near normal incidence, these
are the in-plane components of the dielectric tensor. This does not necessarily
represent an inconvenience, as transition dipole moments are usually in the
plane of the aromatic framework of the molecules used here. The corresponding
DRS (and thus ε_2'') magnitudes should then depend on whether or not the
molecules lie flat on the substrate, thereby offering the opportunity to deduce
structural information from the optical spectra to a certain extent.

2.3.3   Numerical Extraction of the Dielectric Function

As explained above, the simple separation of the DRS into ε_2' and ε_2'' does not
work for the overwhelming part of opaque substrates, and dispersive as well
as dissipative terms affect the measured optical signal. In this case one has to
extract the complex dielectric function of the film from the DR spectra using
a numerical algorithm. The `fit-nk` software (available from sim4tec GmbH,
Dresden, Germany) developed by Robert Nitsche is designed to extract the
two optical functions n and k (or, equivalently, ε' and ε'') of the adsorbate
film from only one spectral measurement, namely the DRS [78, 79]. This
apparent contradiction is resolved by the exploitation of the Kramers-Kronig
transformation which interlinks n and k in such a way that when one quantity
is known for the entire spectral range the other can be obtained via an integral
transformation [68, 80]. The constraints of finite measurement intervals are
coupled to several conditions for the applicability of this procedure, being
discussed in detail in Refs. [78, 79]. Most importantly, the k values must tend
to zero on either end of the spectrum, i.e., one has to experimentally cover
entire molecular absorption bands. The `fit-nk` algorithm now "arbitrarily"
generates a k spectrum and derives the corresponding n spectrum under the
above restrictions. On the basis of this spectral set of n and k, the DRS is

calculated and compared to the measurement according to:

$$[\mathrm{DRS}_{\mathrm{measurement}} - \mathrm{DRS}_{\mathrm{simulation}}\,(n,k)]^2 \to \text{minimum} \quad . \qquad (2.57)$$

Convergence is achieved by means of a Levenberg-Marquardt algorithm [81], and the result is displayed once a satisfying degree of accordance is reached. We would like to direct the reader's attention to Refs. [78, 79] where the authors explain in detail the capabilities and the restrictions of this method, including some demonstrations of convergence as well as thorough trials on numerically generated and experimental examples.

2.3.4   Estimation of Accuracy

For the most part, the above derivation of the DRS and the analysis approaches are similarly discussed in the relevant literature [57, 66, 70, 71, 78, 79]. For the benefit of the reader, we will additionally provide an estimation of the accuracy of the analytical McIntyre approximation and the numerical `fit-nk` algorithm based on exact formulas. By doing so, we will demonstrate that both methods yield comparable results, and, more importantly, artificial peaks are in general *not* generated. This fact will become more important in Chapter 4, where unexpected features in ε'' spectra are observed and discussed.

In Figure 2.10, the measured DRS of $0.93\,\mathrm{ML}$ ($\approx 0.32\,\mathrm{nm}$) of QT on a closed monolayer of HBC on Au(111) (cf. Section 3.4) is shown along with
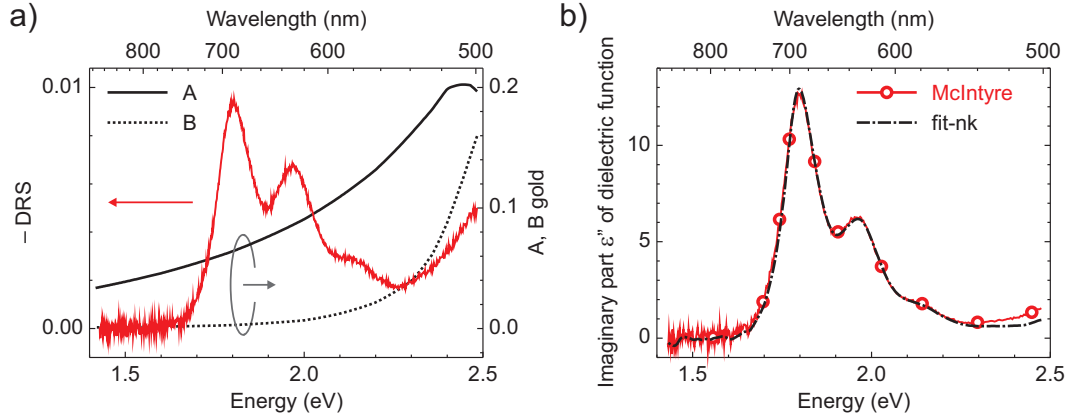
Figure 2.10: Comparison between the analytical McIntyre approximation and the numerical `fit-nk` algorithm based on exact formulas. **a)** Measured differential reflectance spectrum of $0.93\,\mathrm{ML}$ ($\approx 0.32\,\mathrm{nm}$) of QT on a closed monolayer of HBC on Au(111). The vertical scale is inverted (i.e., $-\mathrm{DRS}$) for convenience. For comparison, the A- and B-coefficients of gold (compare Figure 2.9) are plotted on a different scale, demonstrating that $|B| \ll |A|$ for energies below $\approx 2.2\,\mathrm{eV}$. **b)** Imaginary part ε'' of the dielectric function of the QT film derived from the measured DRS shown in (a) by two *independent* methods: *(i)* via the McIntyre approximation (Equation (2.54) $\Rightarrow \varepsilon'' \approx -\mathrm{DRS}/\left[A \cdot 8\pi d/\lambda\right]$), and *(ii)* using the `fit-nk` algorithm.

the spectral A- and B-coefficients of gold (cf. Figure 2.9), demonstrating that $|B| \ll |A|$ for energies below $\approx 2.2\,\mathrm{eV}$. The McIntyre approximation therefore yields $\varepsilon'' \approx -\mathrm{DRS}/[A \cdot 8\pi d/\lambda]$ from Equation (2.54). Alternatively, ε'' can be extracted using the `fit-nk` algorithm. The results of these two *independent* methods are identical within our experimental accuracy. At energies above $2.2\,\mathrm{eV}$ the approximation deviates noticeably from the numerical extraction, as $|B|$ becomes non-negligible compared to $|A|$. Another example of this behavior is given in the Appendix. There, it is demonstrated that a more pronounced deviation of the McIntyre approximation from the `fit-nk` algorithm originates from the neglected term in Equation (2.54) compared to Equation (2.51).

The illustrated correspondence between both methods under certain conditions suggests a straightforward first-order correction of experimental drift in the DRS based on Equation (2.54): Since DRS $\propto \varepsilon''$, the measured DR spectra can be vertically shifted so that the non-absorbing part of each spectrum tends to zero whenever $|B| \ll |A|$ (true for Au and Ag at low energies, and for transparent substrates) .

2.3.5 Realized Experimental Setup

Our apparatus consists of three separately pumped ultrahigh vacuum (UHV) chambers. A fast load-lock and an analysis chamber equipped with a scanning tunneling microscope (STM) are mounted to the deposition chamber, which itself contains all necessary components for film growth and *in situ* optical spectroscopy. The molecular substances are stored in resistively heated Knudsen-type effusion cells at a base pressure of $p \approx 10^{-10}\,\mathrm{mbar}$. A quartz crystal microbalance (QCM) initially monitors the molecular flux. When evaporation parameters for a constant flux are established, the rate can be fine-tuned with the help of STM images of closed monolayers. Almost every type of substrate can be loaded into a five-axial $(x, y, z, \theta, \varphi)$ manipulator where the sample can be heated either by a filament or, additionally, by electron bombardment with a high voltage being applied to the sample. An argon-ion sputter gun enables the preparation of metal surfaces, especially single crystals, done in standard sputtering/annealing cycles. The crystallinity of our substrates and the epitaxial growth of the respective adsorbates can be inspected using an Omicron low energy electron diffraction (LEED) system.

For the reflectance measurements we use a home-built setup (cf. Figure 2.11) that is tightly interconnected to the main deposition chamber yielding maximum mechanical stability. Our ultraviolet-visible (UV-Vis) light sources are either a tungsten halogen lamp or a xenon arc lamp with a stabilized power supply purchased from Müller Elektronik-Optik. An optical multichannel analyzer (OMA) consisting of a back-illuminated single stage Peltier cooled charge-coupled device (CCD) attached to a grating-mirror-spectrograph is used for fast spectra collection (Roper Scientific, SpectruMM 250B with UV-enhance-

ment coating attached to an Acton Research SpectraPro-150, $300\,\mathrm{gr\,mm^{-1}}$ blazed grating). The calibration of the spectral sensitivity was done with a Micropack halogen light source (HL-2000 CAL, color temperature $2960\,\mathrm{K}$). The operating temperature of the CCD of $-35\,°\mathrm{C}$ does not allow the dark noise to be lower than $\approx 0.4\,\%$ per single spectrum. The attached 16 bit A/D converter ($100\,\mathrm{kHz}$ sampling rate) operates at 2^{16} counts per channel at best, which leaves a statistical error of $\Delta N/N = N^{-1/2} \geq 0.4\,\%$ even for large-signal operation. Given that the investigated ultrathin films only generate small changes in reflection, an improvement of the signal-to-noise ratio is indispensable. Statistical noise is reduced by averaging over typically 1800 consecutive spectral measurements which takes approximately $53\,\mathrm{s}$. Such an accumulation is regarded as one spectrum and restarted every $60\,\mathrm{s}$ *during* film growth. The corresponding spectra thus represent a layer thickness range rather than a specific layer thickness. In the following, always the mean value of each range is given. As we desire submonolayer resolution, we work at very low deposition rates of about 1 monolayer in $10\,\mathrm{min}$, varying with the chosen evaporation temperature. Consequently, we have to face drift in the DRS that has to be carefully corrected on the basis of pre- and post-deposition stability tests. Even though minor errors may remain, they have an insignificant impact on our conclusions. Details of the experimental setup, specifically the optical components and the vacuum layout, are given in Refs. [57, 76, 82].

We would like to emphasize that all relevant measurements are carried out *in situ*, i.e., without breaking the UHV. This assures excellent cleanliness and it also prevents ambient condition effects from striking the sample. For example, it has been observed that atmospheric water triggers a rapid recrystallization after a few minutes of exposure to air [76]. When a freshly prepared PTCDA monolayer on a mica sheet (Ted Pella Inc., CAT# 52-6 hi-grade mica sheets)
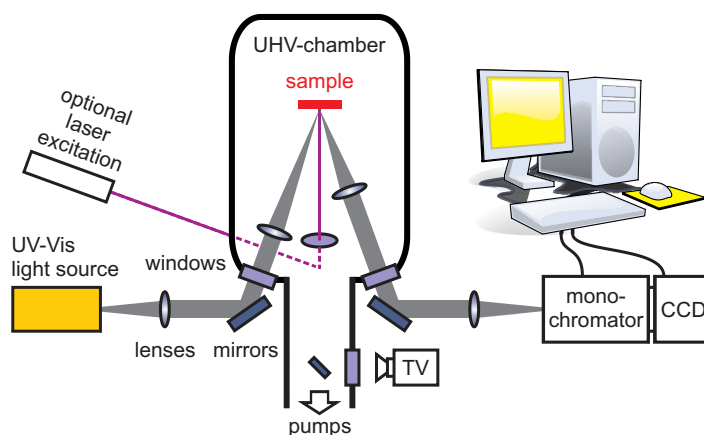

Figure 2.11: Scheme of the experimental setup realized in our laboratory. The home-built DRS device is firmly mounted to the vacuum deposition chamber. Details of the assembled optical components are described in Refs. [57, 76].

was transferred to an *ex situ* spectrophotometer (Shimadzu UV-3101 PC) the absorbance of the adsorbate changed rapidly from a monomer-like to a bulk-like spectrum, clearly indicating the formation of three-dimensional islands. The process could be slowed down, but not stopped, by arranging for dry conditions during sample transfer. It is anticipated that this might also be the case for other molecule–substrate combinations.

For an order of magnitude estimate of our technique's sensitivity, we consider a surface coverage of 0.1 ML for which in many DRS experiments reliable data are routinely obtained. The number of simultaneously detected flat-lying molecules is given by

$$N_{\text{illuminated}} = \text{coverage} \cdot \text{spot size}/\text{area per molecule} \quad . \qquad (2.58)$$

Compared to absorption spectroscopy performed for solutions using standard cuvettes (length $= 10\,\text{mm}$, spot size $\approx 1\,\text{mm}^2$) the same amount of molecules detected in the illuminated cuvette volume $V_{\text{illuminated}}$ would correspond to a concentration of

$$c = \frac{N_{\text{illuminated}}}{V_{\text{illuminated}}} = \frac{\text{coverage} \cdot \text{spot size}/\text{area per molecule}}{\text{spot size} \cdot \text{cuvette length} \cdot N_{\text{A}}} \quad , \qquad (2.59)$$

where N_{A} is the Avogadro constant. Assuming identical spot sizes in DRS and standard absorption spectroscopy, we get:

$$c = \frac{\text{coverage}}{\text{area per molecule} \cdot \text{cuvette length} \cdot N_{\text{A}}} \quad . \qquad (2.60)$$

Inserting typical values for the area per molecule ($\approx 1.2\,\text{nm}^2$ for the (102)-plane of PTCDA, compare Ref. [44]) yields:

$$c \approx \frac{0.1}{1.2 \cdot 10^{-12}\,\text{mm}^2 \cdot 10\,\text{mm} \cdot 6.022 \cdot 10^{23}\,\text{mol}^{-1}} \approx 10^{-8}\,\frac{\text{mol}}{\text{l}} \qquad (2.61)$$

Hence, if identical amounts of molecules are considered, the sensitivity of the DRS would correspond to a concentration of $c \approx 0.01\,\mu\text{mol}\,\text{l}^{-1}$ in standard optical absorption, and even there this is a rather challenging value.

2.3.6 Related Techniques

Similar optical probes of surfaces, such as surface differential reflectance spectroscopy (SDR or SDRS) or reflection anisotropy spectroscopy (RAS, sometimes also called reflectance difference spectroscopy, RDS) are designed to extract the optical signal of the surface from the predominant bulk contribution. In SDRS a change in reflectance induced by purposeful contamination of the surface under investigation, e.g., oxidation, hydrogenation, or chemisorption of foreign atoms, is detected [70, 83–85]. The reflectance difference in RAS

is measured along two perpendicular symmetry axes of the surface [86–89]. The very high number of publications on both techniques only allows for an incomplete list of published work here, but there are several in-depth reviews covering SDRS and RAS and their applications [90–95]. Historically, these spectroscopies are derived from electric field modulation of the reflectivity ("electroreflectance") in semiconductors and metals [96–102]. Optical transitions between filled and empty states of inorganic semiconductor surfaces were detected using differential reflectance with multiple internal reflections [103, 104]. Optical functions of metals have been intensively studied in the light of compositional modulation (i.e., alloys) [105], local field effects [106–108], and at the metal–liquid interface [109].

In the examples given above, the measured signal originates from the substrate surface, or more specifically from its anisotropy (modification) in the case of RAS. Although there are no fundamental restrictions for the choice of the substrate, the applicability of RAS requires a macroscopic lateral anisotropy that is significantly enhanced on certain single crystalline surfaces [94]. However, making use of the anisotropy of the sample may also constitute an inconvenience because structural order at the surface is indispensable in the (macroscopic) area of detection – a requirement typically not being fulfilled even in epitaxial organic thin films, due to the presence of many symmetrically equivalent rotational domains. In SDRS, the change in reflectance is related to the intrinsic optical response of the substrate surface, provided that the purposeful contamination hardly contributes to the spectra in the wavelength range considered.

Only recently, the application of these or similar techniques to organic thin films moved into focus, since the availability of thin film optical data became more and more crucial for various applications. The most important contributions in this field are assessed by a recent review [110], which is why we will not extend the above remarks here.

2.4 Structural and Electronic Characterization

It is one key objective of this work to demonstrate that optical differential reflectance spectroscopy is especially powerful in combination with a structural and/or electronic characterization of the systems under investigation. For this reason, we will succinctly and non-exhaustively present the employed techniques in this section.

2.4.1 Low Energy Electron Diffraction (LEED)

Low energy electron diffraction (LEED) makes use of the wave-like properties of electrons being expressed by the de Broglie-wavelength $\lambda = h/\sqrt{2mE}$, where

h is Planck's constant and E the particle energy. A monochromatic beam of electrons is focused onto a crystalline target whose atoms / ions / molecules serve as centers of diffraction. The crystallinity of the sample then represents a diffraction grating with lattice constants of typically a few Ångströms (Å). This requires primary electron energies E_{primary} of a few electron volts (eV) up to a few hundred eV. Since such an electron beam has in most materials a mean free path of only $\approx 1\,\text{nm}$, LEED is in fact strongly surface-sensitive and is used to elaborate the two-dimensional lateral lattice constants of the topmost layer(s) of the target. In "display-type" LEED setups the electron gun with a heatable filament is placed in front of the sample with the electron beam striking the surface at perpendicular incidence. The back-scattered electrons are usually recorded with a hemispherical fluorescent screen making post acceleration of the electrons via a high voltage necessary. In contrast, the diffraction pattern of spot profile analysis LEED (SPA-LEED) is recorded with a channeltron [111]. Since not all scattering processes are elastic, the inelastically scattered and the secondary electrons with energies smaller than E_{primary} can be suppressed to a certain extent, but will generally contribute to a diffuse background. The LEED setup used in this work is sketched in Figure 2.12.
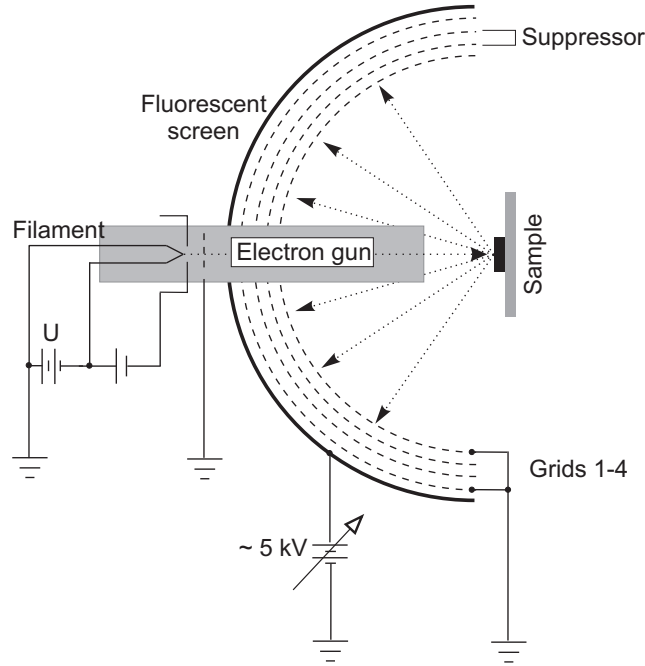
Figure 2.12: Scheme of a "display-type" four-grid LEED setup. The diffraction patterns are captured with a CCD camera located to the left. Reproduced from Ref. [112].

The discussion of the electron diffraction patterns is normally done in reciprocal space. The primitive reciprocal lattice vectors $(\mathbf{a}_1^\star, \mathbf{a}_2^\star, \mathbf{a}_3^\star)$ are related to those of the real space lattice $(\mathbf{a}_1, \mathbf{a}_2, \mathbf{a}_3)$ in the following way:

$$\mathbf{a}_i^\star = 2\pi \cdot \frac{\mathbf{a}_j \times \mathbf{a}_k}{\mathbf{a}_i \cdot (\mathbf{a}_j \times \mathbf{a}_k)} \quad . \tag{2.62}$$

When incident electrons with wave vector $|\mathbf{k}_{\mathrm{primary}}| = 2\pi/\lambda_{\mathrm{primary}}$ and back-scattered electrons with $|\mathbf{k}| = 2\pi/\lambda$ fulfill the Laue condition

$$\mathbf{k} - \mathbf{k}_{\mathrm{primary}} = \mathbf{G}_{hkl} \quad , \tag{2.63}$$

constructive interference and hence diffraction of scattered electron waves occur. Here, (h, k, l) is a set of integer numbers and

$$\mathbf{G}_{hkl} = h\mathbf{a}_1^\star + k\mathbf{a}_2^\star + l\mathbf{a}_3^\star \tag{2.64}$$

is a vector in the reciprocal space. As only elastic scattering is considered, the magnitudes of the electron wave vectors remain unchanged, i.e. $|\mathbf{k}_{\mathrm{primary}}| = |\mathbf{k}|$. The Laue condition (Equation (2.63)) can readily be visualized by the Ewald sphere construction with a sphere radius of $|\mathbf{k}_{\mathrm{primary}}|$. Because of the rather short electron mean free path, only the first few atomic layers contribute to the back-scattered signal. Consequently, the diffraction conditions perpendicular to the surface are absent and the reciprocal space is just a two-dimensional lattice with rods sticking out of each lattice point. The above relations can hence be reduced to a two-dimensional form.

A constant error in the displayed primary energy of $\Delta E_{\mathrm{primary}} = +1.1 \pm 0.2\,\mathrm{eV}$ was determined according to a method proposed in Ref. [113], which had to be subtracted for an exact analysis. Unless otherwise noted, the uncorrected value of the displayed primary energy will be given. Lateral lattice parameters were derived from distortion-corrected LEED images making use of the commercially available simulation software `LEEDSim` (available from sim4tec GmbH, Dresden, Germany).

Further details about the interpretation of LEED measurements and the analysis in the framework of the kinematic approximation as an attempt to model the distribution of spot intensities can be found in Refs. [112–115].

2.4.2 Scanning Tunneling Microscopy (STM)

The scanning tunneling microscope (STM) is certainly among the most valuable tools available for real space imaging in the field of nanotechnology and surface science. Since its invention in the early 1980s by Binnig and Rohrer [116, 117] it has continuously established new records for lateral resolutions on the molecular and atomic scales.

A schematic illustration of the basic STM operating modes is shown in Figure 2.13. In general, a bias is applied between a non-insulating sample and a sharp conductive tip, usually electrochemically etched platinum-iridium or tungsten wires. Since the tip is not in direct contact with the surface, current can only flow via tunneling. The tunneling current I is exponentially dependent on the tip–sample distance z. For this reason, the tip atoms in closest proximity to the sample yield the overwhelming part of the measured

signal, and even subtle surface morphologies can be mapped. Therefore, the lateral resolution depends very much on the quality of the tip and of the sample surface, as well. Imaging is achieved by scanning the tip over the surface in one of two basic modes. In the *constant current mode* the tunneling current is fixed by means of a feedback loop while scanning the surface - the monitored quantity is the relative displacement of the tip (z direction, cf. Fig. 2.13a). In the *constant height mode* the average tip–sample distance is fixed by switching off the feedback loop while scanning the surface - the monitored quantity is the tunneling current I (cf. Fig. 2.13b).

Of course, in reality the operating mode of a STM is in between these two extremes, since the tunneling parameters, such as the feedback gain, can be adjusted rather freely. The interpretation of STM images may become difficult because the tunneling current is also sensitive to locally (or temporally) varying substrate workfunctions. Likewise, organic adsorbates contribute to the tunneling current via their molecular orbitals (MOs) responding differently to varying applied bias. Sometimes, the MOs can even delocalize over entire molecular islands into two-dimensional band states [34]. We will not extend this discussion here, but rather refer the reader to the relevant literature. From the vast number of published work in this field, we have chosen a few reviews [118–120] which extensively cover the STM instrumentation, theoretical background, and possible applications. STM images presented here were evaluated using the software `WSxM` (Nanotec Electrónica S.L.) [121].
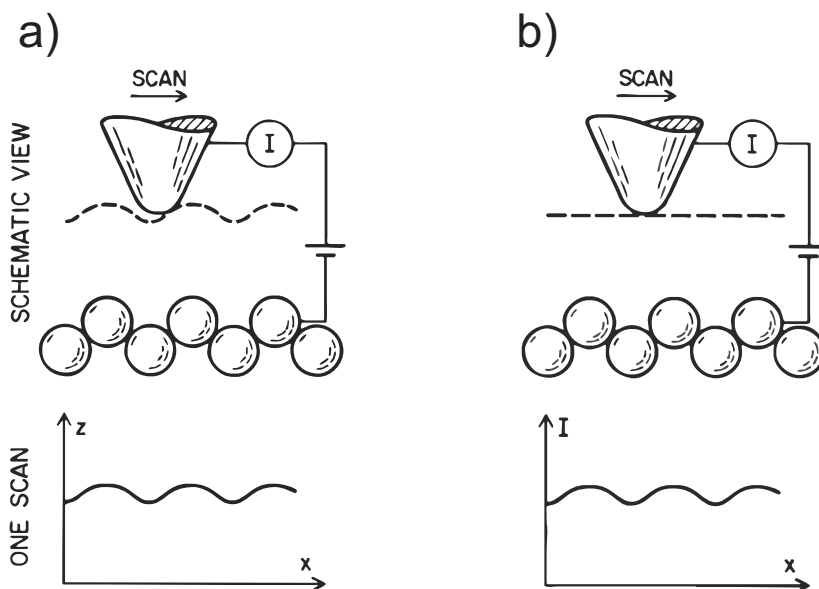
Figure 2.13: Sketch of the STM working principle for either **a)** *constant current mode*, or **b)** *constant height mode*. The upper panels schematically visualize the movement of the conductive tip at a small distance d above the substrate atoms, represented by spheres. The lower panels depict the recorded signals as single line scans, namely the topography in (a), and the current in (b), respectively. Reproduced from Ref. [118].

2.4.3   Ultraviolet Photoelectron Spectroscopy (UPS)

For the characterization of the electronic properties of interfaces, photoemission spectroscopy (PES) is the method of choice. It relies on the photoelectric effect, i.e., electrons are emitted from matter after the absorption of a photon of a given energy $E_{\mathrm{photon}} = h\nu$. For this reason, it yields the occupied electronic structure, also called valance levels/bands. The kinetic energy E_{k} of the ejected electron is given after Einstein by:

$$E_{\mathrm{k}} = h\nu - E_{\mathrm{B}} - \Phi \quad , \tag{2.65}$$

where E_{B} is the binding energy of the electron, and Φ is the workfunction of the material. Koopmans' theorem makes use of the assumption that all the energy levels (or, more rigorously, the associated Fock operators in Hartree-Fock theory) of a molecule remain practically unchanged during the ejection of an electron. Consequently, the first ionization potential I of a closed-shell system is equal to the negative orbital energy of the HOMO, i.e., the binding energy. Hence, PES maps directly the occupied density of states (DOS) in good approximation. Particularly, in ultraviolet photoelectron spectroscopy (UPS), light emitted by a helium discharge lamp at $h\nu = 21.22\,\mathrm{eV}$ (He-I) is usually used to eject valence electrons in the proximity of the Fermi level E_{F}, and their kinetic energy E_{k} is analyzed (Figure 2.14) [22, 23, 25, 26]. Additionally, in X-ray photoelectron spectroscopy (XPS) photons are often
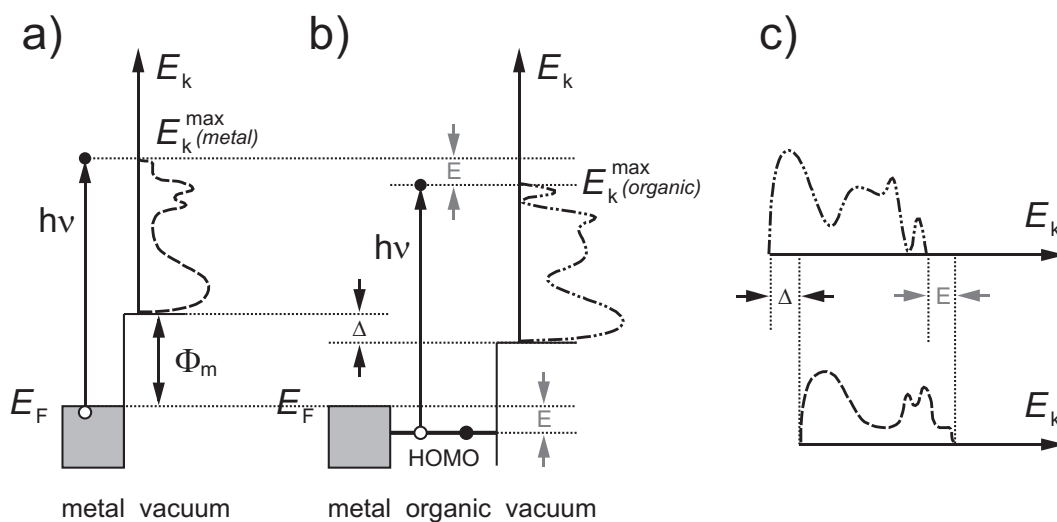
Figure 2.14: Principles of UPS and schematic depiction of photoemission processes. **a)** Energy level diagram of the metal/vacuum interface. The metal workfunction is labelled Φ_{m}. **b)** Energy level diagram of the metal/organic/vacuum interface. **c)** Corresponding photoemission spectra for a given photon energy $h\nu$ in standard orientation versus kinetic energy E_{k} as recorded in (a) and (b), respectively. The difference between the high binding energy cutoffs with and without organic adsorbate represents the interface dipole Δ. Adapted from Ref. [22].

provided by a monochromatic Al-Kα source at $h\nu = 1486.6\,\text{eV}$, being able to excite core level electrons.

Electronic spectra of some of the metal–organic systems presented in this work were acquired in collaboration with the group of Prof. Neal R. Armstrong at the University of Arizona, Tucson, USA. UPS and XPS measurements were carried out in a Kratos Axis-Ultra photoelectron spectrometer in the LESSA laboratory [122]. There, all relevant experiments were also carried out *in vacuo*, at base pressures of typically $p \approx 5 \times 10^{-9}\,\text{mbar}$. A negative bias of $-5.00\,\text{V}$ was applied to the sample to clear off the detector workfunction and to further enhance the collection of lowest kinetic energy electrons.

2.5   Thin Film Growth and Epitaxy

2.5.1   Thin Film Growth

Commonly, thin film growth is sorted into three categories, two of which are actually just boundary cases of the third [123]:

- *Layer-by-layer (Frank-van der Merwe) growth* – Two-dimensional flat islands spread laterally until a layer is completely filled, then the subsequent layer grows on top, and so on [124].

- *Island (Volmer-Weber) growth* – Islands or clusters are formed on the substrate from the very beginning of the deposition, exhibiting three-dimensional character and being spatially separated from each other [125].

- *Stranski-Krastanov growth* – In this intermediate case, the growth of usually one or two closed monolayers (also called 'wetting layers') is followed by a formation of islands on top [126].

None of these growth modes is particularly affiliated with any of the types of epitaxy or vice versa. However, they will play a crucial role for the observability of aggregation effects, such as physical dimerization or oligomerization in stacked molecular arrangements (cf. Section 2.2.3). The occurrence of one of these growth modes depends sensitively on the chosen deposition parameters, but also on the specific molecule–substrate combination in the first place.

The application of low energy electron microscopy (LEEM) operated in the photoelectron emission microscopy (PEEM) mode enables real-time monitoring of the thin film growth [127]. In such experiments, the relative layer coverage is determined from the distribution of specific contrasts between adjacent adsorbate layers in real space images. For pentacene on clean Si(100) it was shown that the coverage of the first layer increases linearly with deposition time after nucleation, as depicted in Figure 2.15. When a coverage of 60 % was
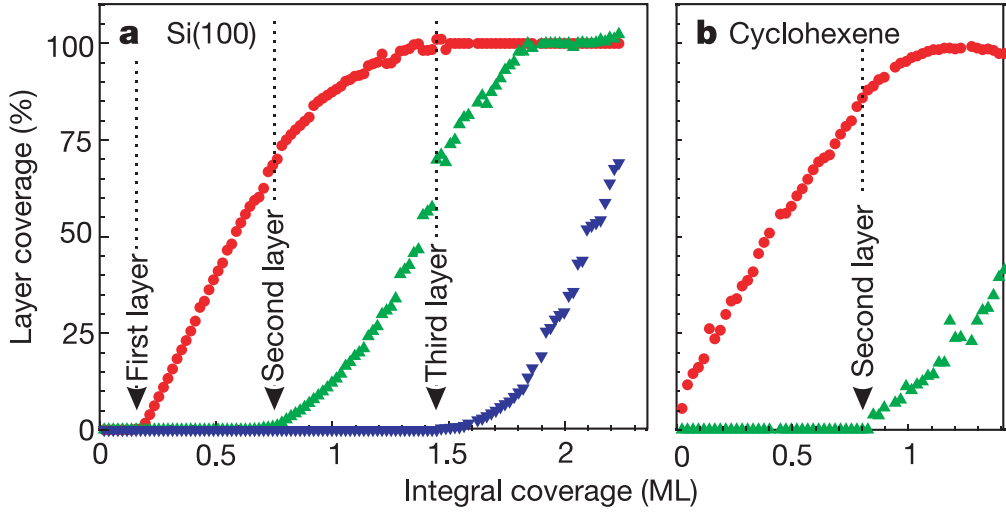
Figure 2.15: Growth dynamics of pentacene thin films, **a)** deposited on Si(100), and **b)** deposited on cyclohexene-saturated Si(100). The plot shows the relative coverage (in %) for the first (●), second (▲), and third (▼) layers separately versus the integral substrate coverage (in ML). Reproduced from [127].

reached, islands started to nucleate in the second layer. Further, at a coverage of 60 % of the second layer – the first having already reached completeness – the nucleation of the third layer began, showing "steady-state layer-by-layer growth". It was also demonstrated by passivating the Si(100) dangling bonds with cyclohexene that the initial dead-time until the beginning nucleation of the first layer could be suppressed and that a higher fractional coverage of the first layer could be achieved before the growth of the second layer actually began.

2.5.2   Epitaxy

The term *epitaxy* has the Greek origins *epi*, meaning 'on top' or 'above', and *taxis*, meaning 'in arranged/ordered manner'. A possible translation would thus be '(ordered) arrangement upon'. Epitaxial growth is established if one specific geometrical relation between an overlayer lattice $\{\mathbf{b}_1; \mathbf{b}_2\}$ and a substrate lattice $\{\mathbf{a}_1; \mathbf{a}_2\}$ can be found:

$$\begin{bmatrix} \mathbf{b}_1 \\ \mathbf{b}_2 \end{bmatrix} = \underline{C} \cdot \begin{bmatrix} \mathbf{a}_1 \\ \mathbf{a}_2 \end{bmatrix} = \begin{pmatrix} C_{11} & C_{12} \\ C_{21} & C_{22} \end{pmatrix} \cdot \begin{bmatrix} \mathbf{a}_1 \\ \mathbf{a}_2 \end{bmatrix} \quad . \tag{2.66}$$

Sometimes, a few geometrical relations are simultaneously observed, each independently denoting an epitaxial coincidence characterized by dissimilar epitaxy matrices $\underline{C}$. In fact, different types of epitaxy can occur, which may be categorized on the basis of the elements $C_{11} \ldots C_{22}$ of the epitaxy matrix $\underline{C}$. If one considers primitive adsorbate (and substrate) unit cells, all epitaxy modes can be directly deduced from the existence of integer elements in $\underline{C}$ [18, 128]

with the exception of the so-called line-on-line coincidence [43, 112] as listed below:

- *Commensurism* – All adsorbate lattice points are located on substrate lattice points. The epitaxy matrix consists of integers only (Fig. 2.16a).

- *Coincidence I or point-on-line coincidence* – All adsorbate lattice points are located on primitive substrate lattice lines, but not necessarily on substrate lattice points. The epitaxy matrix contains one column of integers and the other column may be irrational. Sometimes, an additional distinction is made for this case based on the occurrence of a small overlayer supercell (whose corner lattice points are located on substrate lattice points) if the non-integer column consists of rational elements (Fig. 2.16b vs. c).

- *Coincidence II or geometrical solution* – All adsorbate lattice points are located on substrate lattice lines that are not all primitive. An overlayer supercell is formed whose corner lattice points are located on substrate lattice points. No integer columns are contained in the epitaxy matrix, but all elements are rational (Fig. 2.16d).

- *Coincidence III or line-on-line coincidence* – All adsorbate lattice points are located on substrate lattice lines that are not required to be primitive. No overlayer supercell is formed. The epitaxy matrix consists of non-integer columns which can even contain irrational elements (not depicted in Fig. 2.16).

- *Incommensurism* – None of the above cases applies. No integer columns are contained in the epitaxy matrix, and at least one matrix element is irrational (not depicted in Fig. 2.16).

Note that there is no specific registry between substrate and adsorbate real space lattices in the case of line-on-line coincidence. This fact renders an illustration of line-on-line epitaxy rather unfavorable, which is why it is avoided in Figure 2.16. Moreover, it is difficult if not impossible to recognize this type of epitaxy from looking at the matrix elements. Instead, it can be readily identified by the coincidence between non-primitive substrate and adsorbate reciprocal lattice vectors [43, 112].

It is hence evident that epitaxy and different growth modes offer a variety of combinations. Both can readily be influenced by a number of different parameters, such as molecular deposition rate, substrate temperature, substrate morphology, surface orientation, cleanliness, and so forth. Likewise, a specific substrate modification or passivation can be of particular importance, as demonstrated in Figure 2.15. We are, however, not solely devoted to the examination of growth behavior. In fact, the relations between the physical structure
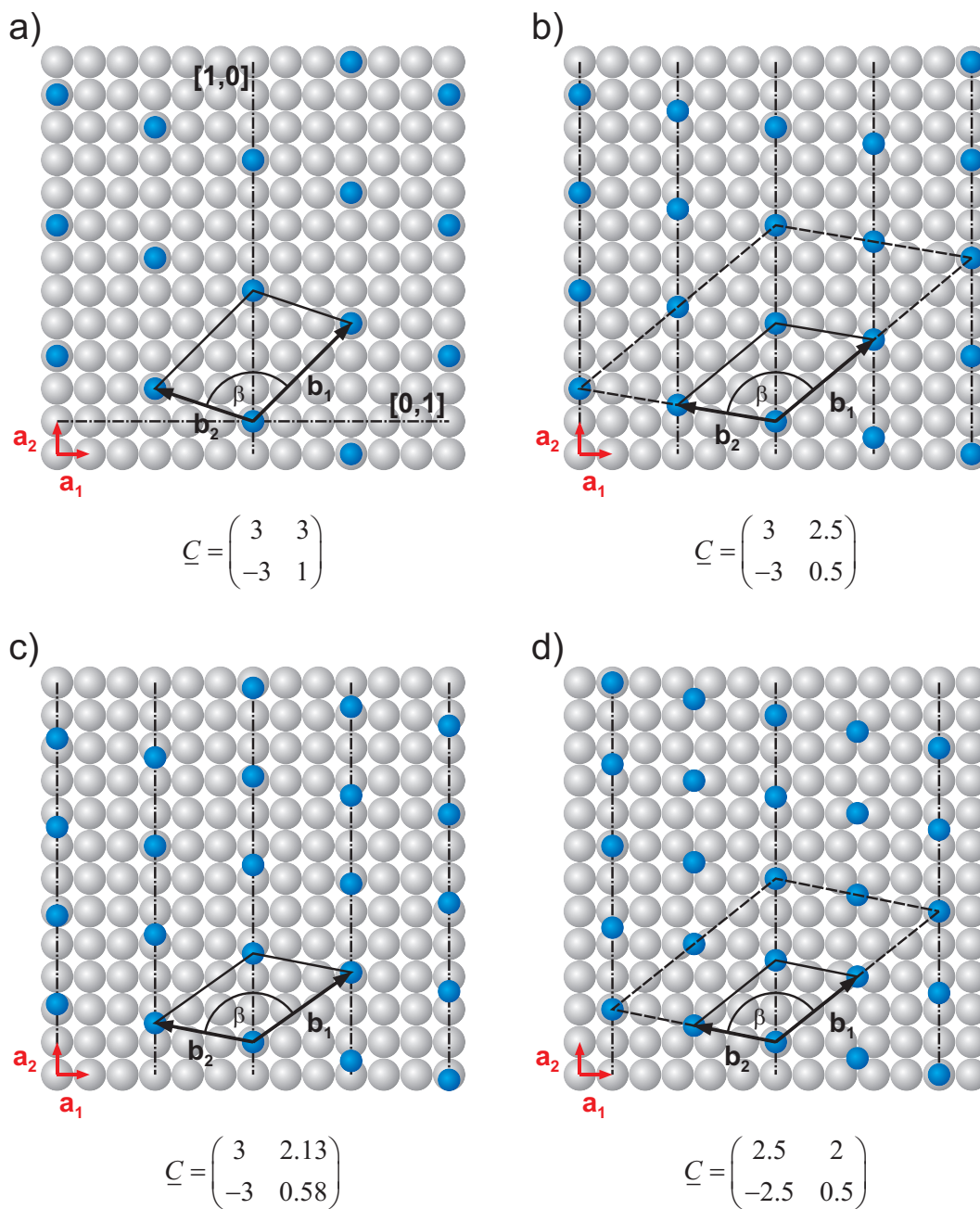
a)

$$C = \begin{pmatrix} 3 & 3 \\ -3 & 1 \end{pmatrix}$$

b)

$$C = \begin{pmatrix} 3 & 2.5 \\ -3 & 0.5 \end{pmatrix}$$

c)

$$C = \begin{pmatrix} 3 & 2.13 \\ -3 & 0.58 \end{pmatrix}$$

d)

$$C = \begin{pmatrix} 2.5 & 2 \\ -2.5 & 0.5 \end{pmatrix}$$

Figure 2.16: Hierarchical classification of the different types of epitaxy. Unit cells are marked with solid parallelograms. Primitive substrate lattice lines are drawn as dash-dotted lines. **a)** *Commensurism.* **b)** and **c)** *Coincidence I or point-on-line coincidence.* A small supercell (here (2×2), indicated by dashed lines) emerges if the non-integer column consists of rational elements, as shown in (b). **d)** *Coincidence II or geometrical solution.* A small supercell is also formed here. After [18, 112, 128].

and the physicochemical properties of organic–inorganic and organic–organic interfaces are in the foreground of this work and will move into focus in the following.

3   Electronic Coupling of Organic Adsorbates to Substrates

The essential experimental results of this thesis will be presented and discussed in the following two major parts. In this chapter, we will elaborate to what extent electronic coupling effects of organic adsorbates to different substrates are manifested in optical spectra. After a short introduction of quaterrylene (QT) and its optical and physical properties known from the literature, we discuss its thin film optical behavior measured with differential reflectance spectroscopy (DRS). Au(111), graphite, mica, and quartz glass were used as substrates with the objective to establish a hierarchical order. We will begin with the strongest observed coupling on the metal surface and will provide evidence that this coupling can be efficiently suppressed by an atomically thin spacer layer comprising exclusively organic molecules, namely hexa-peri-hexabenzo-coronene (HBC). Further, we will demonstrate that different growth modes of the organic film ("face-on" versus "edge-on") result in a markedly different optical response. The key findings will be summarized at the end.

3.1   Introduction

Unsubstituted quaterrylene (QT) and hexa-*peri*-hexabenzocoronene (HBC), see Table 2.1, are planar polycyclic aromatic hydrocarbons (PAHs). They both exhibit a rather poor solubility in standard solvents, but can be dissolved in 1,2,4-trichlorobenzene enabling the measurement of monomer absorption spectra in solution [129, 130]. As depicted in Figure 3.1a, there is effectively no overlap between both spectra, which is due to the dissimilar electronic structures of QT and HBC as also deduced from gas phase photoelectron spectroscopy [130–132]. Optical absorption spectra of evaporated QT and HBC thin films are available from the literature [133–135], clearly indicating spectral broadening of the molecular aggregates and distinct shifts with respect to the monomer absorption, cf. Figure 3.1b. In the following, we will concentrate on QT. There are indications that different QT crystal polymorphs (thin films
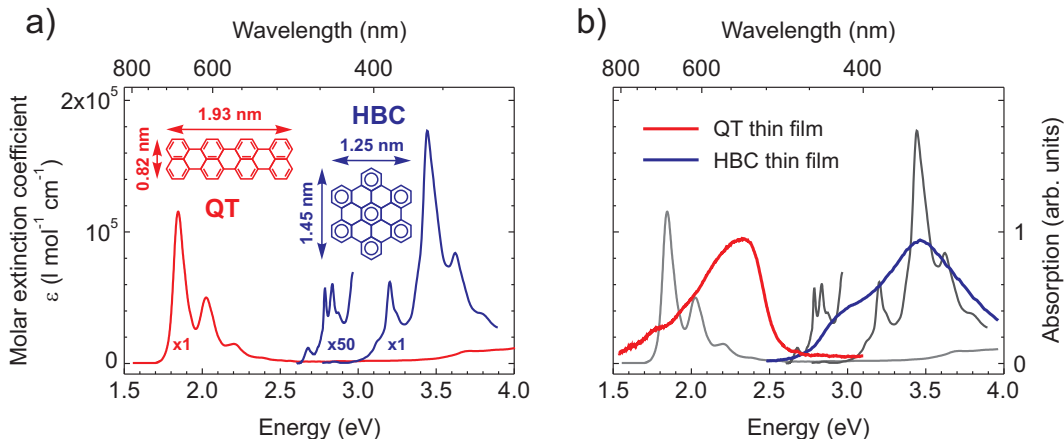
Figure 3.1: Optical absorption data of QT and HBC and respective molecular dimensions. **a)** Dissolved in 1,2,4-trichlorobenzene at room temperature, adapted from [129, 130]. Both contributions did not specify whether natural or decadic molar extinction coefficients (which differ by a factor of $\ln 10 \approx 2.3$) were employed. We therefore assume the decadic quantity, as this is the common case for liquids. It is, however, stated in Ref. [130] that the ε values were determined in the same way as in Ref. [129], ensuring direct comparability. Due to the D_{6h} symmetry of HBC, the energetically lowest transition at $2.68\,\text{eV}$ is forbidden and becomes visible when magnified by a factor of 50. **b)** Respective thin film spectra for HBC ($5\,\text{nm}$ on SiO_2, presumably in the bulk crystal phase) and QT (a few nm thick on mica), adapted from [133, 134].

versus single crystals) show different optical absorption behavior [136]. The reasons for these dissimilarities have not yet been fully understood.

The bulk crystal structure of QT is known from three-dimensional X-ray data [46], as summarized in Table 3.1. It is made up of dimers comprising two centro-symmetrically related molecules exhibiting a mean perpendicular distance of $3.41\,\text{Å}$ (cf. Figure 3.2). The pronounced three-dimensional character of the bulk crystal prohibits the application of the exciton model developed for quasi-one-dimensional molecular crystals (cf. Section 2.2.3). Therefore, the understanding of the optical behavior of QT is not necessarily as straightforward as that of PTCDA.

Table 3.1: Bulk crystal structure of QT: monoclinic, space group $P2_1/a$ with equivalent positions $\pm(x, y, z; \frac{1}{2}+x, \frac{1}{2}-y, z)$. Adapted from [46]. Standard deviations (given in parentheses) were derived from least-squares treatment, while the true accuracy is less good according to Ref. [46].

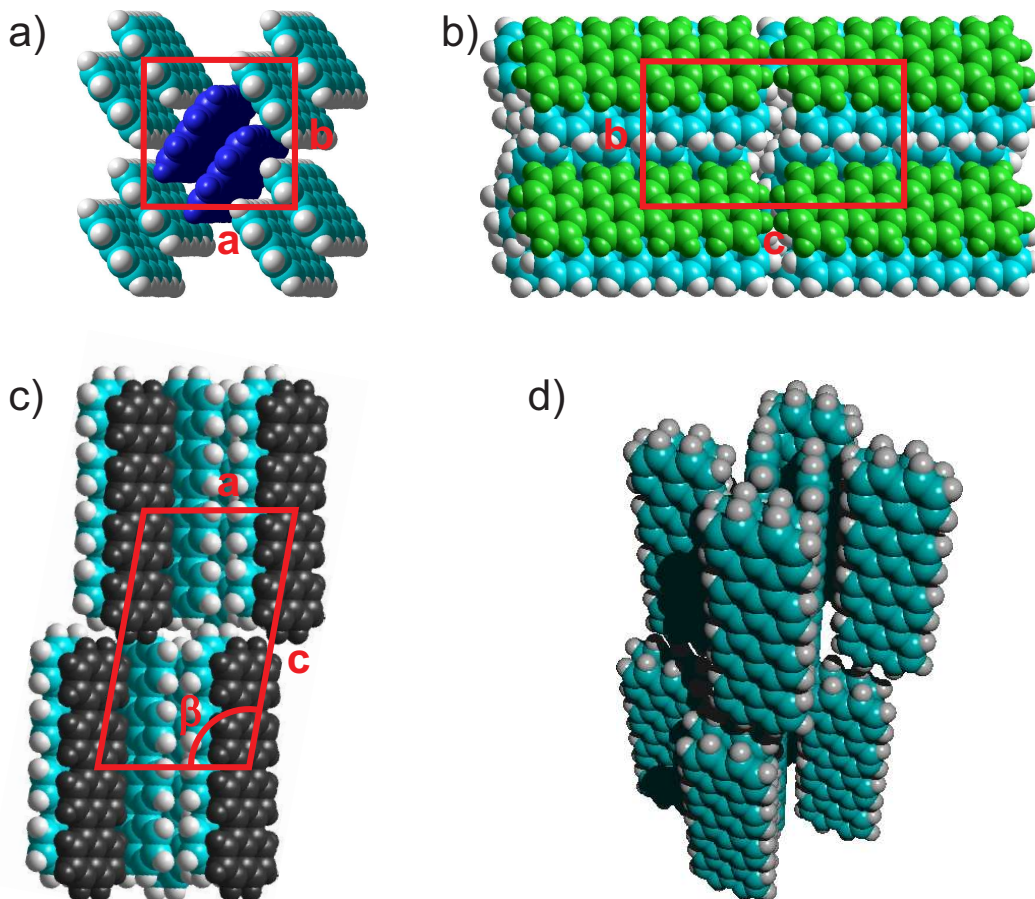| $a(\text{Å})$	$b(\text{Å})$	$c(\text{Å})$	$\beta(°)$	$V(\text{Å}^3)$	Z	$\rho(\text{g cm}^{-3})$
11.145(1)	10.630(3)	19.235(4)	100.46(4)	2240.5	4	1.485

Figure 3.2: Illustration of the QT bulk crystal structure: **a)** a–b-plane, **b)** b–c-plane, **c)** a–c-plane, **d)** three-dimensional rendering. The corresponding parameters can be found in Table 3.1. As apparent in these figures, the QT bulk crystal does not exhibit a plane in which all the molecules lie flat, as opposed to PTCDA.

Profound knowledge of the growth behavior of planar aromatic molecules on insulating and conductive substrates is highly desired since an alignment of the aromatic cores in face-on or edge-on geometry, respectively, will have a direct impact on the charge carrier mobility and hence on the performance of electronic devices, such as OPVDs or OFETs. Previous atomic force microscopy (AFM) and X-ray diffractometry (XRD) studies revealed that QT thin films grow in upright orientation on SiO_2 surfaces with grain sizes depending on the substrate temperature [137, 138]. Layered structures were formed, as evidenced by the $(0\,0\,l)$ Bragg reflections and the apparent terraces with an average height of $\approx 2\,\mathrm{nm}$. The slightly compressed QT lattice relaxes as the film thickness increases up to $4\,\mathrm{ML}$ of upstanding molecules, eventually coinciding with the three-dimensional bulk phase. It has been demonstrated that the charge carrier mobility saturates approximately at this critical thickness when QT films exhibiting a pronounced Stranski-Krastanov growth were used in an OFET architecture on SiO_2/p-Si(001) [139]. It was concluded that

the first few layers serve as a transistor channel with an efficient conductivity due to the overlap of π-orbitals perpendicular to the molecular planes. The growth was shown to have a stronger layer-by-layer character when QT was deposited on an octadecyltrichlorosilane (OTS) intermediate layer, thereby enhancing the charge carrier mobility by almost an order of magnitude [140]. Hence, it becomes evident that the performance of such devices is decisively influenced by ordering effects as well as grain sizes and that improvement can be achieved in an organic–organic stacked arrangement. Thus, we will emphasize the structure–properties-relations of QT films on different substrates in the following.

3.2   QT on Au(111): Strong Coupling

Differential Reflectance Spectra.   In a first experiment, we deposited QT on single crystalline Au(111). The *in situ* recorded differential reflectance spectra (DRS) are plotted in Figure 3.3 for various film thicknesses. In first approximation, the DRS is proportional to the adsorbate thickness d, as expected from Equation (2.51). However, the more or less subtle spectral developments, especially when passing from the (sub-) monolayer regime to two or more layers, are in part concealed by the fact that the DRS on such an opaque substrate is actually a convolution of the adsorbate *and* substrate optical response, com-
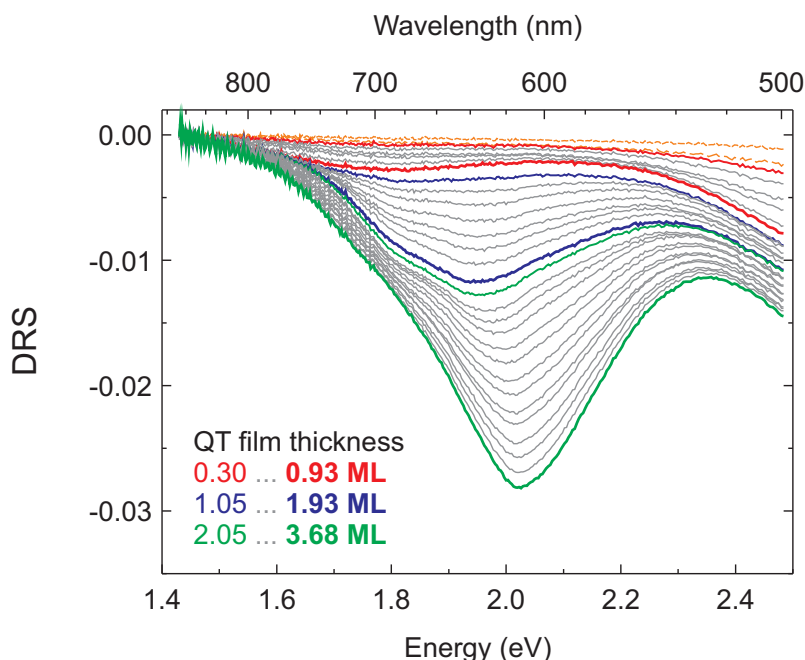

Figure 3.3:   Drift-corrected differential reflectance spectra of QT deposited on Au(111). The dashed orange curves represent QT film thicknesses of $0.05\,\text{ML}$ and $0.18\,\text{ML}$, respectively, and turned out to yield unreliable dielectric functions via `fit-nk` due to the rather low signal-to-noise ratio.

pare Section 2.3.2. Thus, we need to extract the complex dielectric function of these DR spectra using the `fit-nk` algorithm for an analysis of the absorbance behavior. These data have also been discussed in Ref. [133].
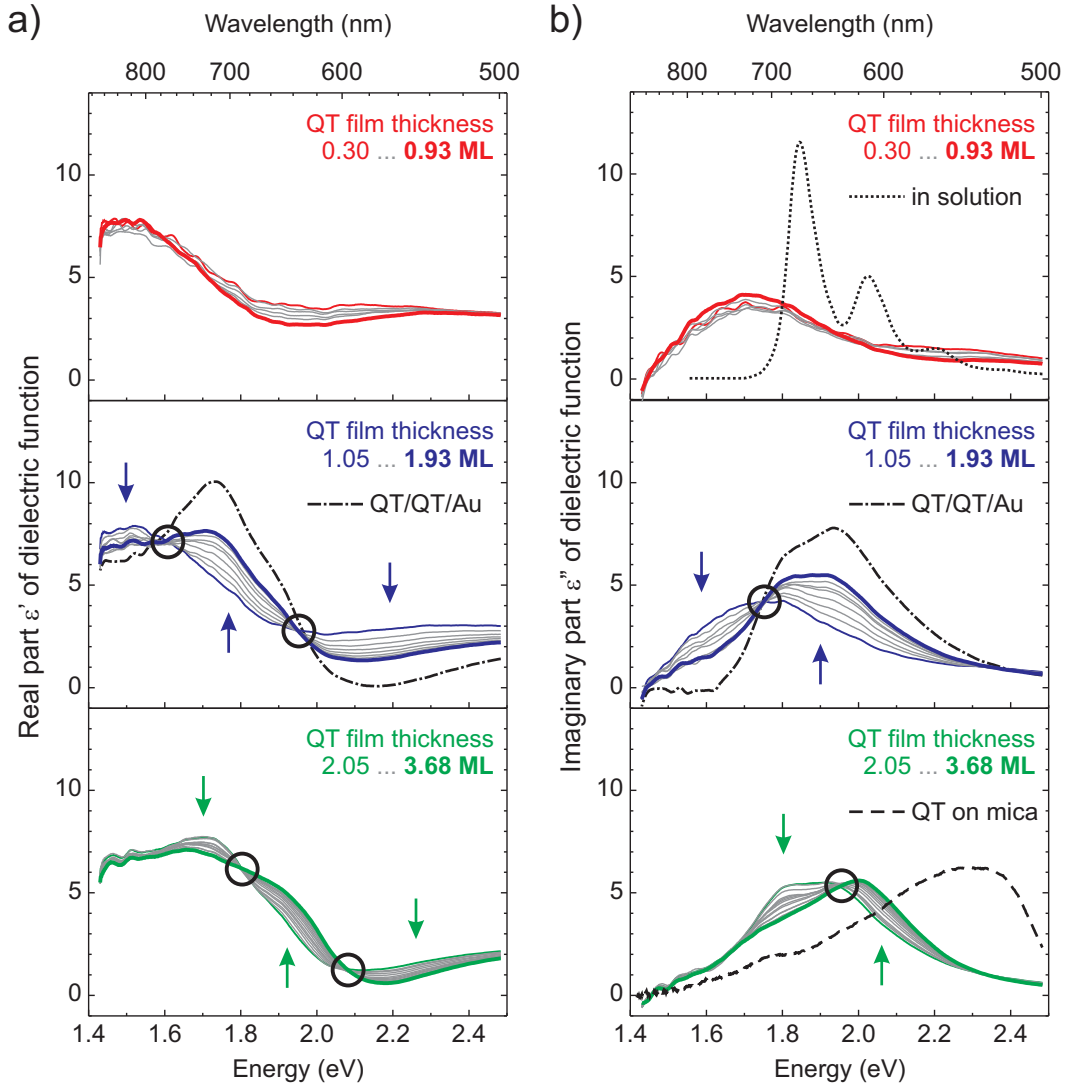

Figure 3.4: **a)** Real part ε', and **b)** imaginary part ε'' of the dielectric function $\hat{\varepsilon} = \varepsilon' - i\varepsilon''$ of QT deposited on Au(111) extracted from the DRS shown in Figure 3.3. Both spectral series are divided into three subsequent growth stages for clarity: *upper panels* $0\,\mathrm{ML} < d < 1\,\mathrm{ML}$, *center panels* $1\,\mathrm{ML} < d < 2\,\mathrm{ML}$, *bottom panels* $d > 2\,\mathrm{ML}$. For comparison, the absorbance spectrum of QT dissolved in 1,2,4-trichlorobenzene is shown (dotted curve, not to scale) [129]. The final ε'' spectra of this series are compared to an *ex situ* recorded absorbance spectrum of QT on mica (dashed curve, not to scale), presumably in the polycrystalline bulk phase. The spectral development with increasing film thickness is indicated by arrows, the resulting isosbestic points are marked with circles. The dash-dotted curves in the center panels represent the hypothetical dielectric function if one takes the first ML of QT to be part of the substrate, i.e., considering the system $0.93\,\mathrm{ML}$ of QT on $1\,\mathrm{ML}$ of QT on Au(111) (see Section 3.4 for explanations).

Dielectric Function Extracted from DRS.   The complex dielectric function $\hat{\varepsilon} = \varepsilon' - i\varepsilon''$ of QT films on Au(111) was extracted from the corresponding DRS series depicted in Figure 3.3 using the `fit-nk` algorithm. Both, the real part ε' and the imaginary part ε'' are plotted in Figure 3.4 for the sake of completeness. However, we will focus the discussion on ε'', since this quantity describes the absorbance behavior of the adsorbate film, as opposed to ε'.

Up to a surface coverage of $\approx 1\,\text{ML}$, the ε'' spectra are nearly identical within experimental accuracy, exhibiting an almost structureless appearance with only one very broad peak centered at around $1.7\,\text{eV}$ (Figure 3.4b). These spectra bear no resemblance to monomeric spectra as in solution (Figure 3.1), and as one would also expect on inert (i.e., non-metallic) surfaces [32]. In contrast, metal surfaces tend to strongly interact electronically with an adsorbate. Coupling of molecular orbitals to electronic states [141, 142] extending perpendicularly from the metal surface will lead to a significant broadening of the adsorbate levels, as described, e.g., by the Anderson–Newns model [143, 144], and can be further accompanied by charge transfer. In principle, this effect has been known for the molecular energy levels from photoelectron spectroscopy measurements, and it is sometimes called metal–organic "hybridization" in the literature [145]. However, here we are able to provide evidence for the impact of this phenomenon on the optical transitions. The strong electronic coupling between the adsorbate and the substrate already indicates the occurrence of flat-lying QT, as it may be expected that in this case the metal surface would interact rather efficiently with the molecules.

There is a significant development in the ε'' spectra for increasing film thickness above $1\,\text{ML}$ (Figure 3.4b). The most severe spectral changes of QT on Au(111) occur between $1\,\text{ML}$ and $2\,\text{ML}$, where the intensity below $1.75\,\text{eV}$ diminishes, while it rises above this energy. With the growth of the second ML, the π–π-interaction between adjacent molecules in a stacked arrangement sets in, which is appreciably stronger than the molecules' in-plane interaction. The occurrence of a spectral substructure is also apparent. Further development of the spectral shape occurs after a nominal thickness of $2\,\text{ML}$, where the spectra are characterized by a peak at $2.00\,\text{eV}$ and a shoulder at $1.75\,\text{eV}$. The ε'' spectra saturate at around $4\,\text{ML}$.

There are very characteristic turning points at $1\,\text{ML}$ and $2\,\text{ML}$ in Figure 3.4, at which the spectral development indicated by arrows abruptly changes direction. This fact already suggests a layered growth mode, as otherwise the spectral changes would tend to be rather blurred, if present at all. Between $1\,\text{ML}$ and $2\,\text{ML}$ of QT the spectra $\mathcal{S}\left(f_{\mathcal{D}}, E\right)$ can be expressed to a good approximation as a mixture of monolayer spectrum $\mathcal{M}(E)$ and double layer spectrum $\mathcal{D}(E)$ with a fraction $f_{\mathcal{D}}$ increasing at the same rate as the fraction $f_{\mathcal{M}} = 1 - f_{\mathcal{D}}$ decreases:

$$\mathcal{S}\left(f_{\mathcal{D}}, E\right) \approx \left(1 - f_{\mathcal{D}}\right) \cdot \mathcal{M}(E) + f_{\mathcal{D}} \cdot \mathcal{D}(E) \quad , f_{\mathcal{D}} \in [0, 1]\,. \qquad (3.1)$$

Consequently, intersections of all spectra belonging to this growth stage arise at specific energies E_i where $\mathcal{M}(E_i) = \mathcal{D}(E_i)$. These so-called isosbestic points are indicative for a (physical) equilibrium reaction between two absorbing species. However, unlike in the case of PTCDA on mica, it is not an expression of the monomer–dimer transition here due to the lack of monomeric spectra in the first place. One could more precisely employ the term monomer*– dimer* transition, where the asterisks symbolize the hybridized character of the QT layers. Yet, we conclude that Figure 3.4 indeed provides evidence for a layer-by-layer growth, since there are further isosbestic points for $d > 2\,\mathrm{ML}$ at different energies, stemming from the transition to oligomers in quasi-one-dimensional stacks.

It is worth noting that the *ex situ* recorded optical absorbance of a poly-crystalline QT film a few nanometers thick on mica significantly differs from the final ε'' spectrum in Figure 3.4. Therefore, the film structure of QT on Au(111) can not be bulk-like. Instead, the red-shifted position (by $\approx 0.3\,\mathrm{eV}$) of the $\approx 4\,\mathrm{ML}$ spectra points toward stronger relaxation and is therefore a further hint toward the layered growth with flat-lying molecules assumed.

Film Structure. In the analysis of the optical spectra and their development for QT films grown on Au(111), we have come across a number of arguments supporting a layered growth mode with the molecular planes lying parallel to the substrate surface. Such a thin film growth would be in contrast to the bulk crystal structure in which no planes exist that are exclusively composed of flat-lying molecules, as opposed to, e.g., PTCDA. Hence, we are dealing with a substrate-induced growth which has nicely been confirmed by LEED and STM measurements [133, 146, 147]. The epitaxial structures of the first monolayer were thoroughly analyzed, yielding two-dimensional unit cell parameters summarized in Table 3.2. The adsorption of QT further leads to a modification of the $\left(22 \times \sqrt{3}\right)$-Au(111) reconstruction to a Au(111) surface with a $\left((25 \pm 1) \times \sqrt{3}\right)$ reconstructed unit cell. For all three structures differing only by their domain angles the epitaxial relations were identified as point-on-line (cf. Section 2.5.2). These findings were further backed by advanced potential energy calculations [148, 149] enabling an energetic explanation for the observed structures [147]. Representative STM images are shown in Figure 3.5.

Remarkably, the unit cell parameters of the second QT layer on Au(111) differ noticeably from those of the first [146, 147]. There, the unit cell vectors were determined as $||\mathbf{b}_1|| = (11.9 \pm 0.4)\,\mathrm{\AA}$, $||\mathbf{b}_2|| = (39.3 \pm 1.1)\,\mathrm{\AA}$, with a unit cell angle of $\beta = (78 \pm 1)^\circ$. The unit cell comprises two flat-lying and two upstanding molecules that are alternately arranged in double rows. Such a structure would clearly contradict the findings in the optical measurements described above, where we concluded a layer-by-layer growth with molecular

Table 3.2: Unit cell parameters of the first QT monolayer on Au(111): unit cell vectors $\mathbf{a}_1$ and $\mathbf{a}_2$, unit cell angle α, an angle ζ describing the azimuthal orientation of the QT mirror axis m_1 (perpendicular to the molecule's long axis) with respect to $\mathbf{a}_1$, and domain angle δ, i.e., the angle between the $[\overline{1}\,\overline{1}\,2]_{\mathsf{Au}}$ direction and $\mathbf{a}_1$. The unit cell contains 1 molecule. The epitaxy matrices $\underline{C}$ are given with respect to the Au(111) surface modified by the $\left((25 \pm 1) \times \sqrt{3}\right)$ reconstruction. Adapted from Refs. [146, 147].

$\|\mathbf{a}_1\|$ (Å)	$\|\mathbf{a}_2\|$ (Å)	α (°)	ζ (°)	δ (°)	$\underline{C}$
8.9 ± 0.3	19.6 ± 0.6	78 ± 1	2 ± 2	26 ± 1	$\begin{pmatrix} 0.192 & 3 \\ -7.790 & 6 \end{pmatrix}$
8.9 ± 0.3	19.6 ± 0.6	78 ± 1	2 ± 2	34 ± 1	$\begin{pmatrix} -0.332 & 3.332 \\ -8.114 & 5.114 \end{pmatrix}^{*}$
8.9 ± 0.3	19.6 ± 0.6	78 ± 1	2 ± 2	86 ± 1	$\begin{pmatrix} -3 & 3.371 \\ -6 & -1.436 \end{pmatrix}$

*Note that despite the absence of a column of integers this structure is also point-on-line coincident with the substrate lattice (cf. Ref. [18]).
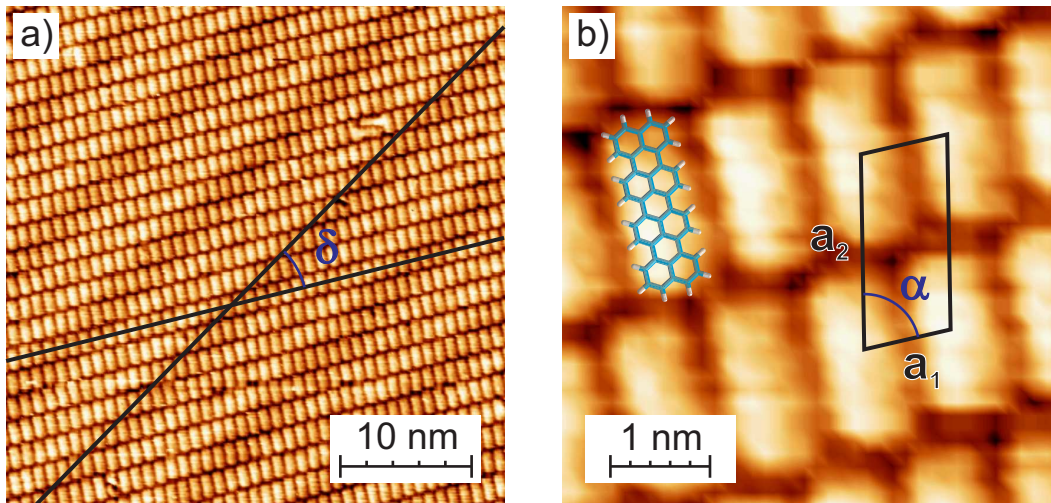

Figure 3.5: STM data of $1\,\mathrm{ML}$ of QT on Au(111) [133]. **a)** Survey scan, $38 \times 38\,\mathrm{nm}^2$, $1.6\,\mathrm{V}$, $100\,\mathrm{pA}$. Two lines mark the $[\overline{1}\,\overline{1}\,2]_{\mathsf{Au}}$ direction and the $\mathbf{a}_1$ direction, respectively. The domain angle $\delta = 34°$ is also indicated. **b)** Closeup view of the scan shown in (a), $5 \times 5\,\mathrm{nm}^2$. The unit cell is given, and a stick model of the QT molecule is superimposed.

planes parallel to the substrate surface. However, these discrepancies can be readily explained by the quite dissimilar growth conditions: QT was deposited on Au(111) heated to $100\,°\mathrm{C}$ in Refs. [146, 147], while the substrates were kept at room temperature here. In fact, many STM images may also be interpreted as face-to-face stacked double layers without upstanding molecules (cf. Figure 3.6), and several distinct film structures of the second QT layer on Au(111) might occur. In any case, the structure of the second QT layer
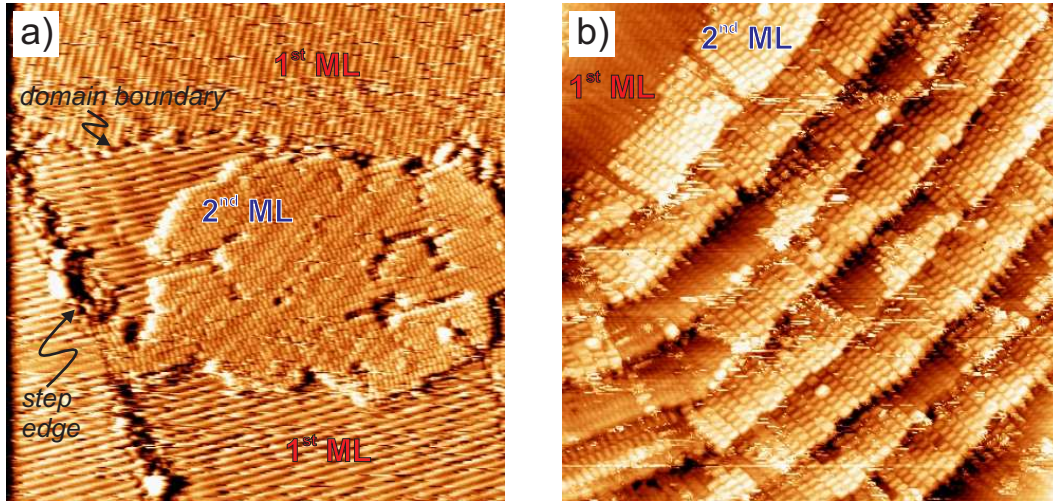
Figure 3.6: STM data of QT double layers on Au(111). **a)** QT thickness $d \approx 1.3\,\mathrm{ML}$, $\approx 150 \times 150\,\mathrm{nm}^2$, $-0.9\,\mathrm{V}$, $50\,\mathrm{pA}$. The molecules in the 1st ML are not individually resolved, but the characteristic QT rows can be seen. These rows are bent at domain boundaries of the gold substrate. The 2nd ML starts growing as an island on top of the 1st ML. Molecular resolution is achieved in the 2nd ML, and all molecules lie flat. **b)** $d \approx 1.8\,\mathrm{ML}$, $\approx 100 \times 100\,\mathrm{nm}^2$, $1.0\,\mathrm{V}$, $60\,\mathrm{pA}$. The first two layers can be imaged with molecular resolution revealing no upstanding molecules. Many gold step edges are contained in this scan. The QT unit cells in the 2nd ML appear slightly enlarged compared to the 1st ML. These data courtesy of Christian Wagner and Moritz Esslinger.

appears to be relaxed, i.e., its unit cell dimensions are slightly larger compared to the first ML.

3.3   QT on Graphite: Intermediate Coupling

Film Structure.   For an elucidation of the QT film structure on graphite, we performed LEED measurements. Figure 3.7 shows images obtained for bare single crystalline graphite along with a graphite surface covered with $\approx 1\,\mathrm{ML}$ of QT. The LEED pattern can be fully explained by just one QT film structure taking into account the substrate symmetry, of course.

The LEED patterns were analyzed by means of `LEEDSim`. The result of a kinematic simulation is depicted in Figure 3.7c, showing a variation of spot intensities as they find a qualitative correspondence in the measurement. Several images recorded at different primary electron energies were taken into consideration, which increases the accuracy of the simulation by including higher order LEED spots. The extracted unit cell parameters are summarized in Table 3.3. On the basis of the epitaxy matrix $\underline{C}$ we can identify the QT monolayer structure as point-on-line coincident with the graphite substrate.

Obviously, the key parameters of the unit cell (i.e., $\mathbf{a}_1$, $\mathbf{a}_2$, and α) are very similar to the ones reported for the first ML on Au(111). The respective
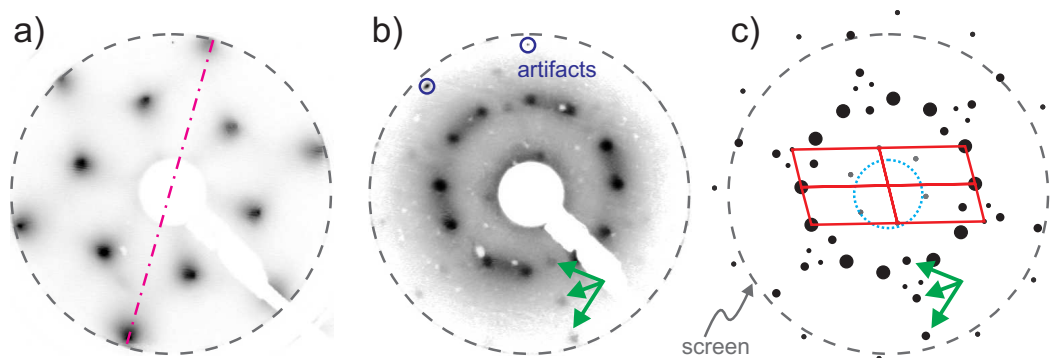
Figure 3.7: LEED images of **a)** single crystalline graphite, recorded at $E_{\text{primary}} = 189.2\,\text{eV}$, and **b)** $1\,\text{ML}$ of QT deposited on the same graphite sample, recorded at $E_{\text{primary}} = 13.0\,\text{eV}$. **c)** Corresponding kinematic simulation of the LEED pattern in (b) using `LEEDSim`. The diameters of the simulated LEED spots qualitatively correspond to the calculated intensities. Three representative spots of moderate intensity which are still fairly resolvable in the measurement are highlighted by green arrows. Expected spots in the proximity of the LEED gun are most likely predominated by the diffuse background originating from the intense (0,0)-spot in the center. Reciprocal QT unit cells are marked by red solid lines. One substrate symmetry axis is marked by the dash-dotted magenta line. Artifacts that did not vary with the primary energy were present in the measurement, highlighted with blue circles.

intermolecular distances are almost identical within the experimental accuracy. With such a high degree of resemblance concerning the thin film structures, one may expect many similarities concerning the optical behavior: In both cases the in-plane dimerization should be negligible due to the molecule–molecule separation being as large as $\approx 0.9\,\text{nm}$, resulting in a very inefficient overlap of the molecular π-orbitals within the monolayer.

Unfortunately, meaningful STM images could not be obtained for QT on graphite (or HOPG). This might be in part due to a high lateral mobility of perhaps rather loosely bound molecules on the surface, rendering room tem-

Table 3.3: Unit cell parameters of the first QT monolayer on single crystalline graphite: unit cell vectors $\mathbf{a}_1$ and $\mathbf{a}_2$, unit cell angle α, an angle ζ describing the azimuthal orientation of the QT mirror axis m_1 (perpendicular to the molecule's long axis) with respect to $\mathbf{a}_1$, and domain angle δ (measured between $[1\,0]$-directions of substrate and adsorbate). The unit cell contains 1 molecule. The epitaxy matrix $\underline{C}$ is given with respect to the graphite substrate lattice.

$\lVert\mathbf{a}_1\rVert$ (Å)	$\lVert\mathbf{a}_2\rVert$ (Å)	α (°)	ζ (°)	δ (°)	$\underline{C}$
8.8 ± 0.2	19.7 ± 0.4	77 ± 1	-10 ± 5	0 ± 1	$\begin{pmatrix} 0 & 3.579 \\ 9 & -2.695 \end{pmatrix}$

perature STM measurements complicated. In addition, there seems to exist a more general difficulty for the acquisition of STM scans with molecular resolution of unsubstituted polycyclic aromatic hydrocarbons on graphite surfaces, which may also be assumed from, e.g., Refs. [41, 150]. In these examples, HBC molecules were imaged, but their typical "snowflake" shape could not be recognized from the data even for closed monolayers. Features belonging to the HBC molecule exhibiting unit cell periodicity were reported instead. Such an obscuring effect might also occur for QT on graphite.

Differential Reflectance Spectra.   The DR spectra of QT films grown on freshly cleaved graphite (HOPG) are shown in Figure 3.8. As in the case on Au(111), three subsequent growth stages are marked with different colors. This might not be obvious at first glance, but will be justified in Figure 3.9. It can be seen that positive and negative parts in the DR spectra occur simultaneously, which demonstrates that the DRS can not be straightforwardly interpreted as the absorbance behavior on opaque substrates. Instead, the dielectric function has to be extracted using the `fit-nk` algorithm. Furthermore and with even more critical impact, the absence of a clear tendency to zero of the DRS on both ends of the spectra renders a drift-correction very difficult, which is especially severe for the lowest coverages (highlighted in orange in Figure 3.8) where the signal-to-noise ratio is smaller. Given that the time-dependent drift recorded before and after deposition exhibits irregular (small) fluctuations, a thorough drift-correction is rather challenging, if possible at all.

Dielectric Function Extracted from DRS.   The dielectric function extracted from the DRS via `fit-nk` is shown in Figure 3.9. Again, this spectral series is divided into three different growth stages displayed separately.

For coverages up to $d \approx 1\,\mathrm{ML}$ the ε'' spectra resemble each other to a large extent (cf. upper panels of Figure 3.9). The monolayer spectrum consists in principal of a main peak at $1.74\,\mathrm{eV}$ and one apparent shoulder at $\approx 1.91\,\mathrm{eV}$. The energy difference between both equals $\approx 0.17\,\mathrm{eV}$ and compares favorably with the vibronic progression $\Delta E_{\mathrm{vibron}}$ resolved in absorbance spectra recorded in 1,2,4-trichlorobenzene [129]. The overall spectral shape indeed comes close to the monomeric character in dilute solution, apart from the broadening of our solid state spectra which must be caused by non-negligible interactions with the underlying substrate. In fact, graphite sheets exhibit π-orbitals above the terminating atomic layer possessing a real space analogy to the π-orbitals of QT. A considerable overlap of these π-orbitals is therefore possible when the molecules are brought into contact with graphite. However, the latter has an electronic structure different from that of QT due to its laterally almost infinitely extended sheets. One can thus not necessarily assume the interaction between QT and graphite to be as strong as between two face-to-face stacked
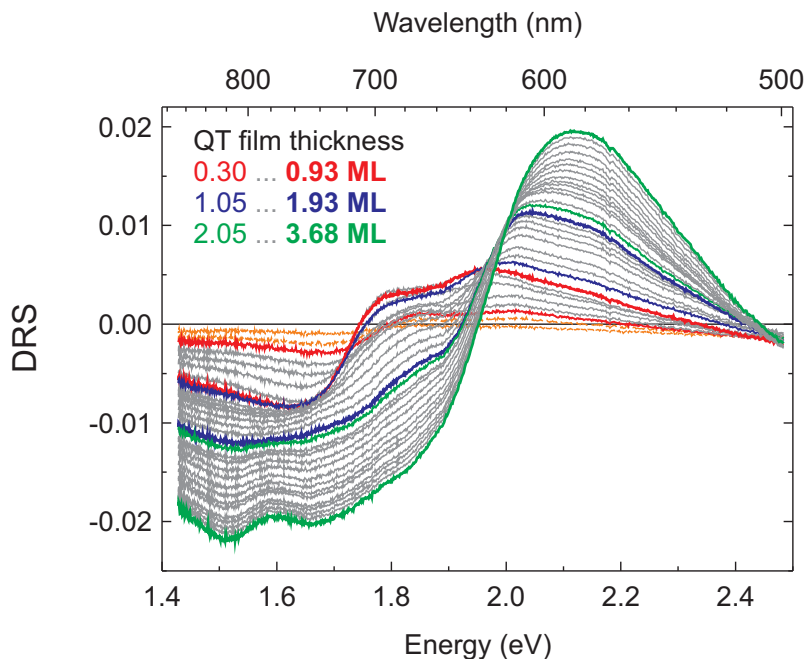
Figure 3.8: Differential reflectance spectra of QT deposited on graphite (HOPG). No drift-correction was carried out. The dashed orange curves represent QT film thicknesses of $0.05\,\mathrm{ML}$ and $0.18\,\mathrm{ML}$, respectively, and turned out to yield unreliable dielectric functions via `fit-nk` due to the rather low signal-to-noise ratio.

QT molecules, for example. It has previously been demonstrated by us for another planar aromatic molecule, namely HBC, that the ε'' spectra of the contact layer still bear monomeric character when deposited on HOPG, though with some broadening [82, 135]. We conclude that also the first monolayer of QT on graphite shows spectra with (broadened) monomer character. This circumstance is a confirmation of the negligible in-plane QT–QT interaction as deduced from the lateral thin film structure outlined above. The red-shift of the main spectral feature (and thereby of the entire spectra) from $1.79\,\mathrm{eV}$ (at $0.30\,\mathrm{ML}$) to $1.74\,\mathrm{eV}$ (at $0.93\,\mathrm{ML}$) can be explained by the increasing amount of molecules contributing to the dielectric background upon completion of the first ML. This dielectric screening effect has been observed and explained before for PTCDA films of similar thickness grown on mica [32, 76].

The deposition of QT beyond the first ML initiates a spectral development similar to that on Au(111) outlined in Section 3.2. From $d = 1\,\mathrm{ML}$ to $2\,\mathrm{ML}$, the most severe changes occur, as indicated by arrows in the center panels of Figure 3.9. The main feature in the ε'' spectra at $1.74\,\mathrm{eV}$ diminishes and the spectra broaden noticeably, while a new maximum is formed at $1.97\,\mathrm{eV}$. All the spectra in this thickness range can be approximated as a mixture between monomer spectrum $\mathcal{M}(E)$ and dimer spectrum $\mathcal{D}(E)$ with a steadily increasing fraction $f_{\mathcal{D}}$ of dimers, according to Equation (3.1). As on Au(111), intersections arise at specific energies E_i where $\mathcal{M}(E_i) = \mathcal{D}(E_i)$. These isos-
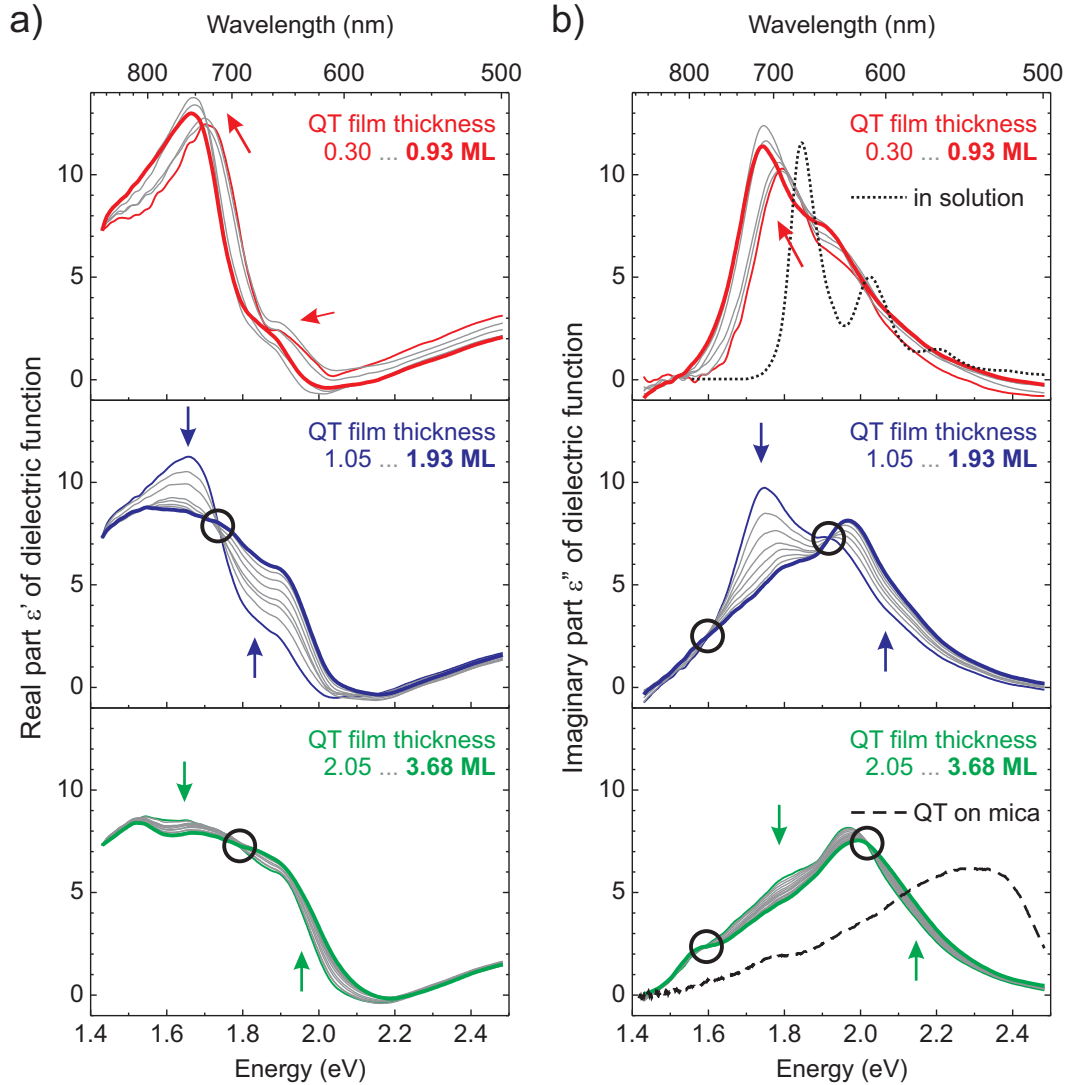
Figure 3.9: **a)** Real part ε', and **b)** imaginary part ε'' of the dielectric function $\hat{\varepsilon} = \varepsilon' - i\varepsilon''$ of QT deposited on graphite (HOPG) extracted from the DRS shown in Figure 3.8. Both spectral series are divided into three subsequent growth stages for clarity: *upper panels* $0\,\text{ML} < d < 1\,\text{ML}$, *center panels* $1\,\text{ML} < d < 2\,\text{ML}$, *bottom panels* $d > 2\,\text{ML}$. For comparison, the absorbance spectrum of QT dissolved in 1,2,4-trichlorobenzene is shown (dotted curve, not to scale) [129]. The final ε'' spectra of this series are compared to an *ex situ* recorded absorbance spectrum of QT on mica (dashed curve, not to scale), presumably in the polycrystalline bulk phase. The spectral development with increasing film thickness is indicated by arrows, the resulting isosbestic points are marked with circles.

bestic points are a sign of a (physical) equilibrium reaction, in this case indeed the monomer–dimer transition of face-to-face stacked QT layers, in contrast to the hybridized layers on Au(111).

Further spectral development takes place when the coverage exceeds 2 ML. The peak at 1.97 eV slightly shifts to 1.99 eV, and a low energy shoulder is

formed at $\approx 1.57\,\mathrm{eV}$. The progress is much less dependent on the film thickness than in between $1\,\mathrm{ML} < d < 2\,\mathrm{ML}$, and isosbestic points are found at different energies. The spectra quickly reach saturation at roughly $4\,\mathrm{ML}$. However, the final ε'' spectra in the bottom panels of Figure 3.9 differ significantly from the absorbance spectrum of a comparatively thick QT film on mica, presumably in the polycrystalline bulk structure. As on Au(111), this provides additional support for the layered growth with flat-lying molecules assumed.

Based on a number of arguments, we have demonstrated that the growth of thin QT films on Au(111) and graphite is rather similar, and that the respective film structures are almost identical. Consequently, the optical behavior exhibits many similarities (apart from the much stronger hybridization on Au(111)), and indeed the same strategies can be applied for the description of the spectral development with rising film thickness. It is an intriguing question whether a predeposited monolayer consisting of a *different* molecular species would influence the growth behavior of a QT film grown on top, but also to what extent it would have an impact on the physicochemical properties of QT, most notably on the observed more or less intense electronic coupling to the substrate. For this purpose, we have chosen HBC as the intermediate layer sandwiched between a Au(111) surface and a QT film on top, which will be addressed in Section 3.4.

3.4   QT on HBC on Au(111): Decoupling

Differential Reflectance Spectra.   With regard to the direct deposition of QT on Au(111), we performed a similar experiment except that here a single monolayer of flat-lying HBC [42] was deposited on the Au(111) surface before growing the QT film (cf. Figure 3.10). In this experiment the layer system "$1\,\mathrm{ML}$ of HBC on Au(111)" is regarded to represent a "new" substrate, being consequently characterized by a different $R^*(E, 0)$ which already incorporates the HBC layer. As in the case of QT, also the HBC states undergo hybridization upon adsorption on Au(111), consequently leading to a broadening of the molecular transitions, which is not shown here. In the following, we will elucidate whether this thin interlayer of a different molecular species would have a noticeable impact on the observed electronic coupling of QT to the metal substrate.

Dielectric Function Extracted from DRS.   Figure 3.11 shows the complex dielectric function obtained via `fit-nk` for differently thick QT films grown on top of such a closed HBC monolayer.

Up to a surface coverage of $\approx 1\,\mathrm{ML}$ of QT on HBC on Au(111), the ε'' spectra are very similar to those of QT dissolved in 1,2,4-trichlorobenzene with comparable peak widths ($0.12\,\mathrm{eV}$ vs. $0.09\,\mathrm{eV}$ in solution), where the
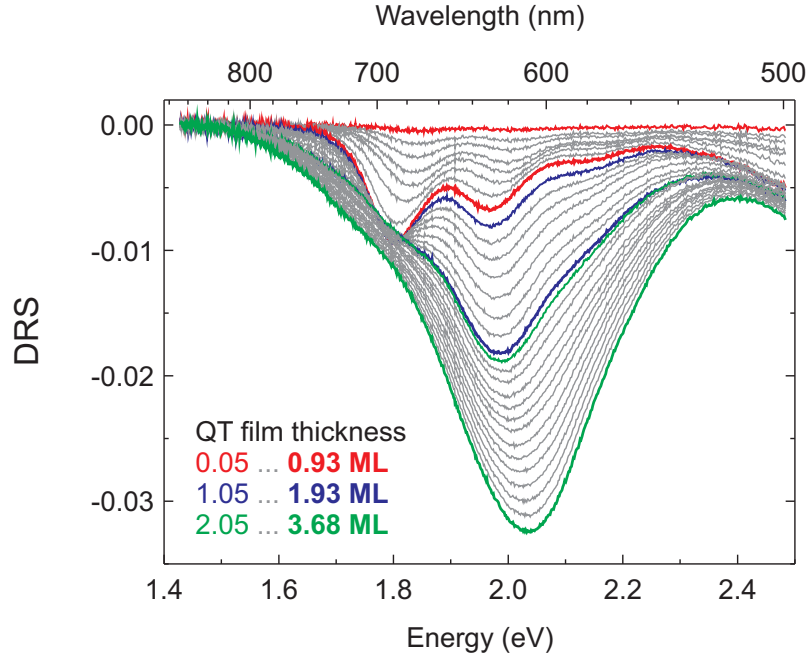
Figure 3.10: Drift-corrected differential reflectance spectra of QT deposited on
1 ML of HBC on Au(111).

three peaks belong to the $S_0 \rightarrow S_1$ transition with its vibronic progression.
The slight red-shift of the main ε'' feature of the QT monomer to $1.80\,\text{eV}$
with rising film thickness up to 1 ML is readily understood by the increasing
number of molecules contributing to the dielectric background, which directly
influences the peak position, as explained in Refs. [32, 76]. Thus, in contrast
to the case of QT directly grown on Au(111), we clearly observe monomers in
the first QT monolayer on HBC. Such spectra would be expected for flat-lying
QT molecules on inert, i.e., *non-metallic* substrates.

Moreover, it is important to realize that those spectra are also fundamen-
tally different from the second QT layer directly on Au(111), even though
1 ML of HBC and 1 ML of QT have an identical thickness, and both molecules
are planar polycyclic aromatic hydrocarbons. To highlight this finding, we
also calculated the dielectric function of the second ML of QT with respect
to the layer system "1 ML of QT on Au(111)", regarding the first QT layer
as part of the substrate (dash-dotted curve in the center panel of Figure 3.4).
If coupling between the adjacent QT monolayers were as weak as between
adjacent QT and HBC monolayers (Section 3.2 vs. Section 3.4), one would
also observe monomeric spectra there due to the similar geometric arrange-
ment of the regarded QT monolayer on top of the two different intermediate
layers considered. However, the comparison to the absorbance measured in
1,2,4-trichlorobenzene reveals no such resemblance as opposed to QT films on
a similarly thick HBC monolayer. Hence, we observe rather strong coupling of
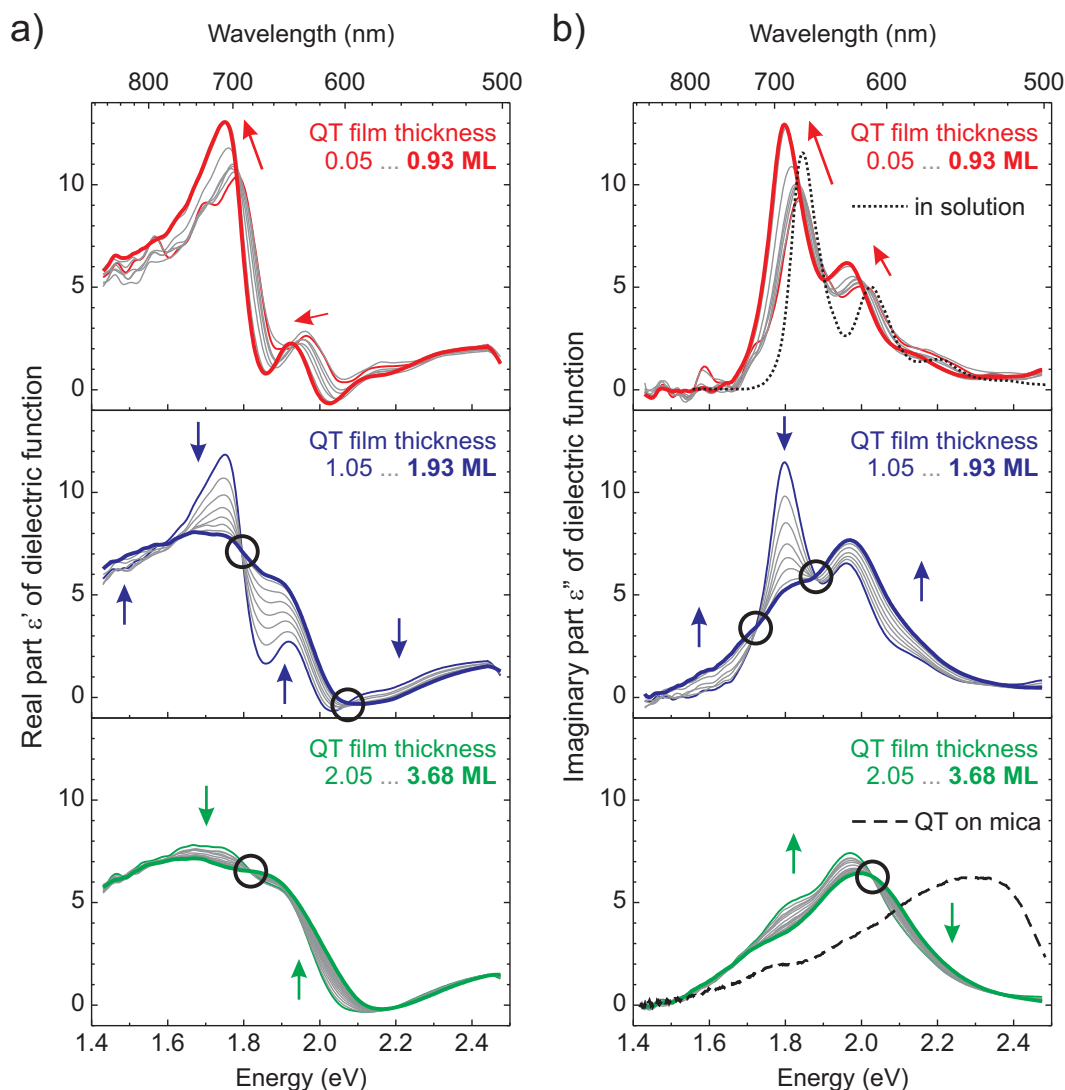the second QT monolayer to the first one on Au(111). Unlike for the case of

Figure 3.11: **a)** Real part ε', and **b)** imaginary part ε'' of the dielectric function $\hat{\varepsilon} = \varepsilon' - i\varepsilon''$ of QT deposited on $1\,\mathrm{ML}$ of HBC on Au(111) extracted from the DRS shown in Figure 3.10. Both spectral series are divided into three subsequent growth stages for clarity: *upper panels* $0\,\mathrm{ML} < d < 1\,\mathrm{ML}$, *center panels* $1\,\mathrm{ML} < d < 2\,\mathrm{ML}$, *bottom panels* $d > 2\,\mathrm{ML}$. For comparison, the absorbance spectrum of QT dissolved in 1,2,4-trichlorobenzene is shown (dotted curve, not to scale) [129]. The final ε'' spectra of this series are compared to an *ex situ* recorded absorbance spectrum of QT on mica (dashed curve, not to scale), presumably in the polycrystalline bulk phase. The spectral development with increasing film thickness is indicated by arrows, the resulting isosbestic points are marked with circles.

an intermediate HBC layer, the electronic coupling to the metal is most likely not suppressed by the intermediate QT layer. In addition, one should point out that the (hybridized) QT states of the first monolayer and the states of the QT molecules in the second layer occur at roughly the same energy (having at least a noticeable energetic overlap) and hence can interact – quite contrary to

the case of a HBC interlayer. We conclude that already one HBC monolayer decouples the QT from the Au(111) surface, and that this effect is not merely due to the thickness of the intermediate layer.

The ε'' spectra between 1 ML and 2 ML of QT on HBC (center panel in Figure 3.11b) can be approximately described by Equation (3.1). Here, $\mathcal{M}(E)$ undoubtedly corresponds to the monomer spectrum turning into the dimer spectrum $\mathcal{D}(E)$ with a steadily increasing fraction $f_\mathcal{D}$ of dimers, thereby attenuating the observed fraction $f_\mathcal{M}$ of monomers. The very sharp isosbestic points at 1.73 eV and 1.88 eV associated with this distinct spectral development clearly indicate the monomer–dimer transition of flat-lying face-to-face stacked QT layers. Therefore, it is anticipated that also the second monolayer of QT on HBC consists of flat-lying molecules, each forming a stacked dimer with an underlying QT molecule.

In the third and fourth monolayers, the spectral shape very quickly saturates with increasing film thickness, and the influence of the substrate is already almost lost at around 4 ML (bottom panels Figure 3.11). Once again, the final ε'' spectra differ noticeably from the absorbance of a comparatively thick polycrystalline QT film on mica. Since the latter is presumably in the bulk crystal phase, this can not be the case for the thin QT film on HBC on Au(111). The red-shifted position (by ≈ 0.3 eV) of the ≈ 4 ML spectra points toward stronger relaxation and is therefore a further indication for the layered growth assumed.

Film Structure.   Quite naturally, one could suspect different QT film structures of being responsible for the dissimilar optical behavior. However, the QT film structure on top of the HBC monolayer (Figure 3.12) is rather similar to that of QT grown directly on Au(111) (Figure 3.5). The double layer structure of the sample depicted in Figure 3.12 can be unambiguously evidenced by a Fast Fourier Transform (FFT) of this STM image (Figure 3.13d) which clearly shows contributions of the two different molecular lattices. Combining these results with a LEED analysis (Figure 3.13a-c), we found that the QT film on top of the HBC monolayer on Au(111) consists of flat-lying molecules with the lattice parameters summarized in Table 3.4.

These unit cell vectors are almost identical to those of QT directly on Au(111) [146, 147]. We would like to point out here that the observed heteroepitaxy constitutes a new example of the recently found most general form of epitaxy, the so-called line-on-line coincidence (cf. Section 2.5.2). It is characterized by a coincidence between non-primitive reciprocal lattice vectors of the substrate and the overlayer, in this case the HBC [2 $\bar{1}$] and the QT [2 1] reciprocal lattice vectors. Since both reciprocal lattices are simultaneously visible in a LEED pattern (or in a FFT of a STM image), this assignment can be made with much higher accuracy than the determination of the lattice
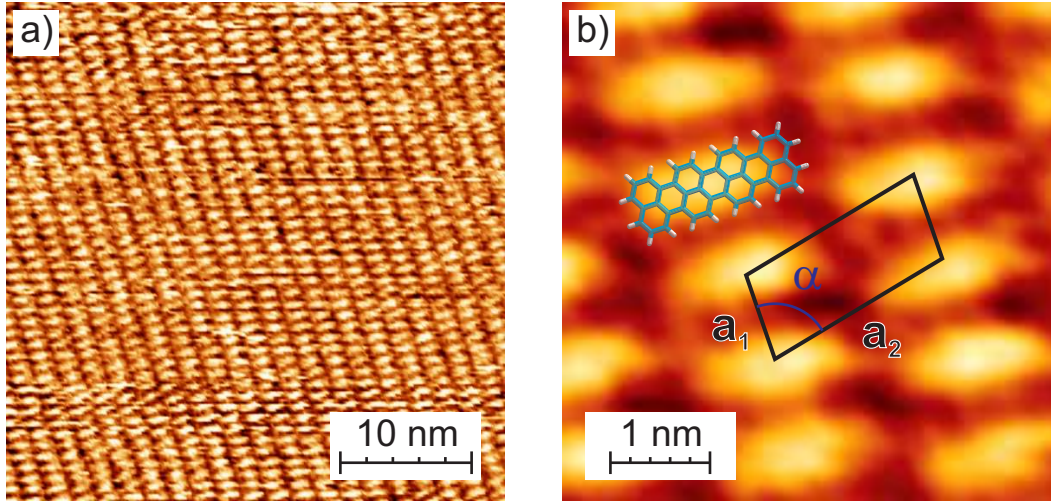
Figure 3.12: STM data of $1\,\mathrm{ML}$ of QT on $1\,\mathrm{ML}$ of HBC on Au(111) [133]. **a)** Survey scan, $38 \times 38\,\mathrm{nm}^2$, $1.0\,\mathrm{V}$, $70\,\mathrm{pA}$. **b)** Closeup view of the scan shown in (a), $5 \times 5\,\mathrm{nm}^2$, filtered. The unit cell is given, and a stick model of the QT molecule is superimposed.

Table 3.4: Unit cell parameters of the first QT monolayer on $1\,\mathrm{ML}$ of HBC on Au(111): unit cell vectors $\mathbf{a}_1$ and $\mathbf{a}_2$, unit cell angle α, an angle ζ describing the azimuthal orientation of the QT mirror axis m_1 (perpendicular to the molecule's long axis) with respect to $\mathbf{a}_1$, and domain angle δ (measured between $[1\,0]$-directions of QT and HBC). The unit cell contains 1 molecule. The epitaxy matrix $\underline{C}$ is given with respect to the underlying HBC lattice ("$0\,^\circ$-structure") [133].

$||\mathbf{a}_1||$ (Å)	$||\mathbf{a}_2||$ (Å)	α (°)	ζ (°)	δ (°)	$\underline{C}$
9.4 ± 0.2	20.9 ± 0.4	77 ± 1	n/a	-47 ± 1	$\begin{pmatrix} -0.71 & 0.56 \\ 0.19 & 1.39 \end{pmatrix}$

constants itself, being not influenced by any absolute scaling. Details of the epitaxial analysis are given elsewhere [151].

Due to the similarity of the observed QT structures on $1\,\mathrm{ML}$ of HBC on Au(111) and directly on Au(111), we can rule out that the discussed spectral differences are a result of structural effects. Recalling that also the second QT layer on $1\,\mathrm{ML}$ of QT on Au(111) does not exhibit monomeric spectra, it is clear that the different behavior of the two systems must indeed be caused by different interactions with the respective substrates. This is a direct consequence of the different electronic band gap of HBC compared to that of QT (energetically lowest absorption peaks in 1,2,4-trichlorobenzene: $E_{\mathrm{opt,\,HBC}} = 2.68\,\mathrm{eV}$ and $E_{\mathrm{opt,\,QT}} = 1.85\,\mathrm{eV}$, compare Figure 3.1). For an accurate description of the interface energetics, we performed UPS measurements for the systems "QT
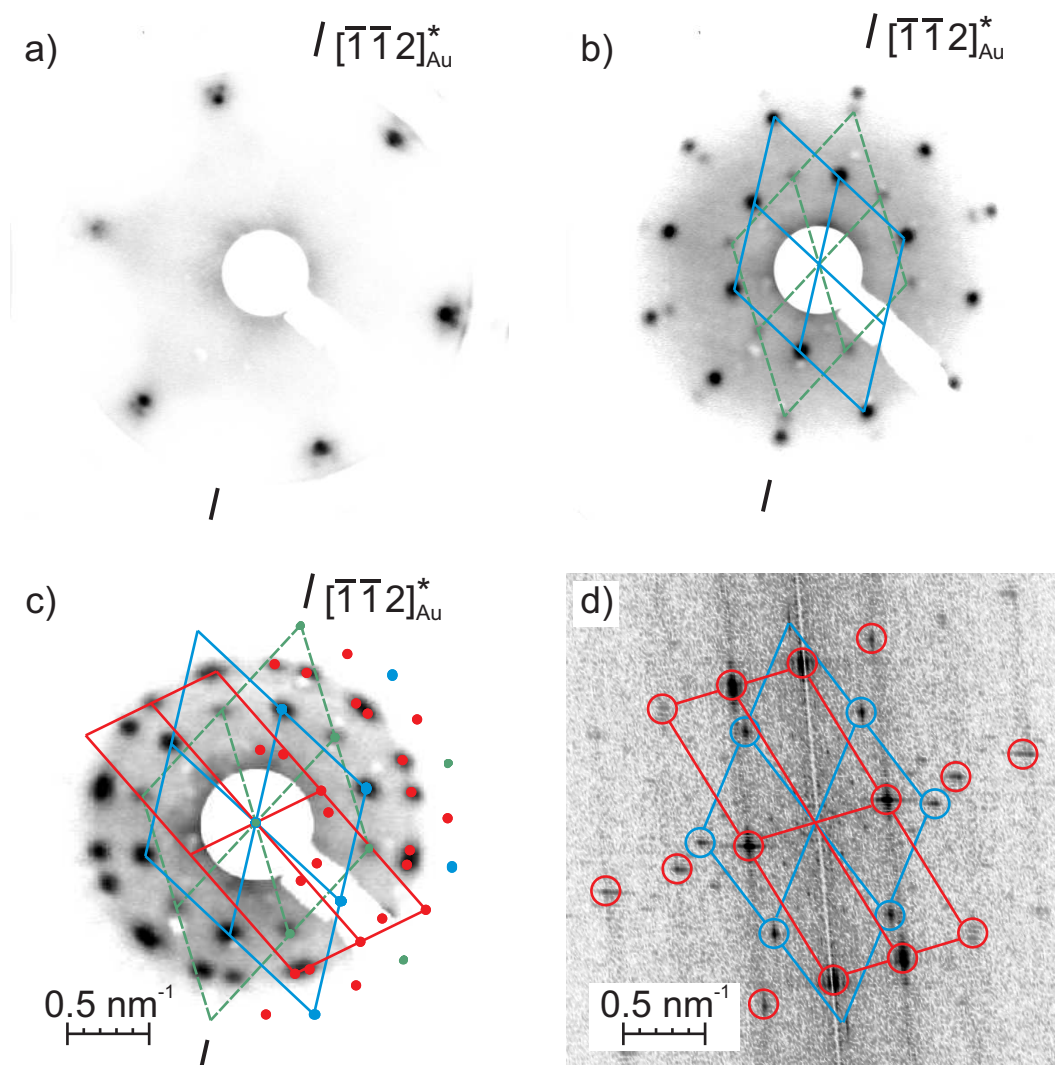
Figure 3.13: **a)** LEED image of the bare Au(111) sample before deposition of molecules, recorded at $E_{primary} = 58.0\,\text{eV}$. The $[\bar{1}\bar{1}2]^{\star}_{Au}$ direction is indicated. The surface reconstruction can be recognized by the additional speckles around the first order spots. **b)** LEED image of $1\,\text{ML}$ of HBC deposited on Au(111), recorded at $E_{primary} = 11.0\,\text{eV}$. Two different HBC orientations are present, highlighted in green ("30°-structure") and blue ("0°-structure"), respectively. **c)** LEED image of $1\,\text{ML}$ of QT on $1\,\text{ML}$ of HBC on Au(111), recorded at $E_{primary} = 11.0\,\text{eV}$. This image is slightly enlarged in order to match the scale in (d). The overlay depicts a simulation using `LEEDSim` (shown for the right half of the image, only). Reciprocal unit cells are highlighted in the same colors as in (b), spots associated with the QT lattice are marked in red. **d)** Fast Fourier Transform (FFT) of the STM image shown in Fig. 3.12a. The sample orientations in LEED and STM are different. QT grows preferentially on the "0°-HBC-structure", since the "30°-HBC-structure" is not present.

on Au(111)" and "QT on HBC on Au(111)", in order to determine the role of the HBC spacer layer. This will be the subject of Section 3.5.

3.5   Electronic Structure

We reasoned in Section 3.4 that the HBC spacer layer of only 1 ML on Au(111) causes an efficient decoupling effect for QT films grown on top. This was based on conclusions drawn solely from the optical data. For a more thorough analysis of the electronic properties of the systems "QT on Au(111)" and "QT on HBC on Au(111)", it is advisable to perform photoelectron spectroscopy measurements.* For these experiments *pc* Au samples were favored over the more demanding Au(111) since surface structure and crystallinity could not be analyzed. Yet, film structures are assumed to be similar on Au(111) and *pc* Au. In the following, we will discuss the obtained UPS data for both systems.
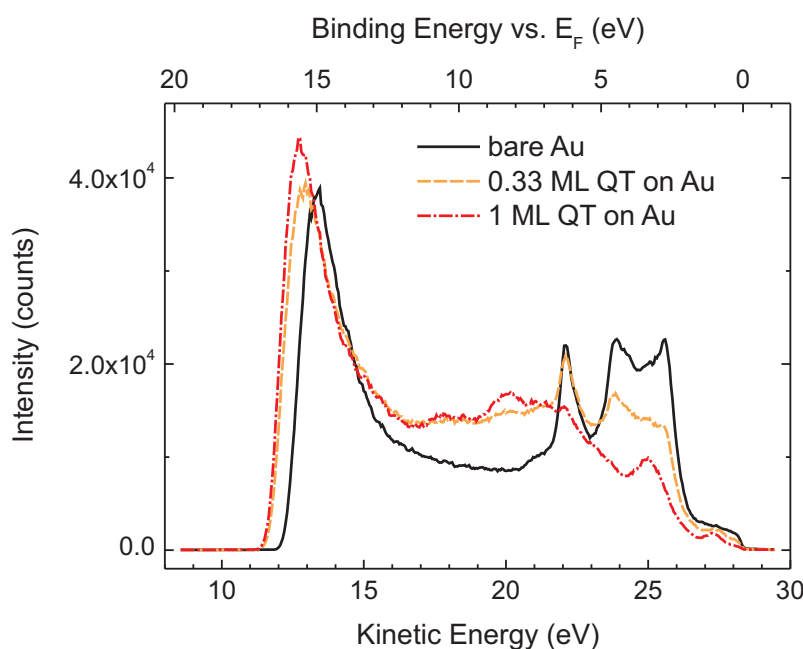

Figure 3.14: UPS data (full scans) of QT deposited on *polycrystalline* Au, in analogy to Figure 2.14. The UV light source is a He-I discharge lamp ($h\nu = 21.22\,\text{eV}$). An additional sample bias of $-5.00\,\text{V}$ was applied.

Figure 3.14 depicts the full UPS scans of a bare polycrystalline (*pc*) gold sample in comparison with $0.33\,\text{ML}$ and $1\,\text{ML}$ of QT on Au, respectively. The gold Fermi edge can be seen at a kinetic energy of $E_\text{k} = 28.33\,\text{eV}$. The high binding energy cutoff (HBEC) of the bare gold sample is at $12.24\,\text{eV}$, which yields a reasonable gold workfunction of $\Phi_\text{Au} = 5.13\,\text{eV}$ with $h\nu = 21.22\,\text{eV}$ (He-I). Upon deposition of QT, the Au-5d bands at low binding energies are attenuated, and new features related to the molecular orbitals emerge. At the same time, the HBEC exhibits a quite abrupt shift, i.e., an interface dipole

---

*The equipment required for this purpose was unavailable in our group. However, the author of this thesis was kindly invited by Prof. Neal R. Armstrong to join his research group at the University of Arizona for several weeks of collaborative research in order to record XPS and UPS data of our systems.
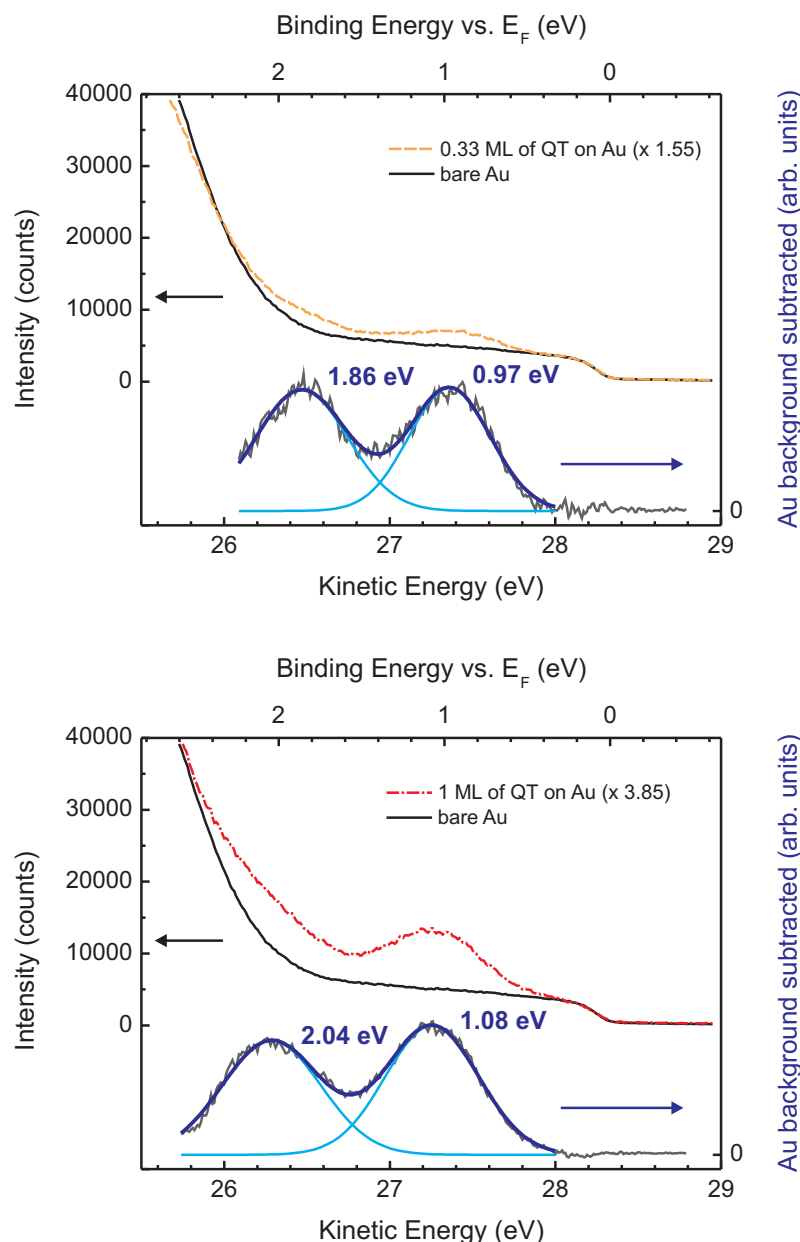
Binding Energy vs. E_F (eV)

Intensity (counts)

Au background subtracted (arb. units)

0.33 ML of QT on Au (x 1.55)
bare Au

1.86 eV   **0.97 eV**

Kinetic Energy (eV)

Binding Energy vs. E_F (eV)

Intensity (counts)

Au background subtracted (arb. units)

1 ML of QT on Au (x 3.85)
bare Au

2.04 eV   **1.08 eV**

Kinetic Energy (eV)

Figure 3.15: Closeup view of the high kinetic energy side of the UPS data shown in Figure 3.14. Here, the spectra of $0.33\,\mathrm{ML}$ and $1\,\mathrm{ML}$ of QT on Au were multiplied with 1.55 and 3.85, respectively, in order to account for the attenuation of the Au spectrum upon deposition of molecules. These factors were adjusted such that the gold Fermi edge is matched as closely as possible. The corresponding residuals are plotted as dark gray curves on different scales, vertically offset for clarity, and were further fitted with Gaussian functions drawn in blue. The binding energies with respect to E_F are indicated.

of $\approx 0.6\,\mathrm{eV}$ is formed. The secondary electron peak at low kinetic energies simultaneously rises with the "contamination" of the Au surface. The features in the proximity of the Fermi edge (high kinetic energies) are of particular interest since they map the occupied density of molecular states formed during film growth. A closeup view of this region is depicted in Figure 3.15. The

absolute scaling of these graphs is not strictly meaningful, as the sample had to be transferred from the analysis chamber to the growth chamber for each deposition step, which did not allow for entirely reproducible sample positions during UPS. After adequate subtraction of the Au derived photoemission features, two peaks remain in the proximity of the Au Fermi edge which are attributed to the HOMO and HOMO−1, respectively. They were fitted with Gaussian curves as a function of the QT film thickness, cf. Figure 3.15.
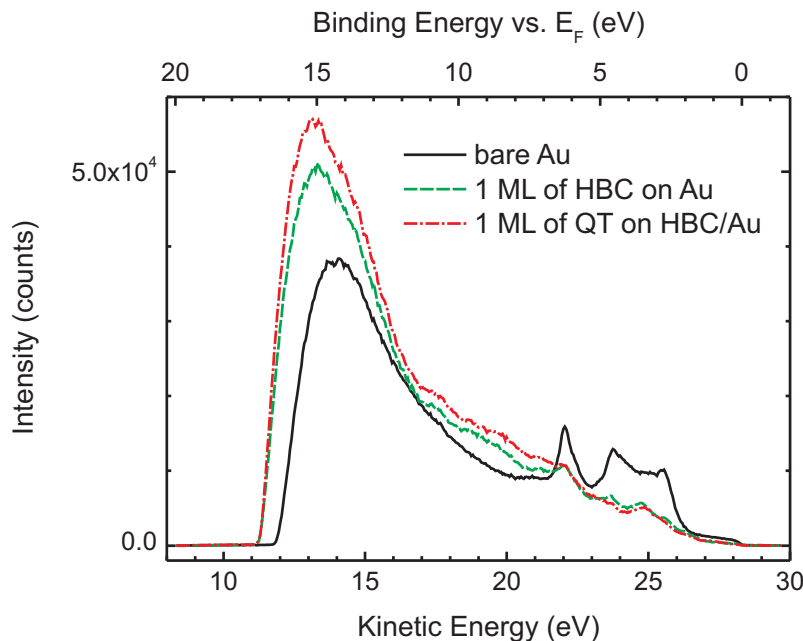

Figure 3.16: UPS data (full scans) of QT deposited on HBC on *polycrystalline* Au, in analogy to Figure 2.14. The UV light source is a He-I discharge lamp ($h\nu = 21.22\,\text{eV}$). An additional sample bias of $-5.00\,\text{V}$ was applied.

In a second step, monolayers of HBC and QT were subsequently grown on polycrystalline Au and examined with UPS. It can already be seen in Figure 3.16 that the UPS signal of the bare Au surface showed some odd variation compared to Figure 3.14. While the gold Fermi edge lies at a kinetic energy of $E_\text{k} = 28.30\,\text{eV}$, the high binding energy cutoff (HBEC) of the bare gold sample is at $11.86\,\text{eV}$, which yields a gold workfunction of $\Phi_\text{Au} = 4.78\,\text{eV}$. This low value indicates either a remaining oxygen or carbon contamination (as also judged from XPS, not shown here), or a significant roughening of the surface and hence a net increase of the secondary electrons and thereby a broader low kinetic energy peak in the spectrum.[†] Consequently, the HBEC might occur at systematically too low energies, and the relative intensity of the Au-5d derived features at low binding energies is noticeably smaller. Still, we would like to

---

[†]Surface roughening is likely to be predominant, due to a thorough cleaning procedure prior to the measurements. Initially, the Au samples were etched with piranha solution (a mixture of sulfuric acid (H_2SO_4) and hydrogen peroxide (H_2O_2)). After transferring the Au samples to UHV, they were further sputtered with Ar^+ at $2\,\text{keV}$ for several $15\,\text{min}$ cycles.

present these data, since the level alignment in the proximity of the Au Fermi edge is believed to be hardly affected.

A closeup view of the high kinetic energy region of Figure 3.16 is shown in Figure 3.17. Again, the photoemission originating from the Au substrate was
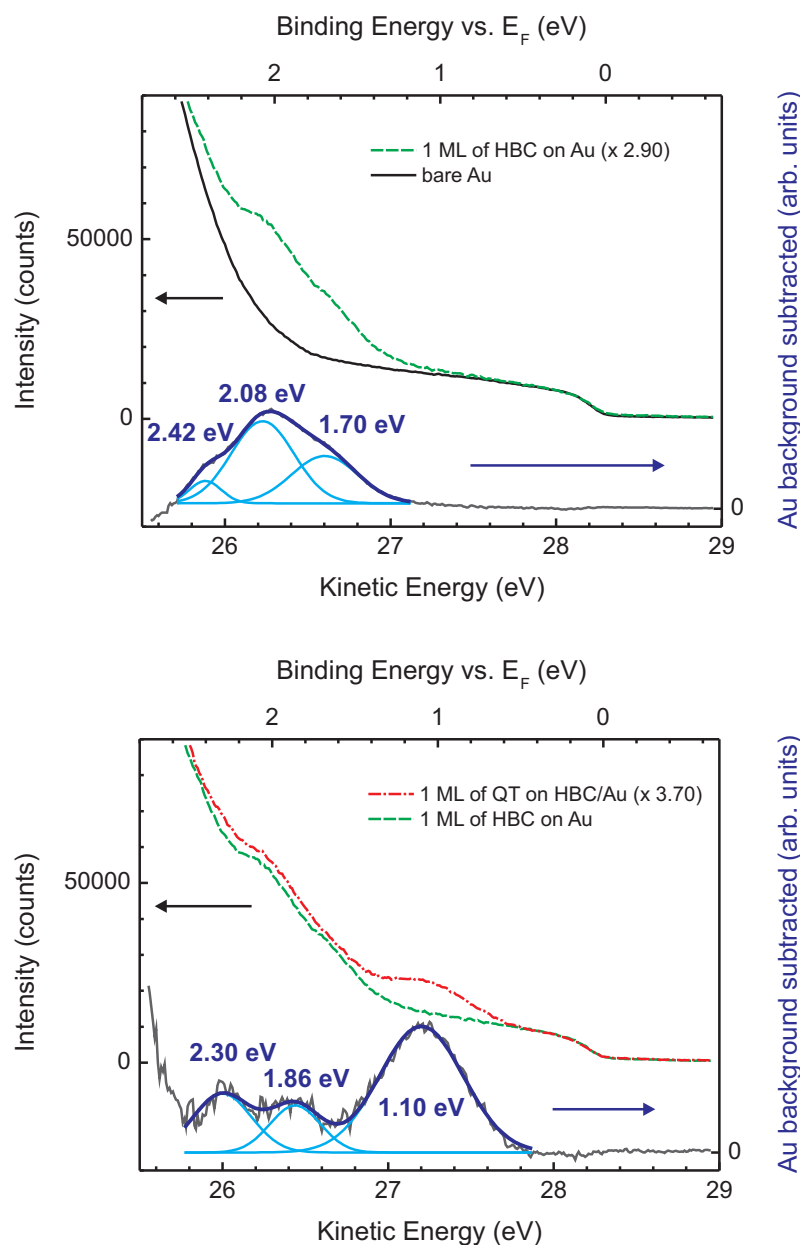

Figure 3.17: Closeup view of the high kinetic energy side of the UPS data shown in Figure 3.16. Here, the spectra of $1\,\mathrm{ML}$ of HBC and $1\,\mathrm{ML}$ of QT on HBC on Au were multiplied with 2.90 and 3.70, respectively, in order to account for the attenuation of the Au spectrum upon deposition of molecules. These factors were adjusted such that the gold Fermi edge is matched as closely as possible. The corresponding residuals are plotted as dark gray curves on different scales, vertically offset for clarity, and were further fitted with Gaussian functions drawn in blue. The binding energies with respect to E_F are indicated.

subtracted after adequate magnification of the corresponding spectra in order to match the gold Fermi edge as closely as possible. The obtained residuals were fitted with Gaussian functions. For 1 ML of HBC on Au, a triple peak at 1.70 eV, 2.08 eV, and 2.42 eV below E_F emerges which is most likely derived from the HOMO of the HBC film. These values compare favorably with a previous measurement of a 20 nm thick HBC film on polycrystalline Au [152] but differ significantly from the reported HOMO binding energy of a HBC multilayer on Au(111) of only 1.4 eV [134]. It is known that the morphology influences the electronic structure of thin HBC films on conductive surfaces, such as Au [153], but the exact film structure on our polycrystalline Au samples could not be checked due to the lack of structural analysis techniques at the UPS/XPS apparatus. We therefore assume the molecular arrangements to be similarly flat and densely packed as on Au(111).

Additional deposition of 1 ML of QT leads to the appearance of a main feature at 1.10 eV below E_F attributed to the QT HOMO. Evidently, the HOMO of the QT film on the HBC monolayer occurs at roughly the same binding energies as if deposited directly on Au (compare Figure 3.15). It does, however, not coincide with the broad feature originating from the HOMO of HBC, which suggests that an electronic decoupling effect from the Au surface is indeed favored. In addition, two smaller peaks at 1.86 eV and 2.30 eV below E_F are visible which probably stem from the QT HOMO-1 (or the HOMO-2) at a position where only one feature was observed for QT directly on Au. Unfortunately, it remains unclear whether there is a true splitting of such deeper lying QT levels or whether this could be caused by a pinning effect to the HOMO of the underlying HBC layer. From the HBEC one can confirm vacuum level alignment between QT and HBC, i.e., no additional interface dipole is formed between these two layers (cf. Figure 3.16). According to Ref. [23], vacuum level alignment was assumed to be a general law for organic films until the mid 1990s. Their surfaces, which consist of closed-shell molecular entities were believed to hardly interact electronically with substrates. Despite the fact that this assumption fails for strongly interacting surfaces, such as metals, vacuum level alignment between two adjacent molecular layers still hints toward weak electronic coupling [23]. These arguments considered, we conclude that an electronic decoupling effect between HBC and QT is very likely, but can not be evidenced with absolute certainty from these UPS data, since the peak position and width of the QT HOMO did not change significantly upon inserting the HBC monolayer.

3.6   QT on Insulators: Minor Coupling

Having observed differently intense electronic coupling effects on conductive substrates up to now, we may suppose that almost complete electronic decou-

pling naturally occurs on insulating substrates, such as mica or quartz glass. Hence, on such surfaces we would expect the optical behavior of a QT monolayer to be monomer-like, provided that the molecules grow flat-lying with a rather large intermolecular separation, as demonstrated, e.g., for PTCDA on mica [32]. However, we will see in the following to what extent our expectations are met by the experimental results and how strong the QT growth modes influence its optical response. This constitutes a further consequent step toward the elucidation of the structure–properties-relations of thin molecular films.

QT on Mica.   Using an air-cleaved $95\,\mu$m thick muscovite mica sheet as a substrate, we recorded the DRS of QT films grown on this surface as depicted in Figure 3.18a. The nominal thicknesses are given here in equivalents of densely packed flat-lying monolayers, as encountered on Au(111), on graphite, or on HBC on Au(111). In Section 2.3 we had seen that the DRS on such a transparent substrate is to a good approximation proportional to the imaginary part of the adsorbate dielectric function (and hence to its absorbance behavior). However, the DRS of QT on mica reveals no resemblance to the monomer absorbance recorded in solution (cf. Figure 3.1), even for submonolayer coverage. Further, it is conspicuous that the spectral development changes abruptly once a critical film thickness of $\approx 2.3\,$ML (marked in red) is exceeded. These two growth phases will therefore be discussed separately in the following. We would like to point out here that the drift of the DRS recorded right before film growth is close to an ideally flat zero baseline (Figure 3.18b), while the non-vanishing drift signal immediately after film growth demonstrates a structural reordering of the QT film after the deposition (Figure 3.18c).

The ε'' spectra extracted from the DRS via `fit-nk` are shown in Figure 3.19. Up to a *nominal* thickness of $2.3\,$ML the spectra are rather broad and indeed very similar with a maximum at $\approx 2.10\,$eV and a shoulder at $\approx 1.85\,$eV. A slight red-shift can be observed upon increasing film thickness which can readily be explained by the developing dielectric background stemming from the growing number of molecules on the surface [32, 76]. No vibronic substructure is apparent, and in fact these spectra bear no resemblance with the absorbance recorded in 1,2,4-trichlorobenzene [129]. This optical behavior is in strong contrast to that of thin PTCDA films on mica [32, 76], and can only be explained by a fundamentally different film structure. If QT were to grow flat-lying on mica (as encountered on Au(111), on graphite, or on HBC on Au(111)), the ε'' spectra should be monomer-like, since the intermolecular separation would be large enough for the π–π-overlap to be rather inefficient (compare Section 3.4). The inert insulating mica surface itself does evidently not provide a sufficiently high electron density to cause electronic coupling of the QT film to the substrate. Likewise, the formation of three-dimensional QT islands or clusters is very unlikely, as in this case there would not be a critical
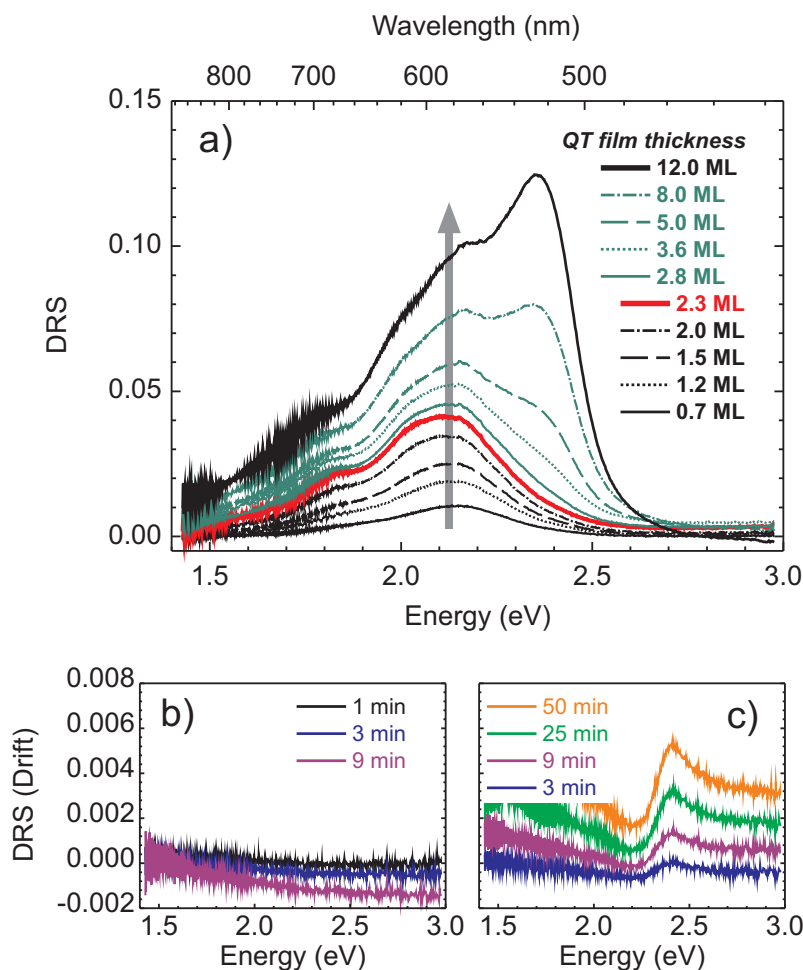
Figure 3.18: **a)** Differential reflectance spectra (DRS) recorded for QT films deposited on mica. The nominal thicknesses are given here in equivalents of densely packed flat-lying monolayers, as encountered on Au(111), on graphite, or on HBC on Au(111). The gray arrow indicates the development with increasing film thickness. **b)** Drift of the DRS signal right before film growth being close to an ideally flat zero baseline. **c)** Drift of the DRS signal immediately after film growth (same scale as in (b)). The non-vanishing signal demonstrates a structural reordering of the QT film after the deposition.

thickness at which the spectral development completely shifts gears. Instead, we interpret this spectral series as a growth divided into two subsequent stages.

In *stage 1* (up to 2.3 ML, Figure 3.19a), the molecules already aggregate as evidenced by the absence of monomer spectra with vibronic progression. This might be caused by an edge-on growth, i.e., the QT long edge is assumed to be in contact with the substrate while the molecular planes are slightly inclined by an angle ξ with respect to the mica surface normal (cf. Figure 3.20b). By that, an efficient π–π-overlap is ensured even at the lowest surface coverages, as adjacent edge-on molecules are presumably separated by $\approx 3.41\,\text{Å}$ which is the mean perpendicular distance of the two centro-symmetrically related molecules in the bulk crystal structure. Compared to the lateral width of QT
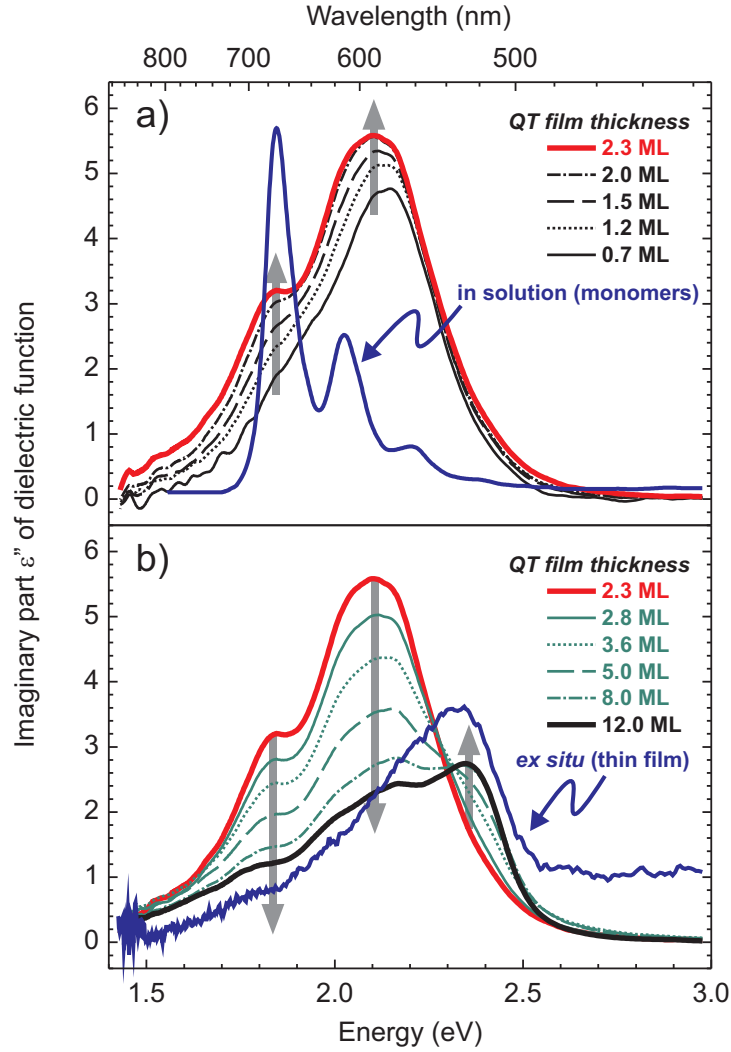
Figure 3.19: Imaginary part ε'' of the dielectric function $\hat{\varepsilon} = \varepsilon' - i\varepsilon''$ of QT deposited on mica extracted from the DRS shown in Figure 3.18. The nominal thicknesses are given here in equivalents of densely packed flat-lying monolayers, as encountered on Au(111), on graphite, or on HBC on Au(111): **a)** up to $2.3\,\mathrm{ML}$, and **b)** beyond $2.3\,\mathrm{ML}$. These spectra are compared to the absorbance recorded in solution [129] and to the *ex situ* measured absorbance of a $4\,\mathrm{ML}$ thick QT film on mica, respectively (both spectra not to scale).

of $\approx 8.2\,\text{Å}$ (cf. Figure 3.1), the shorter separation distance of edge-on molecules would mean a reduction of the required space by a factor of ≈ 2.4 with respect to densely packed face-on (i.e., flat-lying, cf. Figure 3.20a) molecules. If one further assumes an inclination angle of $\xi \approx 18°$ derived from the tilting angle between two adjacent QT dimers in the bulk crystal [46], one correspondingly obtains a factor of $2.4 \cdot \cos\xi \approx 2.3$. This value renders the observation of a critical *nominal* thickness of $\approx 2.3\,\mathrm{ML}$ (in units of flat-lying QT) plausible.

In *stage 2* (above $2.3\,\mathrm{ML}$, Figure 3.19b), the spectral features at $\approx 2.10\,\mathrm{eV}$ and $\approx 1.85\,\mathrm{eV}$ quickly diminish, while a new peak evolves at $\approx 2.35\,\mathrm{eV}$. By
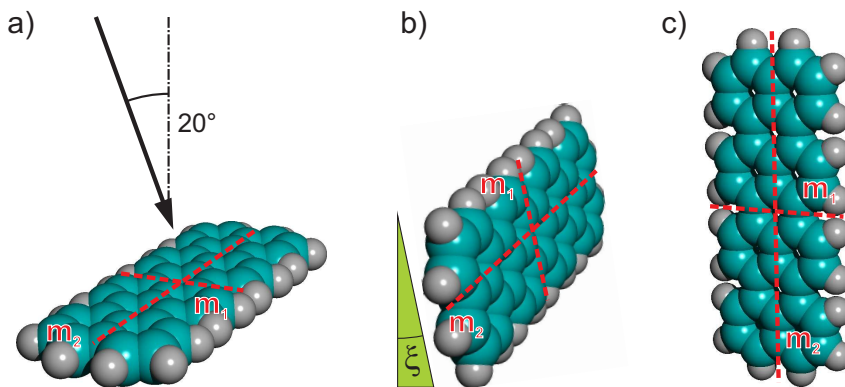
Figure 3.20: Rendering of three possible QT arrangements with respect to the substrate: **a)** face-on (flat-lying), **b)** long edge-on, and **c)** short edge-on (upstanding). The almost perpendicular $(20\,^\circ)$ incidence of light is also indicated. The molecule's mirror axes m_1 (short axis) and m_2 (long axis) are marked with red dashed lines. The molecular planes might further be inclined by an angle ξ with respect to the surface normal, visualized by the green triangle.

that, the area under the spectra substantially decreases, although it should in first approximation be almost constant, provided that the oscillator strength per molecule is constant. This apparent decrease of the observed oscillator strength of the ensemble is probably caused by the specific geometry of this QT film. Having in mind that we record the DRS under near normal incidence, we can only probe those molecular transition dipole moments that have components perpendicular to the incident light beam (transverse waves), i.e., essentially parallel to the surface. According to semi-empirical calculations [154] based on the ZINDO/S method performed for a QT derivative (with substituted end groups that increase the solubility but hardly affect the optical properties), the main $S_0 \rightarrow S_1$ transition dipole moment is oriented along the molecule's long axis, while the $S_0 \rightarrow S_2$ transition is perpendicular to the latter, i.e., along the naphthalene units of the aromatic framework. Therefore, the observed oscillator strength of the $S_0 \rightarrow S_1$ transition should decrease considerably for short edge-on (i.e., upstanding, Figure 3.20c) molecules, while it should be similar for long edge-on vs. face-on orientation (Figure 3.20a vs. b).

The *ex situ* measured absorbance spectrum of a 4 ML thick QT film on mica shown in Figure 3.19b essentially consists of a main peak at $\approx 2.32\,\mathrm{eV}$ which is by far more pronounced than the feature at $2.35\,\mathrm{eV}$ in the *in situ* ε'' spectrum of the 3.6 ML QT film. This circumstance is very likely caused by a structural reordering of the QT film after deposition as evidenced in Figure 3.18c. The tendency of the molecules to rearrange may be even more obvious when transferred to ambient conditions for the *ex situ* absorbance measurements. The exposure of the QT covered hydrophilic mica surface to atmospheric humidity seems to trigger a recrystallization into the bulk structure, as similarly demonstrated for PTCDA on mica [76].

QT on Quartz Glass. The assignment of the new high energy feature of QT on mica arising at thicknesses higher than 2.3 ML was derived from the evolution of the ε'' spectra with increasing film thickness. To further tighten our interpretation, it is advisable to repeat these measurements on quartz glass (SiO_2), as on this substrate the growth behavior of QT films is already known. Hayakawa *et al.* unambiguously showed by means of atomic force microscopy (AFM) and X-ray diffractometry (XRD) that QT thin films grow in upright orientation on SiO_2 (cf. Figure 3.20c), presumably exhibiting lattice parameters comparable to the bulk crystal [137, 138]. If our assumptions for QT deposited on mica are true, a similar high energy feature as in *stage 2* of QT on mica should also develop on quartz glass.

The measured DRS series of QT films on quartz glass is depicted in Figure 3.21. Once more, the nominal thicknesses are given here in equivalents of densely packed flat-lying monolayers, as encountered on Au(111), on graphite, or on HBC on Au(111). The DRS drops below zero at $E \gtrsim 2.7$ eV, which is probably caused by a non-negligible surface roughness of the substrate and the adsorbate as well, as also discussed in Ref. [79]. In addition, drift is a major concern in this experiment, since the optical response of the upright oriented QT molecules is indeed very small. Therefore, the signal-to-noise ratio is inferior to the experiments described above, and drift-correction is challenging.

The ε'' spectra extracted from the DRS via `fit-nk` are shown in Figure 3.22. As quartz glass is a highly transparent substrate, the ε'' spectra qualitatively match the DRS, compare Section 2.3. We do indeed observe a peak at 2.49 eV (at $d = 0.9$ ML) which shifts toward even higher energies upon
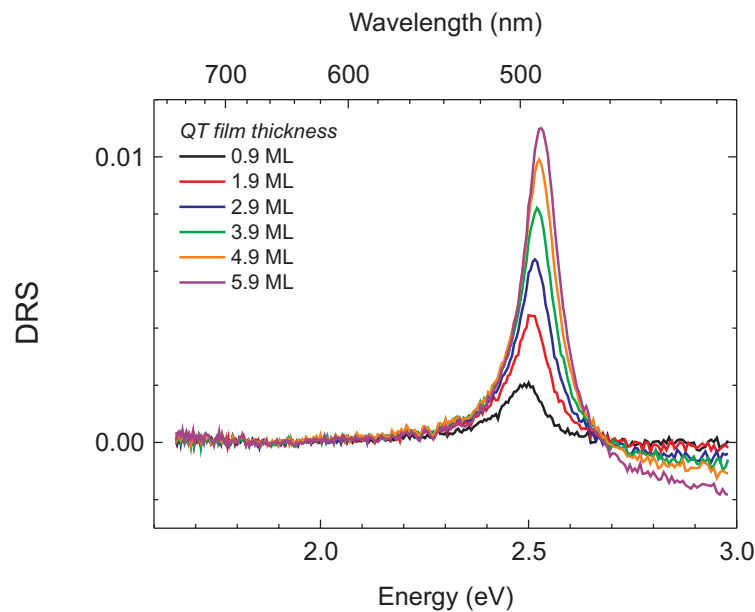

Figure 3.21: Drift-corrected differential reflectance spectra of QT deposited on quartz glass.

further deposition of QT ($2.53\,\text{eV}$ at $d = 5.9\,\text{ML}$). All the spectra are much narrower than the rather broad absorption behavior observed on mica, even for thicknesses greater than $4\,\text{ML}$. However, single molecule behavior can be ruled out due to the absence of monomer spectra with vibronic progression and the completely different transition energy. Instead, aggregates are predominant and cause this optical absorption behavior. Except for the slight shift, no significant spectral development occurs up to thicknesses of more than $8\,\text{ML}$ (not shown here), in contrast to the systems discussed above.

Very low ε'' values (and hence very small oscillator strengths) are evident from Figure 3.22, which is a direct consequence of the film anisotropy already discussed. Only those components of the molecular transition dipole moments are probed by the incident light beam that are perpendicular to the latter, i.e., essentially parallel to the substrate plane. This yields rather low measurable intensities for the main transition dipole moments oriented along the molecular long axis due to the upright orientation of the QT molecules. For these reasons, the absolute intensities of the depicted spectra certainly have an inferior experimental accuracy and can not be regarded as a reference, but should be qualitatively correct.

This high energy peak at $\approx 2.50\,\text{eV}$ might in principle have the same origin as the aggregate feature at $\approx 2.35\,\text{eV}$ developing in *stage 2* of QT on mica. The difference of $\approx 0.15\,\text{eV}$ may in part be explained by the differ-
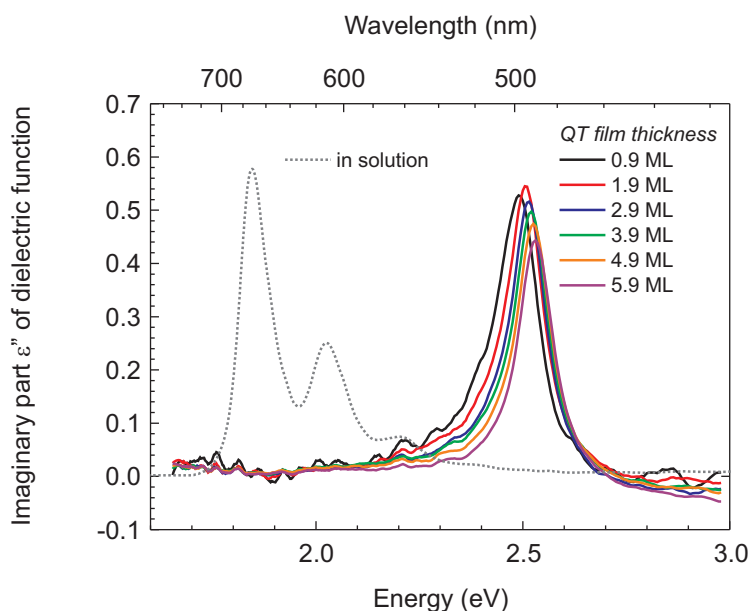

Figure 3.22: Imaginary part ε'' of the dielectric function $\hat{\varepsilon} = \varepsilon' - i\varepsilon''$ of QT deposited on quartz glass extracted from the DRS shown in Figure 3.21. The nominal thicknesses are given here in equivalents of densely packed flat-lying monolayers, as encountered on Au(111), on graphite, or on HBC on Au(111). These spectra are compared to the absorbance recorded in solution [129] (not to scale).

ent dielectric backgrounds on mica (covered by 2.3 ML of QT) and quartz glass, respectively. Furthermore, the upright orientation suggested for QT films thicker than 2.3 ML on mica might deviate from that on quartz glass, with perhaps different mutual arrangements of adjacent QT molecules, yielding different π–π-overlaps in both cases. While *stage 2* of QT on mica is most likely a polycrystalline film in the bulk structure with a typical optical splitting energy of $\Delta E \approx 0.55$ eV between the main feature and the low energy shoulder, we assume that linear chains consisting of upright oriented QT molecules *not* arranged in pairs are formed, as opposed to the assumptions made in Refs. [137, 138]. We had seen in Section 2.2.3 that even from the rather simple Kasha model one can conclude a spectral blue-shift for (almost) parallel alignment of the molecules, whereas an oblique alignment of the two molecules forming a dimer in the known bulk structure leads to a band splitting whose splitting energy depends on the respective geometry. This would readily explain the more pronounced blue-shift with an entirely suppressed low energy shoulder of QT on quartz glass.
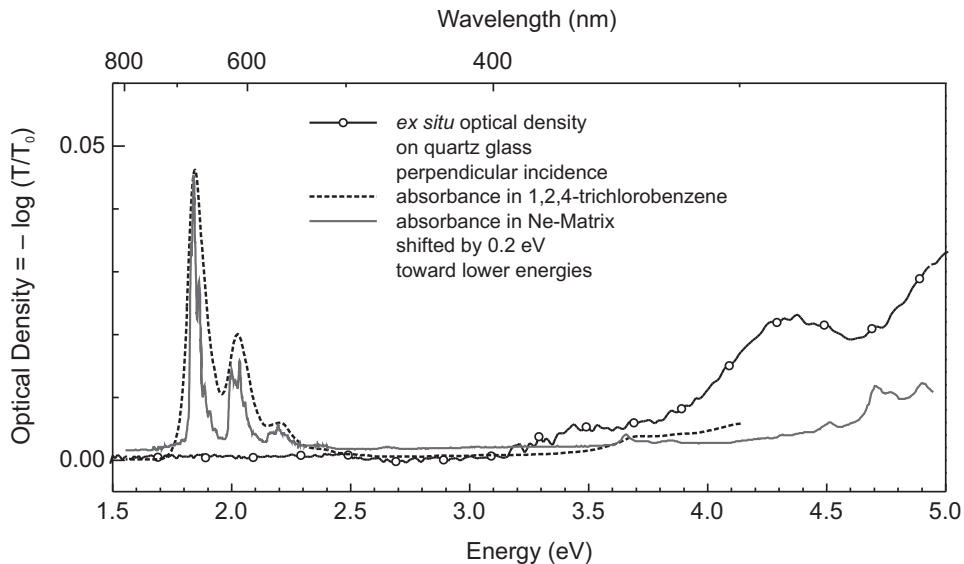

Figure 3.23: Optical density O.D. $= -\log(T/T_0)$ of a 8.5 ML (≈ 2.9 nm) thick QT film on quartz glass recorded *ex situ* at perpendicular incidence. This spectrum is compared to the absorbance recorded in 1,2,4-trichlorobenzene [129] and in a Ne-matrix at < 5 K [155] (both not to scale, the latter shifted by 0.2 eV to match the absorbance of QT in solution). At $E \gtrsim 3.5$ eV the $S_0 \rightarrow S_2$ transition sets in.

Judging from a comparison to absorbance measurements for isolated QT molecules (cf. Figure 3.23), one can state that the peak at ≈ 2.50 eV of a 8.5 ML (≈ 2.9 nm) thick QT film on quartz glass is suppressed at exactly perpendicular incidence in the *ex situ* spectrophotometer. However, several features emerge at $E \gtrsim 3.2$ eV which may be compared to the $S_0 \rightarrow S_2$ transition at higher energies. Of course, the respective spectral positions do not perfectly coincide with those of isolated molecules, as we have measured QT

aggregates here, but one can still reason that those features originate from the molecular $S_0 \rightarrow S_2$ transition. Since the latter is perpendicular to the long axis of QT [154], i.e., perpendicular to the incident light beam, this observation is an additional optical affirmation of upstanding QT molecules.

In summary, the optical behavior of QT on quartz glass suggests an upright orientation in a structure different from the bulk crystal causing a high energy peak similar to the one observed for QT films thicker than 2.3 ML on mica, but with a noticeably dissimilar band splitting behavior.

3.7   Conclusions

In conclusion, it can be stated the QT monolayers on Au(111), on graphite, and on 1 ML of HBC on Au(111) are equally composed of flat-lying molecules with almost identical unit cell dimensions. Hence, the in-plane intermolecular π–π-interaction is rather inefficient on these three substrates, as in the case of PTCDA on mica or KCl [32, 37], and can therefore not serve as an explanation for the dissimilarities in the associated optical spectra. The only option left is the coupling to the respective substrates whose intensity is drastically lower on graphite than on Au(111). By introducing a single monolayer of flat-lying HBC we even achieved an almost complete decoupling from the underlying Au(111) surface, as evidenced by the vibrationally resolved QT monomer spectra that are almost as sharp as in solution. So far, such a decoupling effect yielding monomeric behavior has only been achieved in STM-tip-induced luminescence of single molecules on *inorganic* spacer layers, i.e., on oxides (e.g., Zn(II)-etioporetioporphyrin I on a 0.5 nm thin aluminum oxide (Al_2O_3) film grown on a NiAl(110) surface [156]) or on salts (e.g., C_{60} on a NaCl film of thickness between 1 and 3 ML on Au(111) [157]). Thus we have demonstrated the first atomically thin *organic* spacer layer [133], and we anticipate our results to be a starting point for the fabrication and investigation of multiple organic quantum wells on the monolayer scale.

Insulating mica and quartz glass surfaces that naturally exhibit negligible electronic coupling capabilities cause a upstanding orientation of the QT molecules. While QT grows in two subsequent stages on mica, as deduced from the optical spectra only, its upright orientation rigorously occurs beginning at submonolayer coverage on quartz glass [137, 138]. We have seen that not only these two growth modes can be unambiguously distinguished by means of DRS, but also that the fundamental dissimilarities with the optical spectra on the conductive substrates discussed here can only be explained by entirely different film structures.

The comparison of these QT systems on various substrates serves as an instructive example for the elucidation of the structure–properties-relations of thin molecular films.

4 Optical Manifestation of Metal–Organic Charge Transfer

The second chapter containing experimental results is meant to be a consequent extension of the preceding one. We will aim for a classification of the electronic coupling of organic adsorbates to different metal substrates, which may in principle be accompanied by charge transfer (CT). For this purpose, 3,4,9,10-perylenetetracarboxylic dianhydride (PTCDA) will be in focus here, since the electronic properties of PTCDA thin films on various metal surfaces have been intensively elaborated in the recent past. In particular, Au, Ag, and Al surfaces will be used for epitaxial thin film growth monitored with differential reflectance spectroscopy (DRS). We present clear optical evidence for ionized PTCDA at several interfaces and propose the CT to be related to the electronic level alignment governed by interface dipole formation on the respective metals. Some of our findings actually disagree with previous studies to a certain extent, and we anticipate that new beneficial insight to the current understanding of CT effects in the proximity of metal surfaces can be established.

4.1 Introduction

The electronic properties of organic dyes are markedly affected by the proximity of metal surfaces, depending on the strength of the metal–organic interaction [22, 23, 25, 26]. We have demonstrated in the previous chapter that this electronic coupling is evidently reflected in the optical behavior of thin QT films, even on an inert noble metal (gold) surface. In particular, the optical absorption of the molecular contact layer appears broadened and almost structureless, while it is possible to suppress such a coupling by an organic spacer layer only one atom in height.

Here we would like to expand these studies by varying the type of metal used as substrate. For this purpose we choose Au, Ag, and Al surfaces in order to cover a broad range from inert to rather reactive metals. Furthermore, 3,4,9,10-perylenetetracarboxylic dianhydride (PTCDA, see Table 2.1) will be

in focus here, since this molecular species has received outstanding scientific attention concerning the epitaxial growth as well as the electronic spectra of thin films. For example, it is known from photoelectron spectroscopy, high-resolution electron energy-loss spectroscopy (HREEL), and density functional theory (DFT) that the molecular orbitals of highly ordered PTCDA thin films differ noticeably for various metal substrates ranging from weakly to highly interacting, including the examples named above [158–163]. We will elucidate the literature data in more detail where appropriate.

The good quantitative agreement of the PTCDA film structures observed by us on the various metal surfaces with those published [164–170] decisively enhances the comparability between different measurements. Briefly summarized, our epitaxial PTCDA films exhibit flat-lying molecules forming two closed MLs before island growth sets in (Stranski-Krastanov growth, cf. Refs. [166–168, 171]). The unit cell parameters of the plane of contact are usually very close to the (102) "herringbone" plane of the known bulk crystal structure, which itself exhibits two polymorphs, namely the α- and the β-phase [44, 172–174]. The lattice parameters of both phases are listed in Table 4.1 and are correspondingly visualized in Figure 4.1. Both polymorphs can be rationalized as stacked sheets with a small lateral displacement of adjacent (102) planes in which the molecules lie flat. Within one such sheet, the separation of nearest neighbors is comparatively large (≈ 1.2 nm) and the resulting π-orbital overlap is rather weak. However, the overlap between two face-to-face stacked molecules with an intermolecular distance of only $d_{(102)} \approx 0.32$ nm (cf. Table 4.1) is significantly higher. Consequently, the crystal can be regarded as a two-dimensional array of one-dimensional stacks. Hence, we speak of quasi-one-dimensional crystals with strong intermolecular orbital overlap, which can be favorably addressed by established exciton theories [52, 58–61].

Table 4.1: Bulk crystal structure of PTCDA: monoclinic, space group $P2_1/c$, two molecules per unit cell. Adapted from [44, 172, 173]. Standard deviations (given in parentheses) are available for the β-phase only [44].

	$a(\text{Å})$	$b(\text{Å})$	$c(\text{Å})$	$\beta(°)$	$V(\text{Å}^3)$	$d^\dagger_{(102)}(\text{Å})$
α-phase*	3.74*	11.96	17.34	98.8	766.5	3.219
β-phase	3.78(01)	19.30(03)	10.77(02)	83.6(1)	780.8	3.250

*The lattice parameters of the α-phase listed in Ref. [173] were cited in Ref. [44], however with a different value for a (3.74 Å instead of 3.72 Å in the original publications [172, 173]).
†The distance $d_{(102)} = ac \cdot \sin\beta / \sqrt{4a^2 + c^2 - 4ac \cdot \cos\beta}$ between adjacent (102) planes was calculated with the values given here and in Ref. [44]. Replacing a with the original value of 3.72 Å [172, 173] yields $d_{(102)} = 3.205$ Å for the α-phase.
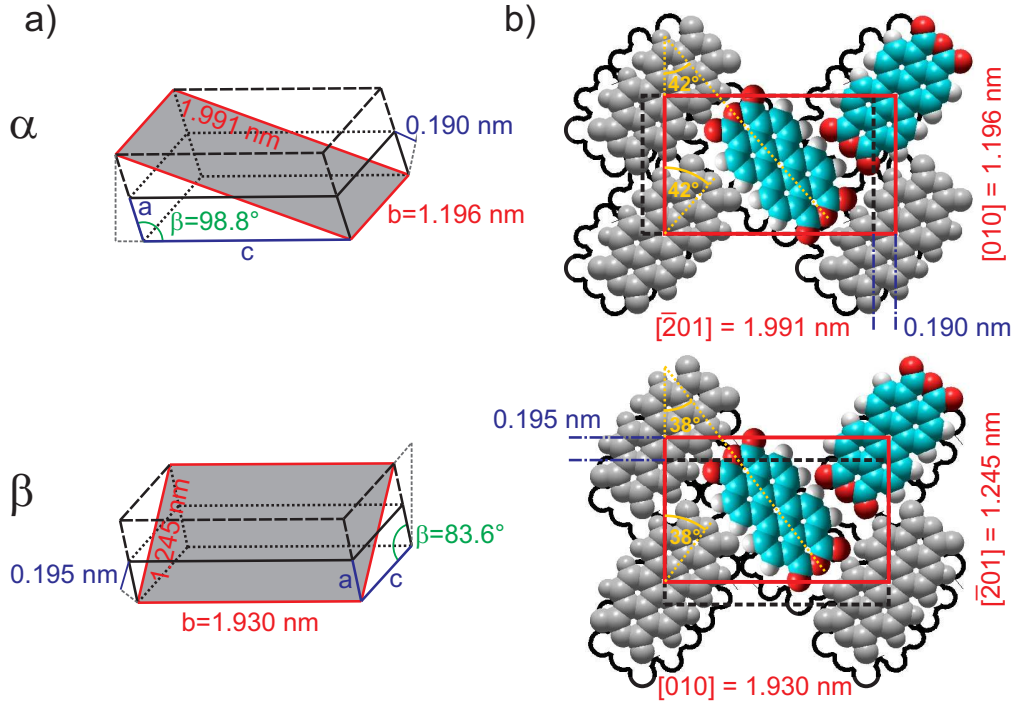
Figure 4.1: Illustration of the PTCDA bulk crystal structure, **upper panels:** α-phase, **lower panels:** β-phase. **a)** Representation of the respective three-dimensional unit cells, adapted from Ref. [174]. The (102) planes are shaded in gray. **b)** Projection onto the (102) planes. PTCDA molecules of two adjacent layers are sketched differently, and the lateral shifts between them are indicated. The rotational angle of the molecules' long axes with respect to the rectangular (102) unit cells are given. The van der Waals dimensions of PTCDA are approximately $1.42\,\text{nm} \times 0.92\,\text{nm}$ [112, 170].

Only few exceptions from these general statements are found, where either flat-lying PTCDA square phases, with no known bulk analogy, or a rod-like structure with upstanding molecules were observed [165, 166, 170, 175]. However, these exceptions are not relevant for the films investigated here.

4.2   PTCDA on Au(111) and Au(100)

This section addresses the optical spectroscopy performed on PTCDA thin films on low index surfaces of gold single crystals. In the past, analogous investigations were the subject of a similar, yet in central aspects very different publication [176]. However, the *ex situ* character of the technique used at that time did not allow for an unambiguous identification of interface formation processes, such as coupling versus decoupling, or metal–organic charge transfer, on the basis of the spectra obtained then. It was also shown in the meantime that especially PTCDA films may be subject to pronounced structural reordering when transferred from UHV to ambient conditions, with a strong impact on the optical behavior [76]. Thus, UHV and cleanliness are

crucial prerequisites for such experiments. Further, the evaluation of comparable optical data of PTCDA on Au(111) previously given in the PhD thesis of Robert Nitsche [79] differs from the present work. We propose an alternative interpretation of the optical spectra as discussed hereafter and in Ref. [177].

Differential Reflectance Spectra. The differential reflectance spectra as a function of PTCDA film thickness on Au(111) are shown in Figure 4.2. Motivated by the abruptly emerging sharp features in the DRS for $d > 1\,\mathrm{ML}$, we expand the two components (metal / n MLs PTCDA) to a hypothetical three-phase system (metal / 1st ML PTCDA / $(n-1)$ MLs PTCDA) by setting a new baseline after completion of the 1st ML of PTCDA (dashed line in Figure 4.2):

$$\mathrm{DRS}^*(E, d^*) := \frac{R(E, d^*) - R(E, d_0)}{R(E, d_0)} \ , \tag{4.1}$$

where $d^* = d - d_0$ means the *reduced* nominal film thickness, and $R(E, d_0)$ is the reflectance of the metal covered with $d_0 := 1\,\mathrm{ML}$ of PTCDA. We would like to emphasize that we do not introduce any sort of model here, as Equation (4.1) is in fact an approximation based on the observation that the optical response of the first ML appears to be separated from further layers grown on top, as demonstrated in the following. This situation is schematically depicted in Figure 4.3. It is already visible in Figure 4.2 that the DRS signal of up to $d \approx 1\,\mathrm{ML}$ is broad and essentially featureless. Distinct peaks suddenly appear upon growing the 2nd ML of PTCDA, as also evidenced in the DRS* (cf. Figure 4.4).
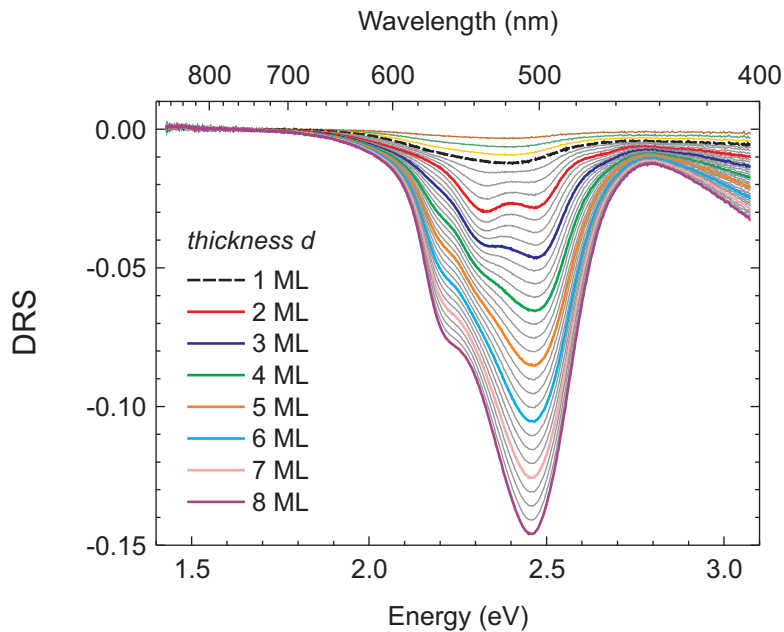

Figure 4.2: Drift-corrected differential reflectance spectra (DRS, Equation (2.12)) of PTCDA deposited on Au(111). The *total* nominal film thicknesses d are given.
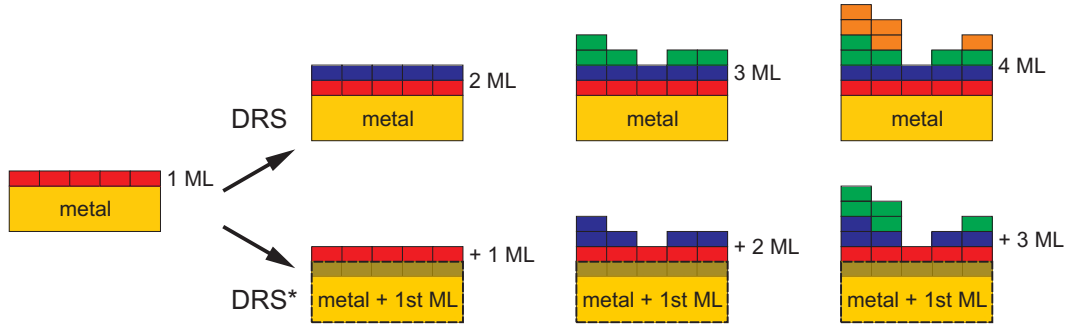
Figure 4.3: Scheme of the Stranski-Krastanov growth of PTCDA on metal surfaces. Intuitively, the interaction between face-to-face stacked PTCDA molecules would dictate the optical response as drawn in the upper panels. In contrast, the strong electronic coupling to the metal substrate leads to an optical behavior comparable to a hypothetical three-phase system as visualized in the lower panels. Thus, for our analysis we treat the 1st ML as part of a new substrate being consequently characterized by $R(E, d_0 = 1\,\text{ML})$. This evaluation in terms of DRS* (cf. Equation (4.1)) differs from Ref. [79].
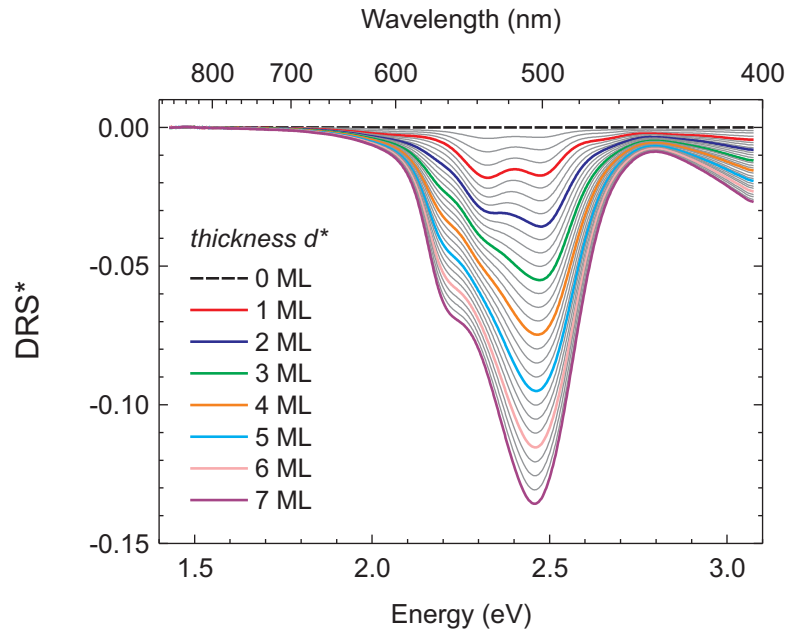

Figure 4.4: Drift-corrected differential reflectance spectra (DRS*, Equation (4.1)) of PTCDA deposited on Au(111). The *reduced* nominal film thicknesses $d^* = d - 1\,\text{ML}$ are given, in contrast to Figure 4.2. We thereby assume a hypothetical three-phase system (metal / 1st ML PTCDA / $(n-1)\,$MLs PTCDA).

This procedure is not obvious at first glance as it implies that formerly identical molecules are now to be treated separately in the 1st and 2nd MLs. Moreover, it is not suitable for all molecule–substrate combinations, since a clear electronic decoupling is a prerequisite for the separate treatment. For instance, monomer spectra exhibiting a vibronic progression are *not* observed if the 1.93 ML thick QT film on Au(111) is considered as 0.93 ML of QT de-

posited on a closed QT monolayer on Au(111) (dash-dotted curve in Figure 3.4 on page 51). Instead, this spectrum rather bears the broader dimeric character known from the 1.93 ML QT spectrum on the HBC spacer layer (thick blue curve in Figure 3.11 on page 62). In addition, the pronounced interaction between adjacent QT layers seemed to be associated to almost coinciding optical transition energies of QT monomers and the hybridized contact layer of QT on Au(111). However, as this coincidence can also be stated for the PTCDA layers on Au(111) here, we conclude that dissimilar optical transition energies of the 1st and 2nd molecular layers are *not* a necessary condition for the occurrence of electronic decoupling between them. Hence, caution is advised when applying this three-phase approach.

Dielectric Function Extracted from DRS. The according ε'' (and ε') spectra extracted from the original DRS and from the reduced DRS, i.e., DRS*, are depicted in Figure 4.5. The broad character of the 1st ML of PTCDA in the DRS directly translates to broad ε'' spectra centered at 2.26 eV. As a matter of fact, the submonolayer spectra ($d < 1$ ML) exhibit virtually no deviation from the $d \approx 1$ ML spectrum and therefore only a selection is shown in Figure 4.5. Because of the large intermolecular distance between nearest neighbors the in-plane dimerization should be negligible, as recently demonstrated for insulating substrates [32, 37]. However, the spectrum of the 1st ML of PTCDA on Au(111) does *not* exhibit the monomeric shape known on inert (i.e., non-metallic) surfaces, most evidently on mica and KCl [32, 37]. This behavior must be due to a comparatively strong coupling of molecular orbitals to electronic states extending perpendicularly from the metal surface. Consequently, significant broadening of the adsorbate levels, as described, e.g., by the Anderson–Newns model [143, 144], is observed which may be additionally accompanied by charge transfer. This effect is also called metal–organic "hybridization" in the literature [178, 179] and has been examined for the molecular energy levels by means of photoelectron spectroscopy and electron energy loss spectroscopy measurements [145, 161]. The impact of this phenomenon on the optical transitions of molecular adsorbates on metal surfaces as reported here has been described before in Section 3.2 and in Ref. [133].

For PTCDA thicknesses of $d > 1$ ML (i.e., $d^* > 0$ ML), several peaks emerge, as depicted in the upper part of Figure 4.5b, and show almost no variation until completion of the 2nd ML (i.e., $d^* = 1$ ML; intermediate coverages omitted in Figure 4.5 for clarity). Clearly, this spectrum of $d^* = 1$ ML can be divided into two different parts which will now be discussed separately.

In the range $E \gtrsim 2.2$ eV, the spectral shape can be assigned to neutral monomers since the main feature at 2.32 eV with its vibronic progression of $\Delta E_{\mathrm{vibron}} \approx 0.17$ eV corresponds to the spectra recorded in solution (cf. Figure 2.3) and on insulating surfaces [32, 37]. This means in turn that there can
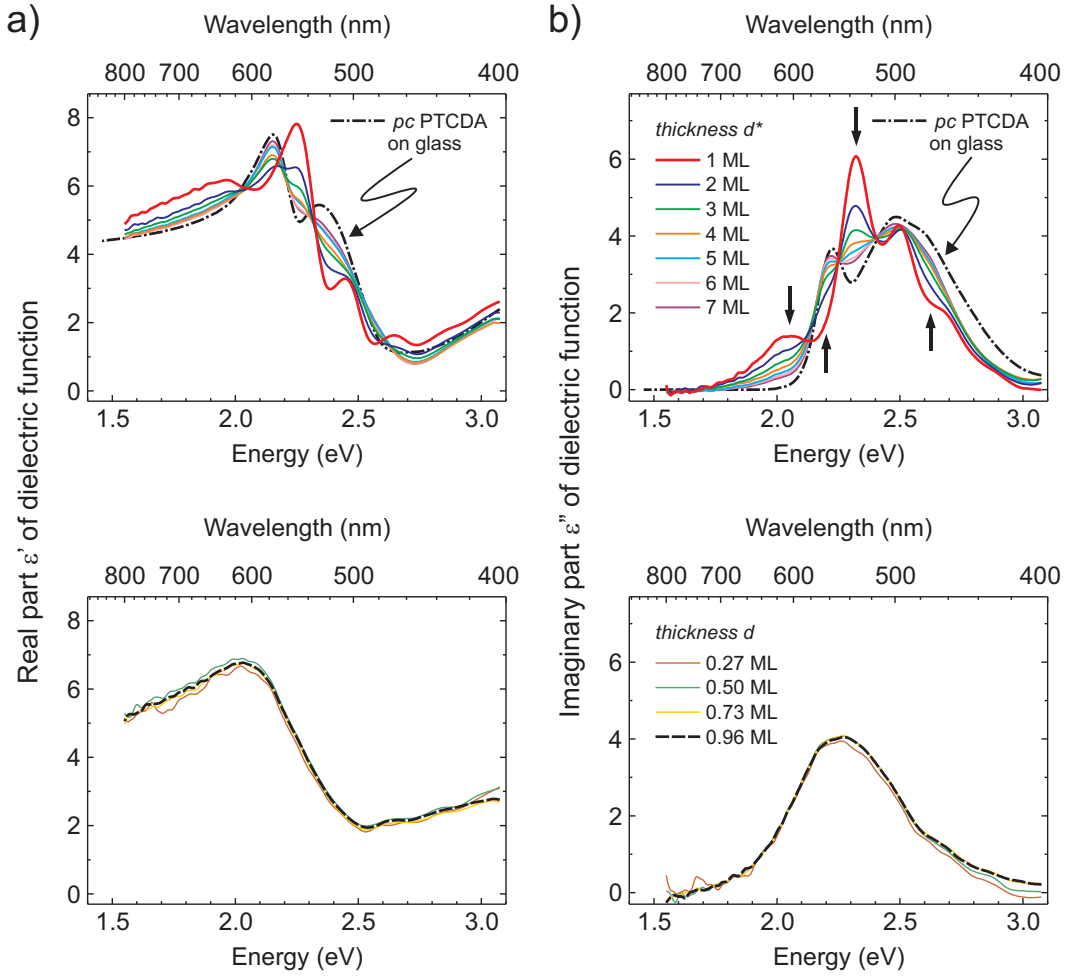
Figure 4.5: **a)** Real part ε', and **b)** imaginary part ε'' of the dielectric function $\hat{\varepsilon} = \varepsilon' - i\varepsilon''$ of PTCDA deposited on Au(111). For thicknesses up to $d = 1\,\mathrm{ML}$ (lower panels) $\hat{\varepsilon}$ was extracted from the original DRS shown in Figure 4.2. There is virtually no deviation in the respective spectral series for both ε' and ε''. For thicknesses of $d > 1\,\mathrm{ML}$ (i.e., $d^* > 0\,\mathrm{ML}$, upper panels) $\hat{\varepsilon}$ was extracted from the reduced DRS, i.e., DRS*, shown in Figure 4.4, see text for explanations. For clarity, only selected spectra are presented. Arrows indicate the spectral development with increasing film thickness. The independently determined $\hat{\varepsilon}$ spectrum of a comparatively thick polycrystalline (*pc*) PTCDA film on glass is shown in comparison (adapted from Ref. [65]).

only be marginal coupling between the 2$^{\mathrm{nd}}$ and the 1$^{\mathrm{st}}$ ML of PTCDA providing further legitimation for the above three-phase approach. This is somehow surprising as one would intuitively expect physical dimerization between face-to-face stacked identical aromatic molecules. However, for $E \gtrsim 2.2\,\mathrm{eV}$ the 2$^{\mathrm{nd}}$ ML of PTCDA remarkably behaves optically like an ensemble of monomers, or, in other words, like the 1$^{\mathrm{st}}$ ML on an *insulating* substrate. This fact reminds us of the results for quaterrylene grown heteroepitaxially on an atomically thin hexa-*peri*-hexabenzocoronene monolayer (cf. Sections 3.4 and 3.5): We conclude that the energy levels of the 1$^{\mathrm{st}}$ ML of PTCDA on Au must

also differ considerably from the levels of decoupled PTCDA in the subsequent layers, thereby inhibiting noticeable coupling.

It is intriguing to note that in the range $E \lesssim 2.2\,\text{eV}$ a new peak at $2.05\,\text{eV}$ (or $2.03\,\text{eV}$, respectively, for an identical PTCDA thickness on Au(100)) has emerged which does not belong to the absorbance of neutral PTCDA monomers. Considering the ε'' spectra of comparatively thick PTCDA films on glass [65] it is obvious that this feature can also not be explained by aggregation effects. Hence, it must be of different nature, and we attribute this peak to PTCDA radical cations (PTCDA$^{\bullet+}$). For a univocal identification of this feature, it would be advisable to compare our ε'' values to absorbance spectra of charged PTCDA in solution. However, to our knowledge complete datasets are not available which is probably due to PTCDA's rather poor solubility. Still, several publications contain optical absorption spectra of soluble neutral and charged PTCDA derivatives, namely DBPI and PBI (cf. Table 2.1) with a high degree of optical equivalence of the according perylene derived chromophores [30, 31]. Although ionized with dissimilar methods, the energy difference ΔE of the cationic main peaks with respect to the associated neutral molecules amounts to $0.29\,\text{eV}$ and $0.28\,\text{eV}$, respectively (cf. Figure 4.15 and Table 4.2). Here, we compare relative peak positions rather than absolute values due to the presence of different solvent shifts and dielectric backgrounds in the respective experiments. The positions of the new PTCDA peaks observed here lowered by $\Delta E \approx 0.27\,\text{eV}$ and $0.29\,\text{eV}$ compared to the main monomeric features on Au(111) and Au(100), respectively, nicely agree with the above values. In contrast, the spectral signatures of the anionic PTCDA derivatives exhibit a multitude of pronounced features shifted by more than $0.5\,\text{eV}$ toward lower energies compared to the absorption peaks of the corresponding neutral species [30, 31]. Hence, we can exclude the presence of anionic PTCDA in the 2$^{\text{nd}}$ ML on Au(111) and Au(100).

For further increasing film thickness, a characteristic development of the ε'' spectra sets in (Figure 4.5 upper part, $d^* > 1\,\text{ML}$). The monomeric features begin to disappear, and the spectral shape broadens forming a new shoulder at $\approx 2.2\,\text{eV}$. The peak at $2.05\,\text{eV}$ (or $2.03\,\text{eV}$, respectively) assigned to cationic PTCDA vanishes suggesting that the 3$^{\text{rd}}$ ML and further layers bear no or just very few charges, and, accordingly, this feature diminishes with rising film thickness as the fraction of neutral PTCDA steadily increases. The development is accompanied by distinct intersections of all spectra in three isosbestic points at $\approx 2.12\,\text{eV}$, $2.25\,\text{eV}$, and $2.40\,\text{eV}$. Isosbestic points are an expression of aggregation to higher quasi-one-dimensional PTCDA stacks, i.e., the physical monomer–oligomer transition [32, 63], cf. Section 2.2.3. Here, we would like to place emphasis on an independently measured ε'' spectrum of a rather thick polycrystalline (*pc*) PTCDA film on a glass substrate [65] which also coincides very nicely with these intersections. Further, the fast convergence

of our ε'' (and ε') spectra toward the *pc* bulk behavior is remarkable as it indicates that the adsorbate dielectric function becomes substrate-independent at quite low film thicknesses. The persistence of the monomeric feature at 2.32 eV for several nominal MLs confirms the Stranski-Krastanov growth with clusters forming on top of a closed 2 ML thick film.

All of the above key statements about the optical spectra and their film thickness-dependent development made primarily for PTCDA on Au(111) are equally valid on Au(100) as substrate, except for some very slight deviations within the experimental accuracy on the energy scale. Consequently, we can rule out that our observations would be a mere effect of film structure which exhibits a number of different phases and orientations due to the distinct substrate symmetries and surface reconstructions [165]. Likewise, the known Au(111) surface state can not be responsible for the observed phenomenon either. The dissimilarities between PTCDA films on Au(111) and Au(100) actually play only a minor role in the respective optical response. Hence, we will not explicitly discuss the results obtained for PTCDA on Au(100) in detail here. Instead, they will be briefly presented in the Appendix.

4.3   PTCDA on Ag(111)

Following the above findings, one is apt to replace the gold substrate with a different metal, such as silver, possessing an appreciably smaller workfunction $\Phi_{Ag} < \Phi_{Au}$ and hence causing a significantly different level alignment. We have chosen Ag(111) since its interface with PTCDA is very well characterized by photoelectron spectroscopy and related methods [160, 161]. For instance, an almost vanishing interface dipole Δ was reported for PTCDA on Ag(111), in contrast to Au(111) substrates [160, 161]. Yet, the detailed picture of the electronics at this interface is much more complicated and will be explained in Section 4.6.

Differential Reflectance Spectra.   The thickness-dependent DRS of PTCDA on Ag(111) is depicted in Figure 4.6. Up to $d \approx 1$ ML the spectra are rather broad and hardly possess any clear features, as also observed on Au(111) in Section 4.2. At thicknesses of $d \gtrsim 1$ ML several peaks abruptly emerge (not shown in Figure 4.6) which immediately remind us of the monomer features discussed previously. We therefore apply the same analysis method in terms of the reduced DRS, i.e., DRS* (Equation (4.1)) as introduced earlier. The corresponding DRS* series is plotted in Figure 4.7.

Dielectric Function Extracted from DRS.   In accordance with Section 4.2 we extract the dielectric function ε'' (and simultaneously ε') from the DRS for thicknesses of $d \lesssim 1$ ML, while the DRS* is used for thicknesses of $d > 1$ ML,
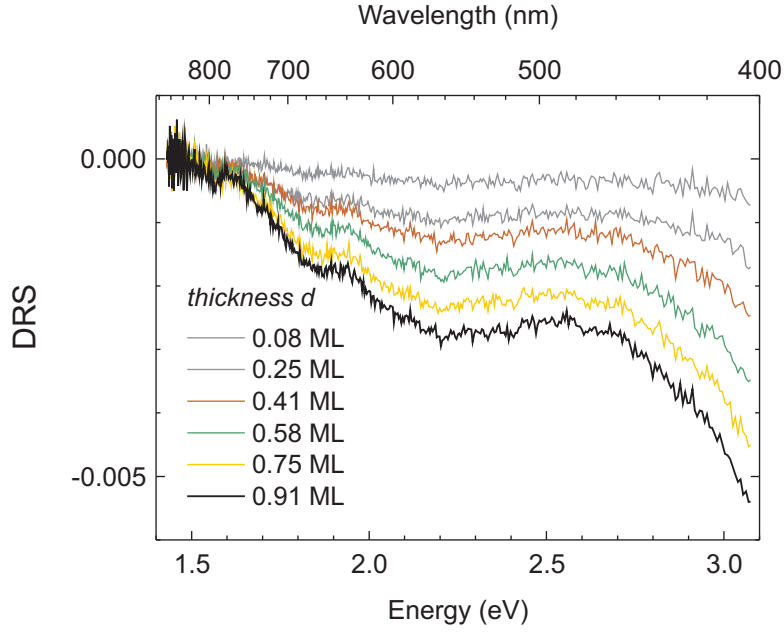
Figure 4.6: Drift-corrected differential reflectance spectra (DRS, Equation (2.12)) of PTCDA deposited on Ag(111). The *total* nominal film thicknesses $d \lesssim 1\,\mathrm{ML}$ are given.
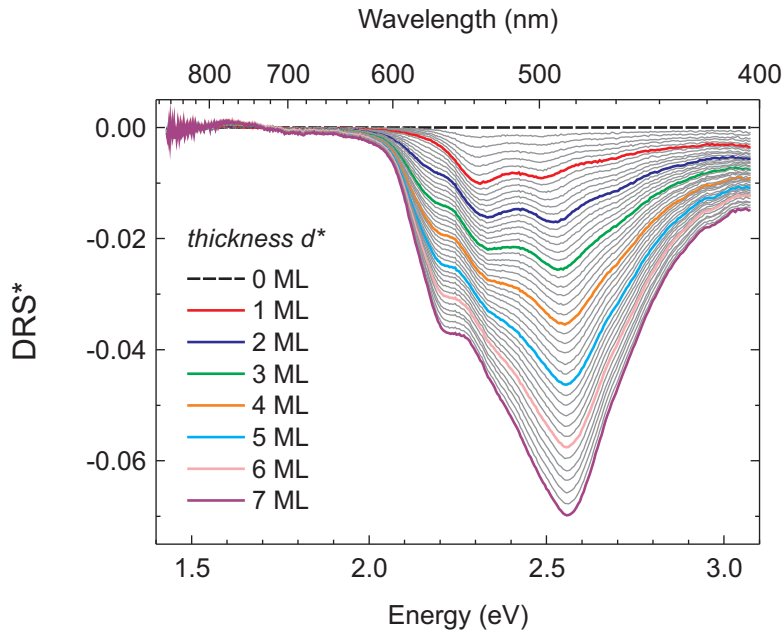

Figure 4.7: Drift-corrected differential reflectance spectra (DRS*, Equation (4.1)) of PTCDA deposited on Ag(111). The *reduced* nominal film thicknesses $d^* = d - 1\,\mathrm{ML}$ are given, in contrast to Figure 4.6. We thereby assume a hypothetical three-phase system (metal / 1st ML PTCDA / $(n-1)\,\mathrm{MLs}$ PTCDA).

i.e., $d^* > 0\,\mathrm{ML}$ (cf. Figure 4.8). Again, we would like to discuss these thickness ranges separately in the following.
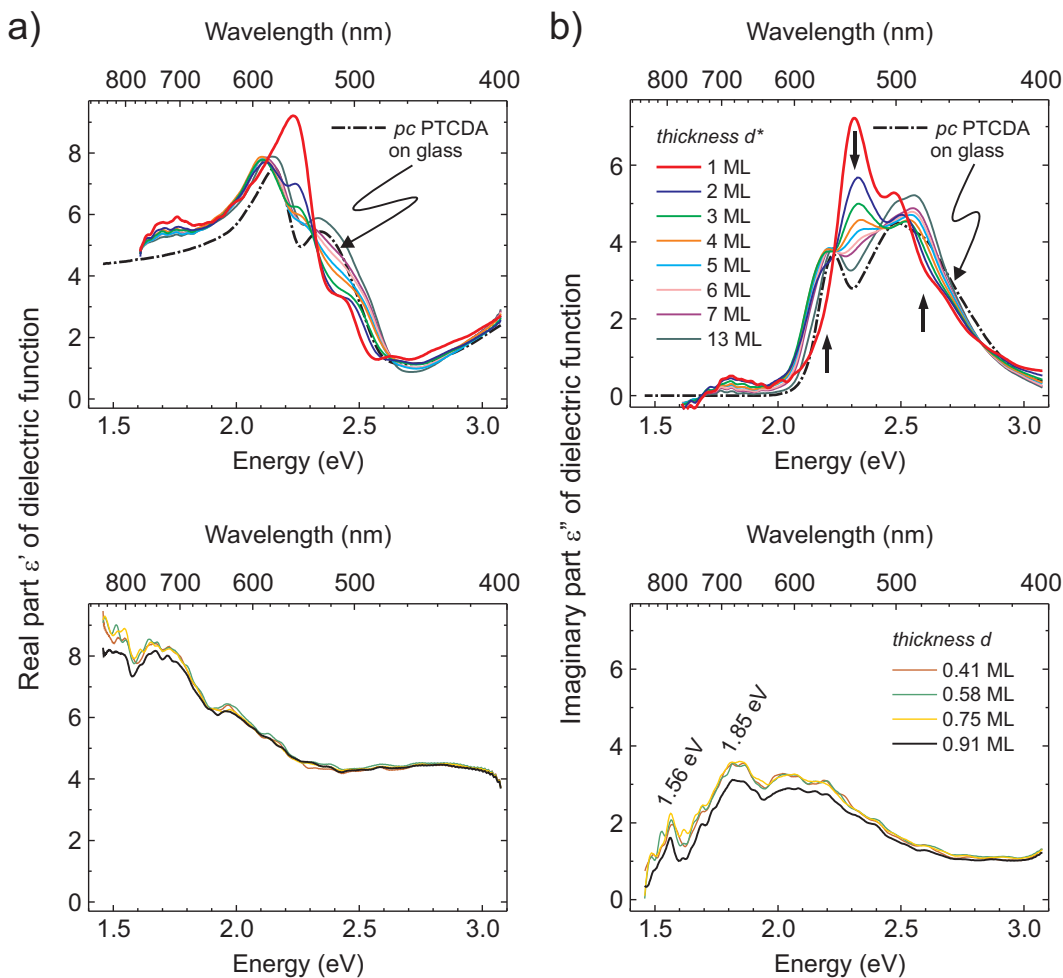
Up to monolayer coverage, i.e., for $d \lesssim 1\,\mathrm{ML}$, the ε'' spectra are very broad

Figure 4.8: **a)** Real part ε', and **b)** imaginary part ε'' of the dielectric function $\hat{\varepsilon} = \varepsilon' - i\varepsilon''$ of PTCDA deposited on Ag(111). For thicknesses up to $d = 1\,\mathrm{ML}$ (lower panels) $\hat{\varepsilon}$ was extracted from the original DRS shown in Figure 4.6. There is almost no deviation in the respective spectral series for both ε' and ε''. For thicknesses of $d > 1\,\mathrm{ML}$ (i.e., $d^* > 0\,\mathrm{ML}$, upper panels) $\hat{\varepsilon}$ was extracted from the reduced DRS, i.e., DRS*, shown in Figure 4.7, see text for explanations. For clarity, only selected spectra are presented. Arrows indicate the spectral development with increasing film thickness. The independently determined $\hat{\varepsilon}$ spectrum of a comparatively thick polycrystalline (*pc*) PTCDA film on glass is shown in comparison (adapted from Ref. [65]).

and bear no resemblance with the monomeric absorption spectra of dissolved PTDCA. As also observed on Au(111), the submonolayer spectra show only very little variation. No vibronic substructure is apparent, however, two small features at $\approx 1.56\,\mathrm{eV}$ and $\approx 1.85\,\mathrm{eV}$ may be noticed in Figure 4.8b (bottom part). Since the overall spectral quality is more noisy than on Au(111), these features should not be overestimated here. Yet, they occur in all the spectra of up to $d \approx 1\,\mathrm{ML}$ at roughly identical spectral positions and are therefore not believed to be artifacts. Remarkably, these transition energies are in excellent agreement with the peaks of negatively charged PTCDA derivatives, namely

DBPI and PBI [30, 31] (cf. Figure 4.15). They might thus stem from PTCDA radical anions (PTCDA$^{\bullet-}$) coexistent with hybridized neutral molecules.

For PTCDA thicknesses of $d > 1\,\mathrm{ML}$ (i.e., $d^* > 0\,\mathrm{ML}$), the spectral shape changes drastically (cf. Figure 4.8, upper part). Comparable to the behavior on Au(111) discussed above, distinct peaks emerge up to $d^* = 1\,\mathrm{ML}$ at $2.31\,\mathrm{eV}$, $2.47\,\mathrm{eV}$, and $\approx 2.64\,\mathrm{eV}$, resembling the monomeric absorption spectra recorded in solution (cf. Figure 2.3) and on insulating surfaces [32, 37] with a vibronic progression of $\Delta E_{\mathrm{vibron}} \approx 0.17\,\mathrm{eV}$. This spectral fingerprint similar to that of an isolated molecule indicates rather weak coupling to the underlying substrate and likewise only negligible in-plane interactions with surrounding molecules. Although we had observed such a decoupling effect for the 2$^{\mathrm{nd}}$ ML of PTCDA on Au(111) in Section 4.2, the similarity of the behavior on Ag(111) is nonetheless remarkable, because an entirely different electronic alignment and even the formation of a covalently bound 1$^{\mathrm{st}}$ ML with distorted PTCDA molecules had been reported for the latter surface [161]. Yet, beginning at $d \approx 1\,\mathrm{ML}$, the ε'' (and ε') spectra of PTCDA on Au(111) and Ag(111) look alike except for the lower photon energies. In fact, for $E \lesssim 2.2\,\mathrm{eV}$ no clear peak can be identified at $\approx 2.05\,\mathrm{eV}$ here, and thus PTCDA$^{\bullet+}$ can be ruled out in the 2$^{\mathrm{nd}}$ ML (and further layers) of PTCDA on Ag(111). Judging from the small features in the region of $\approx 1.85\,\mathrm{eV}$ one might rather be inclined to conclude the presence of (a small fraction of) PTCDA$^{\bullet-}$ in the ε'' spectra of the 2$^{\mathrm{nd}}$ ML (i.e., $d^* = 1\,\mathrm{ML}$). Admittedly, these features vanish with increasing film thickness, which would be characteristic for a peak related to charged molecules that are located in the 2$^{\mathrm{nd}}$ ML. However, the experimental accuracy achieved here does not permit to establish unquestionable evidence.

Further deposition of PTCDA beyond $d^* = 1\,\mathrm{ML}$ leads to intermolecular dimerization and to the creation of higher quasi-one-dimensional molecular stacks, as manifested in the spectral broadening and the convergence toward the independently measured $\hat{\varepsilon}$ spectrum of a comparatively thick polycrystalline (*pc*) PTCDA film on glass, shown in Figure 4.8 (upper part) for comparison. Substrate-independence is only reached at rather high nominal thicknesses of $d^* \gtrsim 10\,\mathrm{ML}$ with a different peak height ratio of the double feature at $2.48\,\mathrm{eV}$ and $2.56\,\mathrm{eV}$ compared to the final spectra on Au(111) (cf. Figure 4.5). This might probably be caused by slight deviations in the thin film structures on these two substrates which might be closer to either the α- or the β-phase that are also known to be spectrally different [64].

4.4   PTCDA on Al(111) and Polycrystalline Al

We have seen in Sections 4.2 and 4.3 that although the PTCDA film structures are comparable, the optical spectra differ appreciably between Au and Ag surfaces. It seems that the lower workfunction of silver compared to that

of gold $(\Phi_{Ag} < \Phi_{Au})$ has an impact on the intensity and probably even on the direction of the proposed charge transfer. Hence, we will include another metal surface in this survey in order to clarify to what extent we can generalize our observations. We have chosen aluminum which possesses an even lower workfunction than silver $(\Phi_{Al} < \Phi_{Ag})$.

This choice also constitutes some unavoidable inconveniences. First, freshly prepared, clean Al surfaces are highly reactive and tend to oxidize very rapidly even in UHV. Christian Golnik has demonstrated by means of Auger electron spectroscopy (AES) in his diploma thesis [180] that Al(111) surfaces clearly re-oxidize under our experimental conditions within 10 to 30 min after thorough sputter cleaning and annealing. It took only a total of 60 min to re-establish the completely oxidized character known from untreated Al surfaces. Second, the Ar^+ sputtering itself is much less efficient than for Au or Ag, rendering the preparation procedure much more challenging, while the surface quality is often inferior to the latter two metals. As a result, comparatively high surface roughnesses of Al(111) single crystals can be concluded from the relatively high noise level in LEED images [180]. Third, the bulk dielectric function and hence the spectral coefficients A and B (compare Figure 2.9) of Al imply the distinct disadvantages that $|A|$ is about 4 times smaller than on Ag and 10 times smaller than on Au, while $|B|$ is non-negligible compared to $|A|$ even at low energies. For this reason, the approximation made in Equation (2.54) is not valid here, and we have to face the consequences illustrated in Figure 4.9. There, we computed the hypothetical DRS of a 1 nm thick PTCDA film on Au, Ag, and Al by means of the commercially available thin film optics software `Film Wizard`™ (Scientific Computing International), using the dielectric function of polycrystalline (*pc*) PTCDA [65]. As a consequence of the rather low *A*-coefficient of Al, the maximum signal intensities scale as $I_{Al}^{max} : I_{Ag}^{max} : I_{Au}^{max} \approx$ 1.0 : 3.8 : 9.2 (cf. Figure 4.9a), meaning a signal-to-noise ratio of almost an
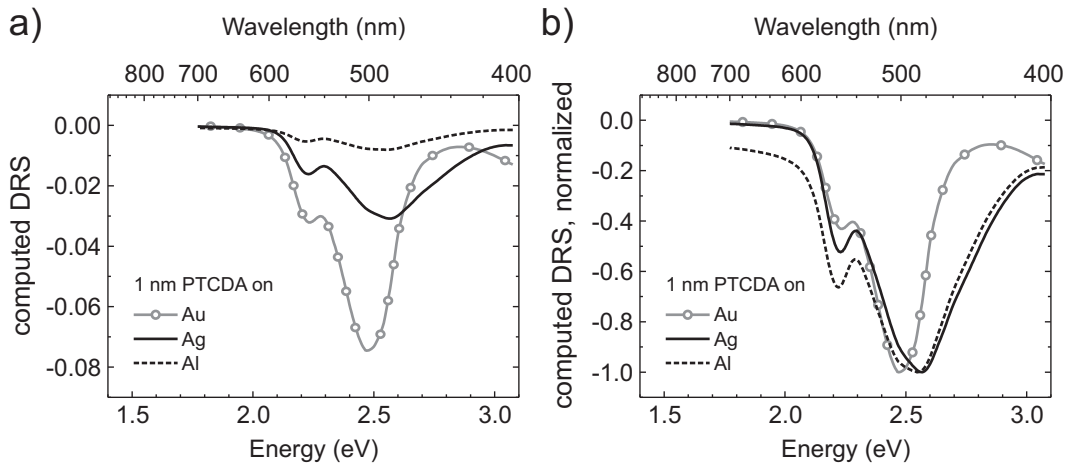

Figure 4.9: Hypothetical DRS computed by means of `Film Wizard`™. **a)** 1 nm of *pc* PTCDA on Au, Ag, and Al (absolute scale). **b)** Same as (a), but normalized to −1.

order of magnitude lower on Al than on Au. In addition, the DRS of PTCDA on Al does not converge to zero at low photon energies as opposed to Ag and Au substrates (cf. Figure 4.9b), rendering a first order drift-correction outlined in Section 2.3.3 rather tricky, if not impossible. All these facts for PTCDA films on Al surfaces considered, we expect to reach the limits of what is currently measurable with our setup.

LEED images of PTCDA films of various thicknesses on Al(111) did not exhibit any evaluable contrast. Even post-growth annealing of the PTCDA films up to $150\,°C$ did not yield any recognizable LEED spots [180]. Highly ordered growth, being the predominant situation on a broad range of other substrates, can thus not be substantiated here. Nevertheless, for the analysis of our data we assume a thin film structure comparable to the ones on Au(111) and Ag(111), i.e., flat-lying densely packed molecules growing in Stranski-Krastanov mode.

Differential Reflectance Spectra.   Figure 4.10 displays the DRS according to Equation (2.12) of up to $d \approx 1\,\mathrm{ML}$ thick PTCDA films grown on Al(111). As mentioned above, the drift-correction turned out to be challenging, since some discontinuities, i.e., 'jumps' of entire spectra sporadically occur that can not be adequately removed (see low energy side of Figure 4.10). In analogy to our previous observations, clear peaks abruptly evolve at $d \gtrsim 1\,\mathrm{ML}$, which is why we also treat this spectral series as a hypothetical three-phase system. The corresponding DRS* is depicted in Figure 4.11 according to Equation (4.1).
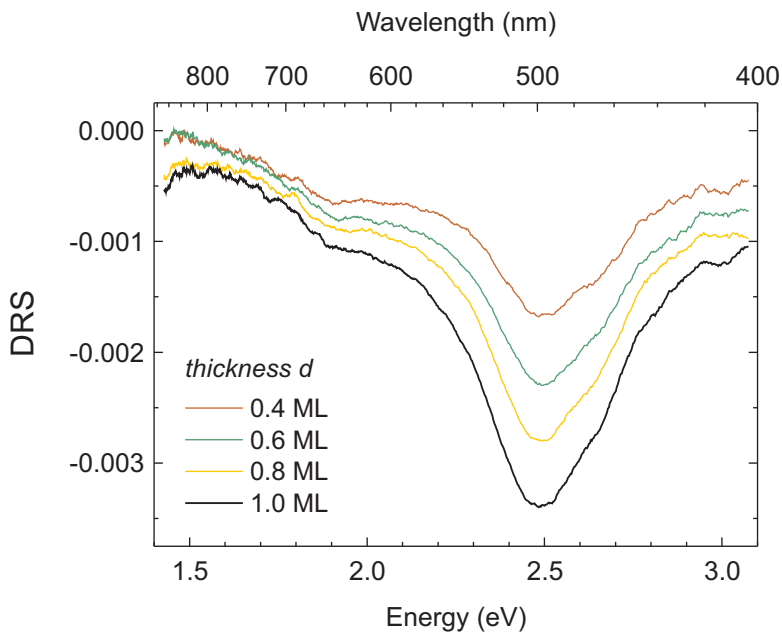

Figure 4.10: Drift-corrected, smoothed differential reflectance spectra (DRS, Equation (2.12)) of PTCDA deposited on Al(111). The *total* nominal film thicknesses $d \lesssim 1\,\mathrm{ML}$ are given.
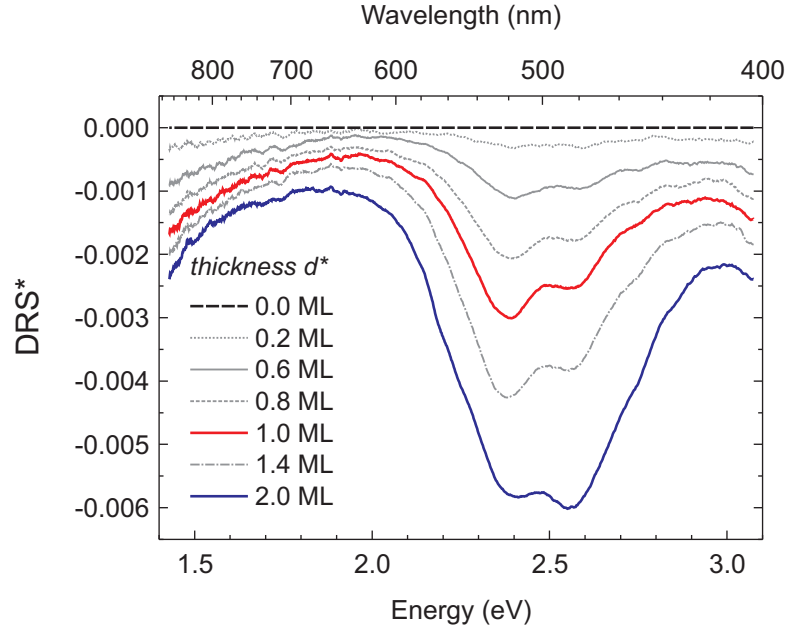
Figure 4.11: Drift-corrected, smoothed differential reflectance spectra (DRS*, Equation (4.1)) of PTCDA deposited on Al(111). The *reduced* nominal film thicknesses $d^* = d - 1\,\mathrm{ML}$ are given, in contrast to Figure 4.10. We thereby assume a hypothetical three-phase system (metal / 1st ML PTCDA / $(n-1)$ MLs PTCDA).

Also in this graph a low energy component of the spectra is visible which is presumed to be drift-related as it hardly appeared in similar experiments with different total duration.

Dielectric Function Extracted from DRS.   Due to the experimental uncertainties discussed, especially at both ends of the spectral range, the extraction of the dielectric function is somewhat approximate. Here, we also want to elaborate the spectral development before and after completion of the 1st ML of PTCDA separately, focusing on the imaginary part of the dielectric function depicted in Figure 4.12.

The ε'' spectrum for $d \approx 1\,\mathrm{ML}$ of PTCDA on Al(111) is comparatively broad (Figure 4.12, lower part). A main peak at roughly $2.47\,\mathrm{eV}$ and a smaller feature at $\approx 1.90\,\mathrm{eV}$ determine the overall picture. Both are broadened compared to the known monomeric absorbance of PTCDA and probably accompanied by smaller subfeatures. This ε'' spectrum is narrower than those on Au and Ag substrates, speaking for a slightly weaker metal–organic coupling in this case. In the view of the AES results discussed above, it seems likely that a fraction of the Al(111) surface has re-oxidized before initiation of and during the film growth, which happens on timescales of 10 to 20 min. PTCDA molecules on top of a thin aluminum oxide film would not be in direct contact with the Al(111) surface and thus exhibit a weaker electronic coupling to the latter. This might cause a contribution of neutral monomers to the signal at
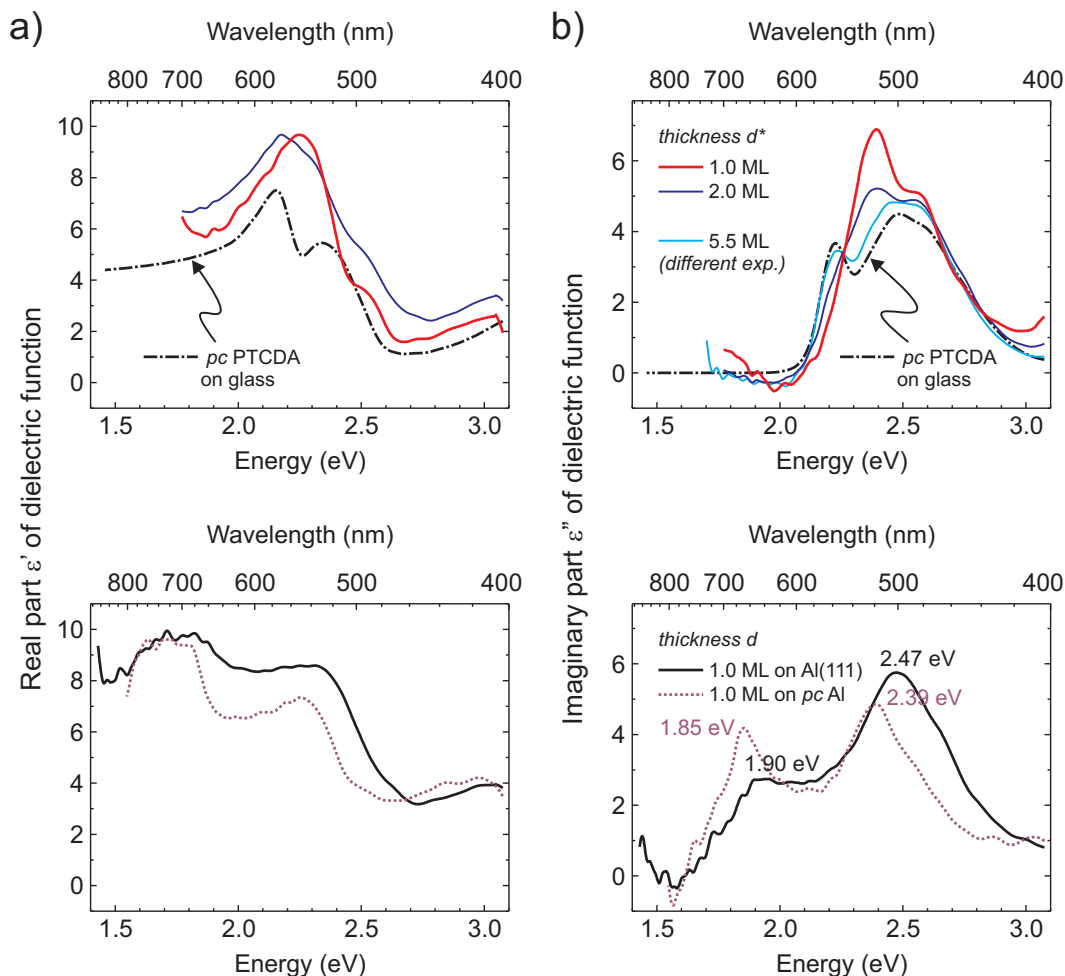
Figure 4.12: **a)** Real part ε', and **b)** imaginary part ε'' of the dielectric function $\hat{\varepsilon} = \varepsilon' - i\varepsilon''$ of PTCDA deposited on Al(111). For $d = 1\,\text{ML}$ (lower panels) $\hat{\varepsilon}$ was extracted from the original DRS shown in Figure 4.6. The dotted curves represent an identical thickness of $d = 1\,\text{ML}$, but deposited on polycrystalline (*pc*) Al. For thicknesses of $d > 1\,\text{ML}$ (i.e., $d^* > 0\,\text{ML}$, upper panels) $\hat{\varepsilon}$ was extracted from the reduced DRS, i.e., DRS*, shown in Figure 4.11, see text for explanations. For clarity, only selected spectra are presented. The ε'' curve of $d = 5.5\,\text{ML}$ stems from a different experiment on Al(111) [180]. The independently determined $\hat{\varepsilon}$ spectrum of a comparatively thick polycrystalline (*pc*) PTCDA film on glass is shown in comparison (adapted from Ref. [65]).

$E \gtrsim 2.2\,\text{eV}$ for $d \approx 1\,\text{ML}$, though considerably broadened by the still present Al surface. The feature at $\approx 1.90\,\text{eV}$ is at too low energies to be attributed to the absorbance of neutral PTCDA monomers. As the difference in energy to the peak at $2.47\,\text{eV}$ is $\Delta E \approx 0.57\,\text{eV}$, this feature is presumably caused by negatively charged PTCDA, i.e., PTCDA$^{\bullet-}$, and not by PTCDA$^{\bullet+}$. The comparison with absorption data of neutral and charged DBPI and PBI in solution [30, 31] also suggests that the transitions of the PTCDA anion should be found at lower energies with a difference of $\Delta E \gtrsim 0.5\,\text{eV}$, and those of the PTCDA cation of only $\Delta E \approx 0.28\,\text{eV}$, compared to the main transition of the

neutral molecule (cf. Figure 4.15 and Table 4.2). We conclude that the 1st ML of PTCDA on Al(111) comprises neutral molecules and anions as manifested by the different contributions to the broad ε'' spectrum.

Additionally, in Figure 4.12 (lower part) the extracted dielectric function for a similar measurement of $d \approx 1$ nm of PTCDA on polycrystalline (pc) Al is depicted. We can state that this broad spectrum is also dominated by two peaks, one at 2.39 eV and the other at 1.85 eV, with a difference in energy of $\Delta E \approx 0.54$ eV. These two peaks presumably have the same origin as those at 2.47 eV and ≈ 1.90 eV, respectively, on Al(111) discussed above, since only a small red-shift can be noticed. However, the peaks at 2.39 eV and 1.85 eV on pc Al are narrower than their counterparts on Al(111). We attribute this fact to a stronger oxidation of the pc Al surface which was sputtered and annealed in standard cycles of 15 min per step, as opposed to Al(111) which was repeatedly sputtered at higher intensities for 2 h while heated to 340 °C with subsequent annealing at 400 °C for 30 min [180]. Therefore, we assume the aluminum oxide layer on pc Al to be more pronounced than on Al(111) without knowing its exact thickness. Consequently, the signal at $E \gtrsim 2.2$ eV exhibits a stronger resemblance to the neutral monomeric behavior, while the feature at 1.85 eV attributed to PTCDA$^{\bullet-}$ is more similar to the absorbance of negatively charged PTCDA derivatives (cf. Figure 4.15).

For PTCDA thicknesses of $d > 1$ ML (i.e., $d^* > 0$ ML) on Al(111), we observe once more a drastic change in the optical behavior (Figure 4.12, upper part). Up to $d^* = 1$ ML the slightly broadened spectral signature of monomeric PTCDA can be seen. The main transition is at 2.38 eV with shoulders at ≈ 2.58 eV and ≈ 2.73 eV, corresponding to a vibronic progression of $\Delta E_{\text{vibron}} \approx 0.18$ eV, similar to the value known for dissolved PTCDA. This means that we also observe a decoupling of the 2nd ML with respect to the 1st ML on Al(111). Hence, this appears to be a more general effect of thin PTCDA films on metal substrates. Due to the mentioned experimental difficulties linked to the Al(111) surface, one should not overestimate the spectral accuracy at both ends of the ε'' spectra here. Especially the non-zero part of the $d^* = 1$ ML spectrum at low energies might have been caused by a measurement artifact, i.e., drift (compare Figure 4.11). Increasing the film thickness up to $d^* \approx 5.5$ ML leads to the well-known aggregation expressed by the convergence toward the pc PTCDA bulk behavior.

4.5   PTCDA on HBC on Au(111)

Differential Reflectance Spectra.   Having studied PTCDA films grown on various metal surfaces as well as the associated coupling effects of the 1st ML, we are indeed reminded of the behavior of the first QT monolayer on Au(111) discussed in Section 3.2. In the course of our argumentation in Section 3.4, we

have also demonstrated that an effective decoupling can be readily achieved by a pre-deposited atomically thin spacer layer consisting of flat-lying densely packed HBC molecules. Such a functionalized (here in the sense of intentionally passivated) metal surface would be of even greater value if the effect was not limited to one specific combination of adsorbates, namely QT and HBC. With this motivation in mind, we performed similar measurements for PTCDA grown on an epitaxial monolayer of HBC on Au(111) monitored with DRS (cf. Figure 4.13). Note that in principle, this DRS corresponds to the reduced DRS, i.e., DRS*, here as the 1st ML of HBC is already ascribed to the substrate. A direct comparison with the previous experiments is also feasible since PTCDA films on HBC on Au(111) exhibit the flat-lying herringbone alignment known from the PTCDA bulk crystal, as evidenced by means of STM and LEED [42].
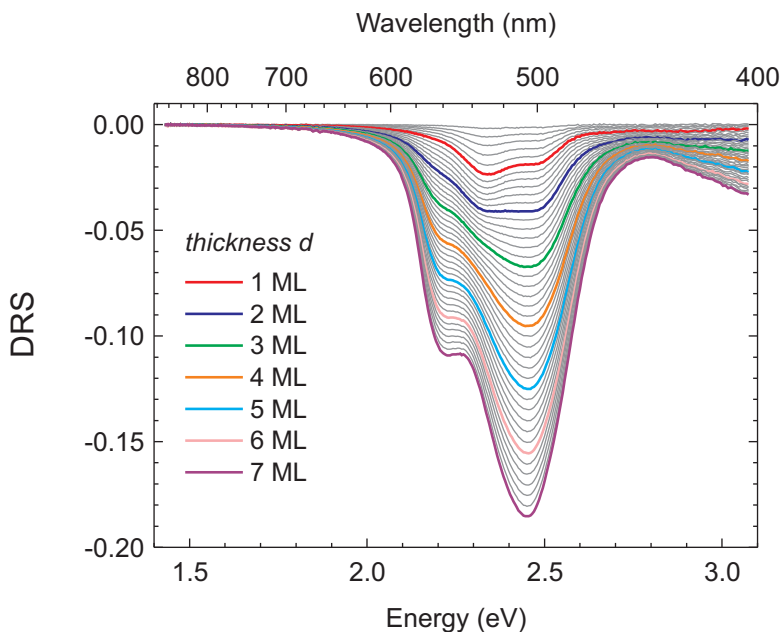

Figure 4.13: Drift-corrected differential reflectance spectra (DRS, Equation (2.12)) of PTCDA deposited on $1\,\mathrm{ML}$ of HBC on Au(111). The *total* nominal PTCDA film thicknesses d are given.

Dielectric Function Extracted from DRS. The complex dielectric function extracted from the DRS is depicted in Figure 4.14. It reveals general characteristics similar to those of the decoupled PTCDA films in the preceding sections. In terms of the ε'' spectra we observe a monomeric shape for the first PTCDA monolayer being slightly broadened. A deconvolution of the $d = 1\,\mathrm{ML}$ spectrum by means of Gaussian fitting yields peaks at $2.33\,\mathrm{eV}$, $2.50\,\mathrm{eV}$, and $\approx 2.66\,\mathrm{eV}$ stemming from the spectral fingerprint of PTCDA monomers and, additionally, two weaker features at $\approx 2.16\,\mathrm{eV}$ and $\approx 1.98\,\mathrm{eV}$ that are necessary to match the low energy tail of this spectrum. The latter two might actually be an artificial expression of the slightly broader appearance of this
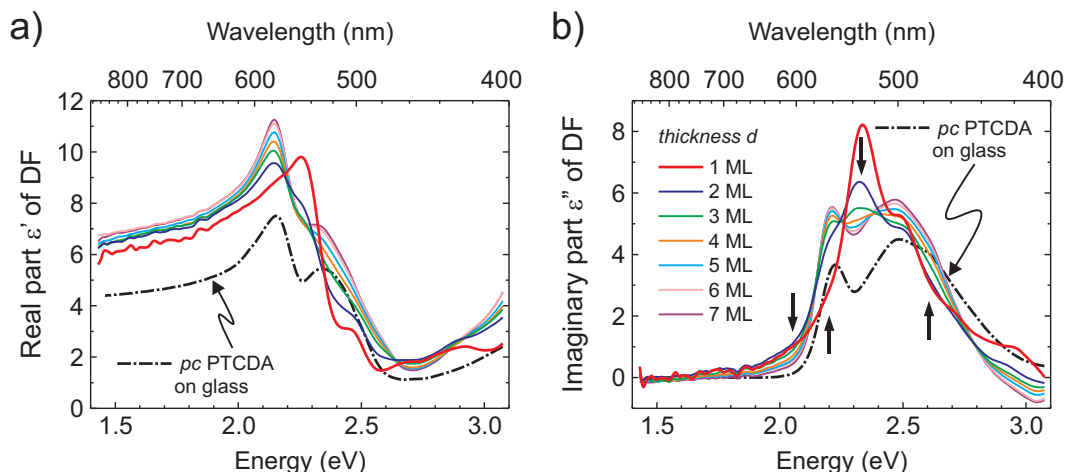
Figure 4.14: **a)** Real part ε', and **b)** imaginary part ε'' of the dielectric function $\hat{\varepsilon} = \varepsilon' - i\varepsilon''$ of PTCDA deposited on $1\,\mathrm{ML}$ of HBC on Au(111) [DF = dielectric function]. For all PTCDA thicknesses $\hat{\varepsilon}$ was extracted from the DRS shown in Figure 4.13. For clarity, only selected spectra are presented. The independently determined $\hat{\varepsilon}$ spectrum of a comparatively thick polycrystalline (*pc*) PTCDA film on glass is shown in comparison (adapted from Ref. [65]).

curve compared to the ε'' spectrum of $d^* = 1\,\mathrm{ML}$ of PTCDA on Au(111). Hence, if there is a small additional peak at $\approx 2.05\,\mathrm{eV}$ originating from charge transfer, it might be concealed by a predominant overall broadening. Therefore, we can not unambiguously identify PTCDA cations here, and if charging does occur, it would be at least strongly suppressed compared to PTCDA films directly on Au(111).

Upon increasing film thickness, aggregation sets in, as manifested by the fast saturation of the dielectric function which becomes comparable to that of a rather thick film of polycrystalline (*pc*) PTCDA (cf. Ref. [65]). However, the magnitudes of the ε' and ε'' spectra are too high by a factor of ≈ 1.5 compared to the *pc* PTCDA data. This might be due to an imprecise film thickness determination, probably caused by a different growth mode. At present, we can not explain this circumstance with absolute certainty.

4.6   Summary and Comparative Discussion

4.6.1   Absorbance of PTCDA Derivatives in Solution

For the sake of completeness, we want to collect here the most characteristic ε'' spectra discussed in the preceding sections. Since the optical response of the 1$^{\text{st}}$ and 2$^{\text{nd}}$ MLs of PTCDA are most severely affected by the presence of the metal substrates, they are compiled in Figure 4.15. They are compared to absorbance data of dissolved DBPI and PBI in the neutral, anionic, and cationic states [30, 31], as also summarized in Table 4.2. It is remarkable

that on all metal surfaces considered the spectra of $d^* \approx 1\,\mathrm{ML}$ of PTCDA are very similar for $E \gtrsim 2.2\,\mathrm{eV}$ clearly showing the spectral fingerprint of the neutral PTCDA monomer with different degrees of broadening, i.e., the 2nd ML behaves optically as if it were deposited on an insulating substrate.
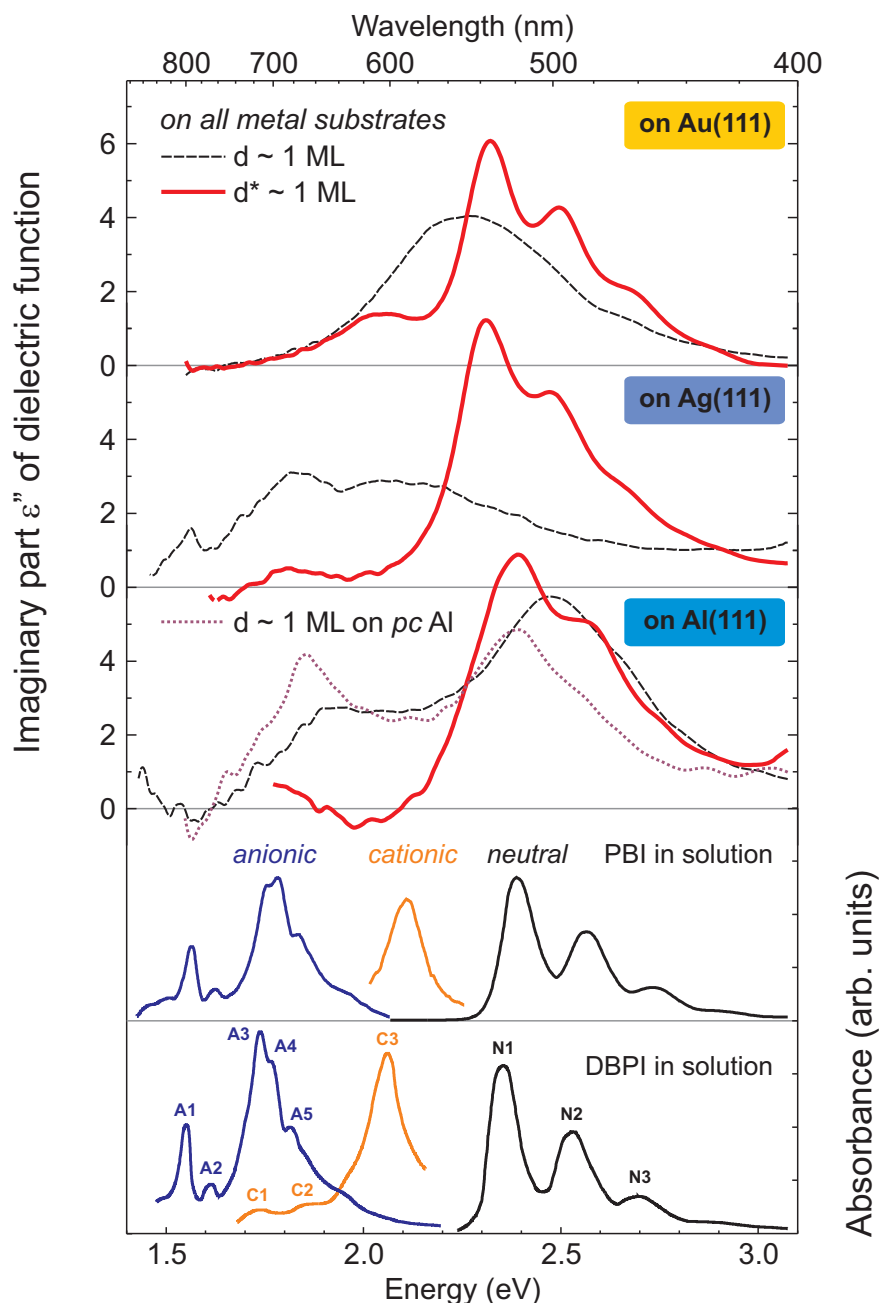

Figure 4.15: Comparison of the most characteristic ε'' spectra for $d \approx 1\,\mathrm{ML}$ (−−) and $d^* \approx 1\,\mathrm{ML}$ (—) of PTCDA on Au(111), Ag(111), and Al(111). The ε'' spectrum for $d \approx 1\,\mathrm{ML}$ (···) of PTCDA on polycrystalline (*pc*) Al is also plotted. These spectra are compared to absorbance data of dissolved DBPI and PBI in the neutral, anionic, and cationic states, not to scale (adapted from Refs. [30, 31]).

Table 4.2: Suggested spectral assignment of identifiable absorption peaks for different PTCDA systems compared to known literature data for dissolved PBI and DBPI. The nomenclature follows that in Figure 4.15, all values are given in eV. The strongest transition for each charged state is shown in bold. Weak features with lower confidence level are given in parentheses. For anionic PTCDA on the solid substrates listed here, it is assumed that the comparatively broad peak at $\approx 1.85\,\mathrm{eV}$ is a superposition of at least A3, A4, and A5 (and perhaps less pronounced shoulders), whose relative intensity might be subject to variations (as also evident for A3 and A4 when comparing PBI$^{\bullet-}$ and DBPI$^{\bullet-}$).

System	anionic					cationic			neutral		
	A1	A2	A3	A4	A5	C1	C2	C3	N1	N2	N3
PBI in solution*	1.56	1.62	1.75	**1.78**	1.83	–	–	**2.11**	**2.39**	2.57	2.74
DBPI in solution†	1.55	1.61	**1.74**	1.77	1.81	(1.73)	(1.86)	**2.06 or 2.08**	**2.36**	2.53	2.70
PTCDA on Au(100) - 1st ML	–	–	–	–	–	*very broad signal, cationic contribution likely*			**2.32**	2.49	(2.66)
PTCDA on Au(100) - 2nd ML	–	–	–	–	–	(1.69)	(1.85)	**2.03**	**2.32**	2.49	(2.66)
PTCDA on Au(111) - 1st ML	–	–	–	–	–	*very broad signal, cationic contribution likely*			**2.32**	2.49	(2.66)
PTCDA on Au(111) - 2nd ML	–	–	–	–	–	–	–	**2.05**	**2.33**	2.50	(2.66)
PTCDA on HBC on Au(111) - 1st ML	–	–	–	–	–	–	(1.98)	(2.16)	**2.31**	2.47	(2.64)
PTCDA on Ag(111) - 1st ML	1.56	–	–	**1.85**	–	*very broad signal, cationic contribution unlikely*			–	–	–
PTCDA on Ag(111) - 2nd ML	–	–	–	(1.85)	–	–	–	–	–	–	–
PTCDA on Al(111) - 1st ML	–	–	–	**1.90**	–	*cation unlikely*			**2.47**	*broad*	
PTCDA on Al(111) - 2nd ML	–	–	–	–	–	–	–	–	**2.38**	(2.58)	(2.73)
PTCDA on (oxidized) pc Al - 1st ML	–	–	–	**1.85**	–	*cation unlikely*			**2.39**	*broad*	
PTCDA on mica + K-doping‡ - 1st ML	1.57	(1.63)	–	**1.85**	–	–	–	–	**2.35**	2.53	2.71

*From Kircher et al. (Ref. [30]) for comparison.
†From Ford et al. (Ref. [31]) for comparison. There, different ionization methods were employed for the cation, thus two different energies are given for C3.
‡From PhD thesis of Thomas Dienel (Ref. [181]) for comparison.

4.6.2   Electronic Structure on Metal Surfaces

Finally, we discuss our findings in the view of electronic coupling and energy level alignment with the respective substrates. Two different approaches will be presented in the following: *(i)* the HOMO/LUMO alignment picture, and *(ii)* the integer charge transfer (ICT) model.

HOMO/LUMO Alignment.   The electronic structure of thin PTCDA films on various metal surfaces has been intensively studied in the recent past [36, 158, 160–162, 179, 182]. In the majority of these publications, it is postulated that the capability to transfer charge is determined by the alignment of the HOMO and LUMO of PTCDA (or levels derived from these molecular orbitals) with respect to the metal Fermi energy E_F, driven by the reactivity of the metal, i.e., the tendency to form covalent bonds with the organic adsorbate. This picture is visualized in Figure 4.16.
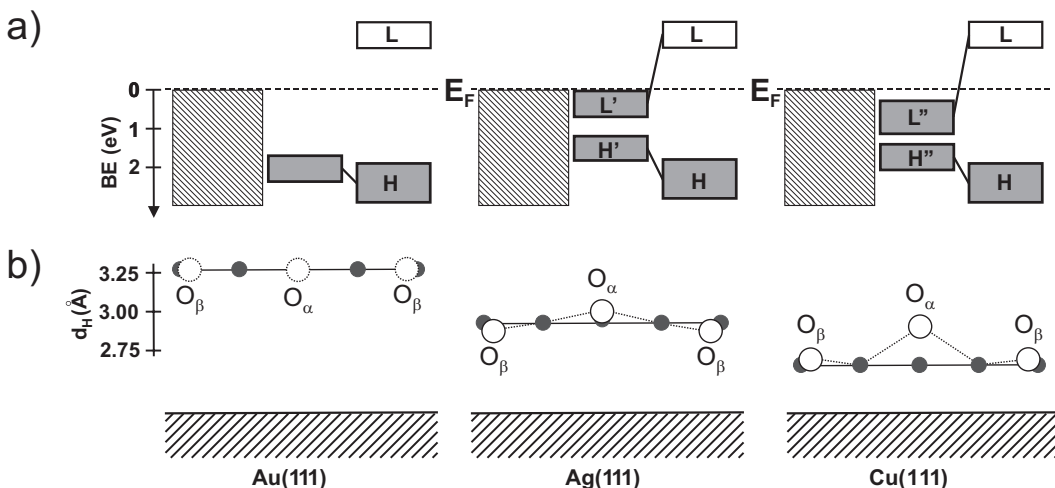
Figure 4.16: **a)** Schematic energy diagrams of PTCDA thin films on Au(111), Ag(111), and Cu(111) [BE = binding energy]. The pristine metal substrates are shaded. The level alignment of the interface layer and of the multilayer follow from left to right. Occupied levels (filled rectangles) were measured with UPS [161]. The relative positions of the unoccupied levels (open rectangles) were estimated from inverse photoelectron spectroscopy (IPES) [182]. HOMO and LUMO are labeled H and L, while the HOMO and LUMO derived states of the interface layers are labeled H′ or H″ and L′ or L″, respectively. **b)** Bonding distances d_H with respect to the surfaces, measured with the x-ray standing wave (XSW) technique [33, 183, 184]. Gray filled circles represent carbon, open circles represent oxygen atoms (O_α = anhydride, O_β = carboxylic). The positions of O_α and O_β on Au(111) were not measured and are assumed to be in the molecular plane (undistorted molecules). Reproduced from Ref. [161].

It is a well-established fact that the Ag(111) surface induces a profound alteration of the molecular levels of adsorbed PTCDA [160, 161]. In this case, the electronic coupling is strong enough to pull down the LUMO of PTCDA

below the Ag Fermi edge leading to a partial filling of what used to be the LUMO before the actual deposition (cf. Figure 4.16a). Consequently, PTCDA is covalently bound to the Ag(111) surface ("chemisorption"), and negatively charged molecules are located at this interface. However, the measured alteration of the workfunction of only $\approx 0.1\,\mathrm{eV}$ is by far too small for such a pronounced charge transfer [160, 161]. This discrepancy was explained by the occurrence of charge back-donation from PTCDA to Ag(111), including at least the former HOMO and the HOMO-1, which also seem to shift in energy [160]. Therefore, the *net* charge transfer is small but not necessarily zero, and charged molecules may actually exist in the 1$^{\mathrm{st}}$ ML of PTCDA on Ag(111). Still, it remains a speculative matter whether the optical features at $\approx 1.56\,\mathrm{eV}$ and $\approx 1.85\,\mathrm{eV}$ observed here can really be assigned to PTCDA$^{\bullet-}$, since all the molecular levels close to the gap are involved in the energetic realignment, and electronic transitions are thus difficult to be categorized. A univocal interpretation is further hampered as the molecular geometry becomes considerably distorted upon the formation of covalent bonds, where the carboxylic (outer) oxygen atoms are bent toward and the anhydride (inner) oxygen atoms are bent away from the Ag(111) surface (cf. Figure 4.16b). The UPS data for PTCDA multilayers on Ag(111), however, are almost identical to those on Au(111) or Cu(111) [160, 161], speaking for a much weaker influence of the respective substrates on the molecular frontier levels. This fact renders the observation of the spectral fingerprint of neutral PTCDA monomers in the 2$^{\mathrm{nd}}$ MLs plausible, except for the optical features at $E \lesssim 2.2\,\mathrm{eV}$ on Au and Al which are attributed here to charge transfer.

The situation changes when a rather inert noble metal, such as Au(111), is used as a substrate. It is stated in a recent UPS study that "...*no clear signature of molecule–metal reaction-induced peaks within the energy gap region of PTCDA was observed in the spectra of PTCDA/Au(111), even at sub-monolayer coverage. [...] If the charge transfer for PTCDA/Au(111) were very small, the experimental observation would merely be limited by the fact that the newly induced density of states is simply too low to be detected [by UPS].*" [161]. Consequently, PTCDA on Au(111) has been classified as a weakly interacting system [161, 179]. The measured position of the PTCDA HOMO is not significantly altered by the presence of the Au(111) surface, cf. Figure 4.16a. Thus, it seems contradictory to optically detect a (partly) positively charged 2$^{\mathrm{nd}}$ ML as claimed above. The interface dipole formation between 1$^{\mathrm{st}}$ and 2$^{\mathrm{nd}}$ MLs of PTCDA on the respective metals was not considered as a central aspect in the HOMO/LUMO alignment picture outlined above, and therefore charging of the 2$^{\mathrm{nd}}$ ML of PTCDA, especially on Au(111), is generally believed to be irrelevant. However, we would like to demonstrate in the following that another model might be better suited to describe the interface formation, particularly between the 1$^{\mathrm{st}}$ and the 2$^{\mathrm{nd}}$ MLs.

Integer Charge Transfer Model (ICT).   It is in general recognized that the electronic behavior of the 1st ML of PTCDA on various metal surfaces differs fundamentally from that of further layers grown on top [160, 161]. We also demonstrated here that the 2nd ML of PTCDA on the respective metals behaves optically as if it were deposited on an *insulating* substrate. This electronic decoupling is corroborated by the occurrence of vibrationally resolved monomeric spectra similar to isolated molecules. The interface between 1st and 2nd MLs is therefore characterized by a negligible hybridization of the adsorbate and substrate wavefunctions and can hence be adequately described as an organic–organic heterojunction. It is of vital importance to realize that for the 2nd ML of PTCDA, the "substrate" comprises the metal surface *and* the 1st ML of PTCDA which is rather strongly hybridized to the latter as evidenced by UPS and also manifested in the broad optical spectra. Consequently, the
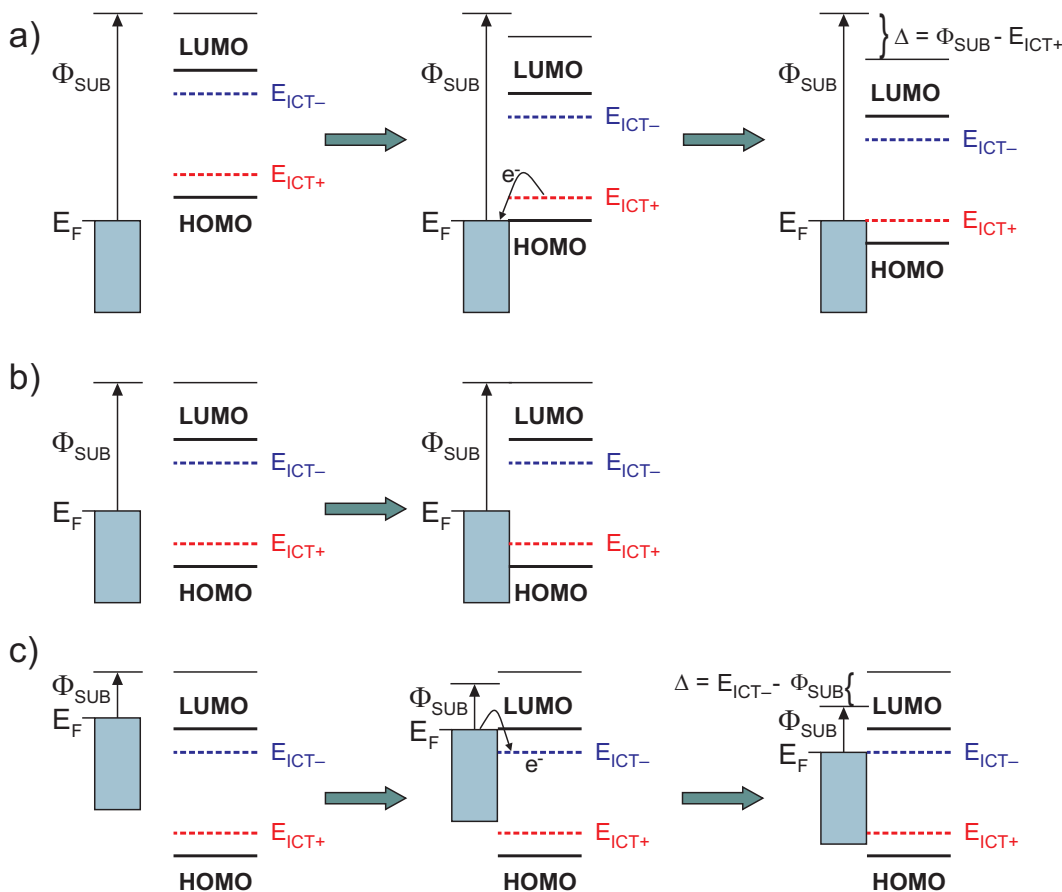
Figure 4.17: Schematic illustration of the integer charge transfer (ICT) model. Proportions are exaggerated to aid the viewer. In our three-phase approach, the substrate characterized by the workfunction Φ_{SUB} comprises the metal *and* the 1st ML of PTCDA. **a)** $\Phi_{SUB} > E_{ICT+}$, charge transfer from the adsorbate to the substrate and Fermi level pinning to E_{ICT+}. **b)** $E_{ICT-} < \Phi_{SUB} < E_{ICT+}$, no charge transfer, but vacuum level alignment ($\Delta = 0$). **c)** $\Phi_{SUB} < E_{ICT-}$, charge transfer from the substrate to the adsorbate and Fermi level pinning to E_{ICT-}. Reproduced from Ref. [26].

total substrate (i.e., metal + 1$^{\text{st}}$ ML of PTCDA) is characterized by the workfunction Φ_{SUB}. Such organic–organic interfaces or interfaces between organic molecules and passivated (e.g., oxidized or covered with residual hydrocarbons) substrates can be favorably described by the integer charge transfer (ICT) model [26]. In this case, the decoupling of the molecular π-electrons from the substrate wavefunctions prevent a partial electron transfer. For sufficiently thin passivating layers (e.g., flat-lying aromatic monolayers) electrons can still be transferred via tunneling, provided that the substrate workfunction Φ_{SUB} is greater (smaller) than the energy required to form a positively $[E_{\text{ICT+}}]$ (negatively $[E_{\text{ICT-}}]$) charged state in the organic compound.* The resulting self-localized charged states are called polarons. The ICT states appear as new features in the otherwise forbidden energy gap of the molecules, separated from the HOMO/LUMO edges. The charge transferred from the molecules to the surface in proximity is located nearby enabling Coulomb interaction, unlike in PES or IPES experiments, for example. In conclusion, it has been proposed that *"...for all cases except highly crystalline molecular films showing band-like transport, the position of the HOMO and LUMO relative to the vacuum level are not the relevant energies to determine the energy-level alignment at this type of weakly interacting interfaces."* [26]. Instead, the ICT model applies, which is depicted in Figure 4.17. Three possible cases can be distinguished:

a) $\Phi_{\text{SUB}} > E_{\text{ICT+}}$: Electrons tunnel spontaneously from the organic adsorbate into the substrate. Charge depletion in the molecular film and accumulation at the substrate side of the interface create a dipole lowering the vacuum level. Equilibrium is reached when $E_{\text{ICT+}} + \Delta = \Phi_{\text{SUB}}$.

b) $E_{\text{ICT-}} < \Phi_{\text{SUB}} < E_{\text{ICT+}}$: Spontaneous charge transfer across the interface does not occur. Vacuum level alignment is achieved.

c) $\Phi_{\text{SUB}} < E_{\text{ICT-}}$: Electrons tunnel spontaneously from the substrate into the organic adsorbate. Charge accumulation in the molecular film and depletion at the substrate side of the interface create a dipole raising the vacuum level. Equilibrium is reached when $E_{\text{ICT-}} - \Delta = \Phi_{\text{SUB}}$.

At first glance, the workfunctions of the substrates used here $\Phi_{\text{Au}} > \Phi_{\text{Ag}} > \Phi_{\text{Al}}$ might suggest a direct classification. However, as already stated above, the relevant substrate is the metal surface passivated by the 1$^{\text{st}}$ ML of PTCDA or, alternatively, by (partial) oxidation in the case of Al.

The workfunction of pristine Au(111) is decreased from $\Phi_{\text{Au(111)}} = 5.15\,\text{eV}$ to $4.95\,\text{eV}$ upon deposition of $0.1\,\text{nm}$ of PTCDA and further to $4.70\,\text{eV}$ up to

---

*$E_{\text{ICT+}}$ ($E_{\text{ICT-}}$) is defined as the amount of energy necessary to eject (add) one electron from (to) the molecule forming an electronically and geometrically fully relaxed state including substrate screening.

a film thickness of 4.8 nm [161]. This suggests that the workfunction is indeed lowered upon adsorption of the 2nd ML of PTCDA here, and consequently, this interface can be assigned to *case a)* of the ICT model. This complies with our observation of molecular cations in the 2nd ML of PTCDA on Au(111) and Au(100), see Section 4.2.

The workfunction of pristine Ag(111) is decreased from $\Phi_{Ag(111)} = 4.90\,eV$ to 4.80 eV upon deposition of 0.1 nm of PTCDA. For further increasing film thickness it is explicitly stated that this value remains constant [161] suggesting that *case b)* of the ICT model applies here. Consequently, no charge transfer to the 2nd ML of PTCDA is expected at all, as also deduced from the respective optical spectra, see Section 4.3.

For the Al(111) or *pc* Al substrates we observe PTCDA anions in the 1st ML of PTCDA which may indicate passivation by a thin oxide layer. Partial or complete oxidation of these highly reactive surfaces is indeed likely for the experimental constraints discussed earlier. Therefore, we assume that the ICT model is also applicable and conclude from our optical results that *case c)* is appropriate here, see Section 4.4. Unfortunately, there are no photoelectron spectroscopy measurements available that could verify this hypothesis.

Admittedly, our reasoning why we observe charged PTCDA, especially in the optical spectra of the 2nd ML on Au(111), is still a matter of debate. The following statement can be drawn from a recent density functional theory (DFT) study favoring the HOMO/LUMO alignment picture: *"The fact that the occupied levels of PTCDA lie substantially below E_F indicates that the charge transfer from the molecular region to the surface is due to the pillow effect, and is not an electron donation from the highest occupied molecular orbital (HOMO) to the metal."* [163]. Note that a thorough theoretical analysis of large aromatic molecules adsorbed on metal surfaces is still rather demanding, and can lead in part to contradictory conclusions [163, 179]. While DFT can achieve consistency with the experimental determination of the workfunction modification and the HOMO/LUMO alignment with respect to the substrate Fermi energy, a reliable prediction of the optical absorption behavior of such systems is currently not feasible. Calculations of stacked PTCDA, i.e., 2 ML or more on a metal surface, are not available at present.

4.7   Conclusions

In conclusion, we have demonstrated that thin PTCDA films on various metals behave somewhat counterintuitively: The first monolayer couples to the respective substrates in such a manner that the second layer is electronically decoupled to a large extent, as substantiated by the vibrationally resolved monomer-like spectra there. Dimerization between the first two adjacent monolayers does not occur and only sets in after completion of the second

layer. This pronounced decoupling from the substrate is evidently present on insulating surfaces [32, 37]. On metal substrates, however, it had only been achieved so far by inserting an organic spacer layer with an entirely different electronic structure than the molecular compound grown on top (QT on HBC on Au(111), compare Section 3.4, or PTCDA on HBC on Au(111), compare Section 4.5). We conclude that the energy levels of the first PTCDA ML on Au must also differ considerably from the levels of decoupled PTCDA in the subsequent layers, thereby inhibiting noticeable coupling.

Yet, the most important result is the occurrence of new peaks in the ε'' spectra of the second PTCDA ML at lower photon energies of $E \lesssim 2.2\,\text{eV}$. By comparison to literature optical absorption data of similar molecular species [30, 31], we attribute the feature at $2.05\,\text{eV}$ on Au(111) to PTCDA radical cations (PTCDA$^{\bullet+}$). On Ag(111) no clear feature was detected at low E, indicating a mostly neutral second ML of PTCDA there. Al(111) and polycrystalline Al with different degrees of oxidation revealed a new feature at $\approx 1.85\,\text{eV}$ which we assign to PTCDA radical anions (PTCDA$^{\bullet-}$). This feature is already present in the first ML on the Al surfaces, which might be due to a thin aluminum oxide film that plays a similar role as the passivating first PTCDA MLs on Au(111) and Ag(111), respectively.

Two dissimilar approaches were discussed in order to explain our findings. The HOMO/LUMO alignment picture [161] which implicates the charge transfer to be caused solely by the formation of covalent bonds turned out to be conflicting with our results, in particular concerning the positive charging of the second PTCDA ML on Au(111) suggested here. The integer charge transfer (ICT) model based on electron tunneling [26] can at least qualitatively describe the different charge transfers proposed by us for the various substrates used. While the first approach is dominant in the literature associated with PTCDA, the applicability of the second approach as discussed here is still a matter of debate. Unfortunately, photoelectron spectroscopy measurements of PTCDA on Al, which could readily clarify our hypothesis, are not available up to now, which is presumably due to the inferior controllability of the quality of such highly reactive surfaces.

5   General Conclusions and Future Perspectives

It was one essential objective of this thesis to convince the reader that differential reflectance spectroscopy (DRS) is indeed a valuable tool for the investigation of electronic coupling effects between molecular epitaxial layers and a variety of substrates. The surface-sensitive character of this technique is very beneficial for its capability to monitor the film growth in real-time, thereby closely following the interface formation, which grants access to the associated physical effects beginning at the layer of contact. The use of extended polycyclic aromatic hydrocarbons is particularly advantageous since the molecules' centers of gravity are often largely separated, even in a densely packed layer. This leads to a small and negligible in-plane excitonic interaction. On the other hand, we can directly probe those interactions, if the molecules are arranged in π–π-stacks, by employing the ensemble effect. By that, we can directly observe the monomer–dimer–oligomer transition in the absorption behavior of van der Waals bound, vertical molecular "chains".

In contrast to previous studies using insulating substrates [32, 37], we have seen that similar flat-lying aromatic molecules used here exhibit a rather strong electronic coupling to metal surfaces, whereas this coupling is less pronounced on semimetallic graphite. A pre-deposited atomically thin spacer layer consisting of a different aromatic compound can readily lead to an efficient electronic decoupling from the subjacent metal, as manifested by the vibrationally resolved monomeric spectra of the molecular layer grown on top. Moreover, we have demonstrated charge transfer effects in some cases by the occurrence of additional features in the optical spectra, surprisingly not limited to the first molecular layer. Furthermore, DRS is especially powerful in combination with structural analysis methods, since the molecular orientation has a large impact on the physical properties. To a certain extent it is even possible to deduce some structural information from the optical spectra making use of the anisotropic film structures produced.

There are a few limitations to the applicability of DRS. First, one would preferentially employ molecular adsorbates whose crystal structures are accompanied by a rather strong excitonic coupling. This enhances the observability

of aggregation effects when passing from a single monolayer (with monomeric spectral character) to stacked multilayers (with non-negligible excitonic inter-actions, as in the case of PTCDA films, for example) and hence facilitates the interpretation of the film thickness-dependent DRS. Second, one has to arrange for suitable molecule–substrate combinations which can have a strong impact on the absolute intensity of the DRS due to the inherent optical functions of the respective substrates. In some cases (e.g., HBC on Au) the molecu-lar absorption band under consideration coincides with a rather inconvenient optical behavior of the substrate which can conceal the adsorbate contribu-tion to the DRS. Third, the DRS on opaque substrates can only be indirectly interpreted as absorption behavior of the molecular film using a model-free numerical algorithm based on the Kramers-Kronig relations implying some additional requirements [78].

In this comparative study, we have also demonstrated that, similar to in-organic heteroepitaxy, the physical properties of an organic heterosystem are not just the sum of the properties of the two single materials, which opens up chances to tune organic layer properties to demand. In the future, heteroepi-taxial architectures may provide the opportunity to modify the electronic prop-erties of certain substrates. Even sub-nanometer thin monolayers are capable of decreasing or increasing the substrate workfunction Φ. An adequate choice of the molecular contact layer composition can hence allow for an adjustment of the electronic level alignment at the interface with subsequent organic lay-ers. Such an iterative workfunction modulation is of particular interest for the injection of charges at metal–organic contacts, which is crucial for the perfor-mance of a device. Moreover, it appears beneficial to investigate the intentional doping of molecular layers in the proximity of metal contacts with our optical DRS technique. Doping with alkali metals has already been monitored with DRS on insulating surfaces [181]. Pursuing this matter can be worthwhile for stacked heteroepitaxial structures, as a single specific layer can be doped and perhaps sandwiched between undoped layers. This issue is also stimulating from the point of view of possible charge transfer between adjacent molecular layers and/or to the respective substrate, especially if an efficient electronic decoupling from a metal surface is found for the undoped case. On the other hand, localized traps in the form of charged molecules may serve as a blocking layer for one charge carrier type (hole or electron) under certain conditions. Finally, *multiple* organic quantum wells on the molecular scale are expected to move into focus, in analogy to their inorganic counterparts. First prototypes comprising alternately deposited layers, for instance quaterrylene and *N*,*N*'-di-octyl-3,4,9,10-perylenedicarboximide [185], have already been realized. Given the importance of inorganic heterostructures for up-to-date optoelectronic de-vices, we anticipate that epitaxial organic heterostructures, especially organic quantum wells, will lead to new classes of organic-based applications.

Appendix

Comparison of Analysis Methods. A closeup view of the DRS* of $d^* = 1\,\mathrm{ML}$ of PTCDA on Au(111) as plotted in Figure 4.4 is given in Figure A.1a on an inverted scale for convenience. Additionally, the substrate coefficients A and B for gold, as shown in Figure 2.9, are depicted. They are derived from the substrate bulk dielectric function $\hat{\varepsilon} = \varepsilon' - i\varepsilon''$. It was shown in Section 2.3 that the DRS can be approximated by $\mathrm{DRS} \approx -(8\pi d/\lambda) \times A \times \varepsilon''_{\mathrm{film}}$ provided that the condition $|A| \gg |B|$ is fulfilled. This so-called McIntyre approximation is also valid for DRS* and d^* with similar accuracy. It can be seen in Figure A.1a that $|A| \gg |B|$ holds indeed for gold at low photon energies $E \lesssim 2.2\,\mathrm{eV}$. Then, two completely *independent* analysis methods can be used to extract the imaginary part $\varepsilon''_{\mathrm{film}}$ of the adsorbate dielectric function: *(i)* the McIntyre approximation given in Section 2.3, and *(ii)* the model-free numerical algorithm based on the Kramers-Kronig transformation.
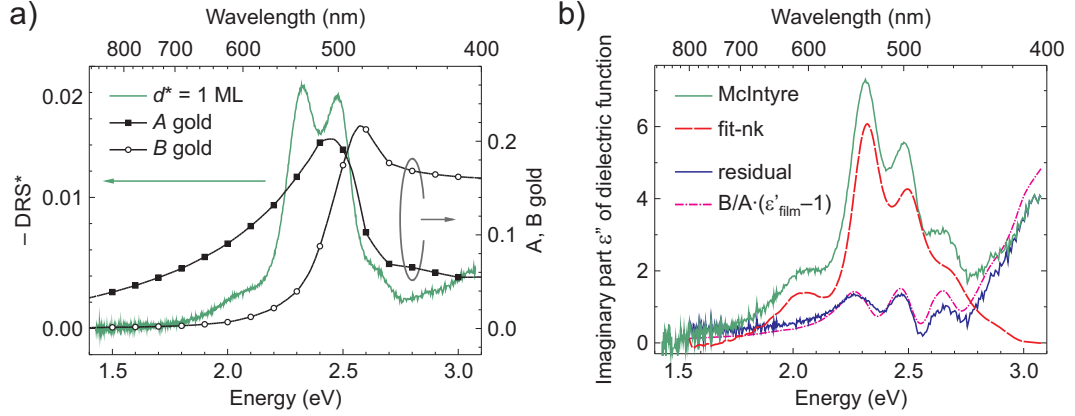
Figure A.1: Comparison between the analytical McIntyre approximation and the numerical `fit-nk` algorithm based on exact formulas. **a)** Measured DRS* of $d^* = 1\,\mathrm{ML}$ (0.32 nm) of PTCDA on Au(111), cf. Figure 4.4. The vertical scale is inverted (i.e., $-\mathrm{DRS}^*$) for convenience. For comparison, the A- and B-coefficients of gold (compare Figure 2.9) are plotted on a different scale, demonstrating that $|B| \ll |A|$ for energies below $\approx 2.2\,\mathrm{eV}$. **b)** Imaginary part ε'' of the dielectric function of the PTCDA film derived from the measured DRS* shown in (a) by two *independent* methods: *(i)* via the McIntyre approximation (Equation (2.54) $\Rightarrow \varepsilon'' \approx -\mathrm{DRS}^*/[A \cdot 8\pi d^*/\lambda]$, no noise filtering), and *(ii)* using the `fit-nk` algorithm (smoothed).

It is evident in Figure A.1b that both methods yield comparable results, and especially the position and the shape of the peaks are indeed very similar. Admittedly, the overall height of these two spectra is not identical, which is particularly apparent for high photon energies, where the condition $|A| \gg |B|$ is invalid for gold, and hence the McIntyre approximation can not be applied. Still, it is very clear from Figure A.1b that a peak at $2.05\,\mathrm{eV}$ (see above) is observed for both analysis techniques, and no artificial features are introduced by the numerical method chosen for the evaluation of our data. Note that for the McIntyre approximation and the `fit-nk` algorithm an identical PTCDA film thickness of $d^* = 0.32\,\mathrm{nm}$, corresponding to monolayer coverage, was used as parameter. For this reason, the uncertainty in d^* does *not* affect the comparison made in Figure A.1b. In order to corroborate this statement we simultaneously varied d^* for both methods from $0.256\,\mathrm{nm}$ to $0.384\,\mathrm{nm}$ using the very same DRS* spectrum of $d^* = 1\,\mathrm{ML}$ of PTCDA on Au(111) as plotted in Figure A.1a. We find that there is almost no variation in the shape and the position of the spectra, except for different respective magnitudes, of course. Hence the difference between the McIntyre approximation and the `fit-nk` algorithm in Figure A.1b must have a different origin, possibly associated with the validity of Equation (2.54). In fact, rewriting Equation (2.51) yields:

$$\underbrace{-\frac{\mathrm{DRS} \cdot \lambda}{8\pi d \cdot A}}_{\text{``McIntyre approximation''}} \approx \varepsilon_2'' + \underbrace{\frac{B}{A} \cdot (\varepsilon_2' - 1)}_{\approx 0 \text{ for } |A| \gg |B|} \quad . \tag{A.1}$$

The notation in terms of DRS and d is in good approximation also valid for DRS* and d^*. In Figure A.1b we actually compare $-\mathrm{DRS}^* \cdot \lambda / (8\pi d^* \cdot A)$ and ε_2'', the latter being extracted using the `fit-nk` algorithm. The residual between both should thus be equal to $B/A \cdot (\varepsilon_2' - 1)$. This is indeed confirmed in Figure A.1b where both quantities are plotted for comparison, using ε_2' for $B/A \cdot (\varepsilon_2' - 1)$ from the `fit-nk` algorithm. Hence, the difference between the McIntyre approximation and the `fit-nk` algorithm stems from neglecting the additional term associated with the ratio of the substrate coefficients B/A, which itself is in general energy-dependent. Consequently, the residual term can be much smaller for certain spectral ranges (e.g., at low energies for gold), as also evident in Figure 2.10 on page 33. We have therefore demonstrated that both analysis techniques yield almost identical results. As the numerical extraction of the dielectric function allows for a simultaneous determination of ε_2' and ε_2'', and as it is further not limited by the assumptions made for the derivation of the McIntyre approximation, it is considered superior.

PTCDA on Au(100).   As already mentioned in Section 4.2, we would like to briefly present the results obtained for PTCDA on Au(100) here in order to demonstrate that they are indeed very similar to those on Au(111). For the sake of completeness, the DRS as a function of PTCDA film thickness on
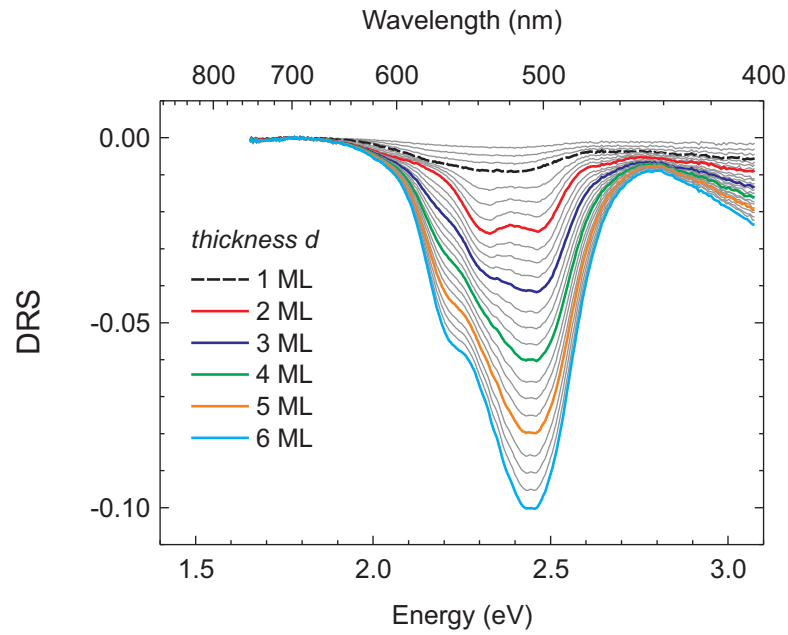
Figure A.2: Drift-corrected differential reflectance spectra (DRS, Equation (2.12)) of PTCDA deposited on Au(100). The *total* nominal film thicknesses d are given.
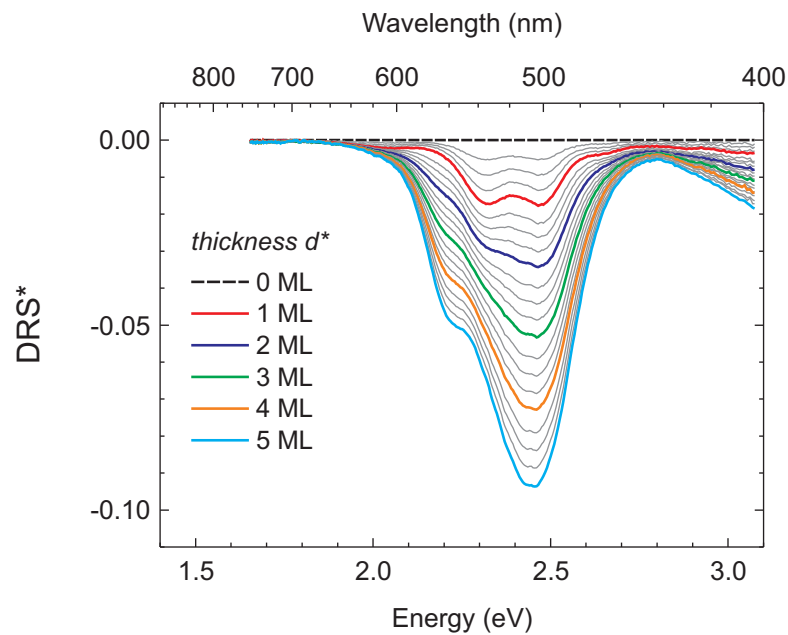

Figure A.3: Drift-corrected differential reflectance spectra (DRS*, Equation (4.1)) of PTCDA deposited on Au(100). The *reduced* nominal film thicknesses $d^* = d - 1\,\mathrm{ML}$ are given, in contrast to Figure A.2. We thereby assume a hypothetical three-phase system (metal / $1^{\mathrm{st}}\,\mathrm{ML}$ PTCDA / $(n-1)\,\mathrm{MLs}$ PTCDA).

Au(100) is shown in Figure A.2, while the corresponding DRS* is depicted in Figure A.3. In the very same manner as in Section 4.2 we extract the complex dielectric function of these films using the `fit-nk` algorithm. The results are depicted in Figure A.4. In comparison with Figure 4.5 on page 85 a very
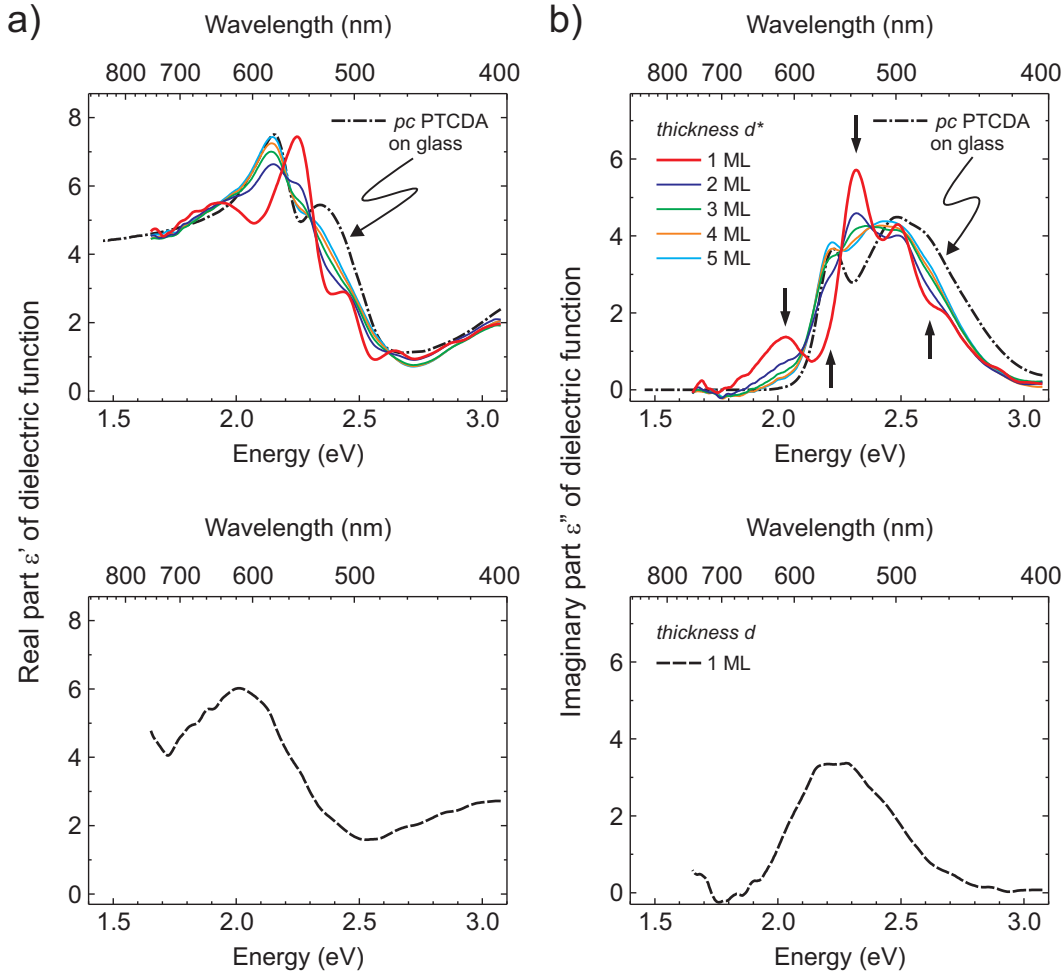
Figure A.4: **a)** Real part ε', and **b)** imaginary part ε'' of the dielectric function $\hat{\varepsilon} = \varepsilon' - i\varepsilon''$ of PTCDA deposited on Au(100). For thicknesses up to $d = 1\,\mathrm{ML}$ (lower panels) $\hat{\varepsilon}$ was extracted from the original DRS shown in Figure A.2. For thicknesses of $d > 1\,\mathrm{ML}$ (i.e., $d^* > 0\,\mathrm{ML}$, upper panels) $\hat{\varepsilon}$ was extracted from the reduced DRS, i.e., DRS*, shown in Figure A.3, see text for explanations. For clarity, only selected spectra are presented. Arrows indicate the spectral development with increasing film thickness. The independently determined $\hat{\varepsilon}$ spectrum of a comparatively thick polycrystalline (*pc*) PTCDA film on glass is shown in comparison (adapted from Ref. [65]).

good spectral agreement is evident. Therefore, all of the key statements about the optical spectra and their film thickness-dependent development made for PTCDA on Au(111) are equally valid on Au(100) as substrate, except for some very slight deviations within the experimental accuracy on the energy scale.

References

[1] D. L. Morel, A. K. Ghosh, T. Feng, E. L. Stogryn, P. E. Purwin, R. F. Shaw, and C. Fishman: *High-efficiency organic solar cells.* Appl. Phys. Lett. **32**, 495–497 (1978).

[2] C. W. Tang: *Two-layer organic photovoltaic cell.* Appl. Phys. Lett. **48**, 183–185 (1986).

[3] C. W. Tang and S. A. VanSlyke: *Organic electroluminescent diodes.* Appl. Phys. Lett. **51**, 913–915 (1987).

[4] S. R. Forrest: *The path to ubiquitous and low-cost organic electronic appliances on plastic.* Nature **428**, 911–918 (2004).

[5] J. Kido, M. Kimura, and K. Nagai: *Multilayer White Light-Emitting Organic Electroluminescent Device.* Science **267**, 1332–1334 (1995).

[6] Y. Sun, N. C. Giebink, H. Kanno, B. Ma, M. E. Thompson, and S. R. Forrest: *Management of singlet and triplet excitons for efficient white organic light-emitting devices.* Nature **440**, 908–912 (2006).

[7] K. Walzer, B. Maennig, M. Pfeiffer, and K. Leo: *Highly Efficient Organic Devices Based on Electrically Doped Transport Layers.* Chem. Rev. **107**, 1233–1271 (2007).

[8] N. Koch: *Organic Electronic Devices and Their Functional Interfaces.* ChemPhysChem **8**, 1438–1455 (2007).

[9] S. Reineke, F. Lindner, G. Schwartz, N. Seidler, K. Walzer, B. Lüssem, and K. Leo: *White organic light-emitting diodes with fluorescent tube efficiency.* Nature **459**, 234–238 (2009).

[10] N. Karl: *Charge carrier transport in organic semiconductors.* Synth. Met. **133-134**, 649–657 (2003).

[11] R. Schüppel, T. Dienel, K. Leo, and M. Hoffmann: *Time-resolved luminescence quenching in thin films of perylene-tetracarboxylic-dianhydride.* J. Lumin. **110**, 309–314 (2004).

[12] E. Engel, K. Leo, and M. Hoffmann: *Ultrafast relaxation and exciton–exciton annihilation in PTCDA thin films at high excitation densities.* Chem. Phys. **325**, 170–177 (2006).

[13] E. Engel, M. Koschorreck, K. Leo, and M. Hoffmann: *Ultrafast Relaxation in Quasi-One-Dimensional Organic Molecular Crystals.* Phys. Rev. Lett. **95**, 157403 (2005).

[14] A. Koma: *Molecular beam epitaxial growth of organic thin films.* Prog. Cryst. Growth Charact. Mater. **30**, 129–152 (1995).

[15] S. R. Forrest: *Ultrathin Organic Films Grown by Organic Molecular Beam Deposition and Related Techniques.* Chem. Rev. **97**, 1793–1896 (1997).

[16] N. Karl and C. Günther: *Structure and Ordering Principles of Ultrathin Organic Molecular Films on Surfaces of Layered Semiconductors Organic-on-Inorganic MBE.* Cryst. Res. Technol. **34**, 243–254 (1999).

[17] J. A. Last, D. E. Hooks, A. C. Hillier, and M. D. Ward: *The Physicochemical Origins of Coincident Epitaxy in Molecular Overlayers: Lattice Modeling vs Potential Energy Calculations.* J. Phys. Chem. B **103**, 6723–6733 (1999).

[18] D. E. Hooks, T. Fritz, and M. D. Ward: *Epitaxy and Molecular Organization on Solid Substrates.* Adv. Mater. **13**, 227–241 (2001).

[19] M. Eremtchenko, J. A. Schaefer, and F. S. Tautz: *Understanding and tuning the epitaxy of large aromatic adsorbates by molecular design.* Nature **425**, 602–605 (2003).

[20] F. Schreiber: *Organic molecular beam deposition: Growth studies beyond the first monolayer.* phys. stat. sol. (a) **201**, 1037–1054 (2004).

[21] N. R. Armstrong, D. M. Alloway, D. Schlettwein, A. Back, K. W. Nebesny, and P. Lee: *Organic Molecular Beam Epitaxy: Creation of Ordered Organic Thin Films and Organic-Organic Heterojunctions.* In: P. Somasundran and A. T. Hubbard (Eds.), *Encyclopedia of Surface and Colloid Science*, vol. 6, 4349–4363. Taylor & Francis Group, LLC, 2nd edn. (2006).

[22] H. Ishii, K. Sugiyama, E. Ito, and K. Seki: *Energy Level Alignment and Interfacial Electronic Structures at Organic/Metal and Organic/Organic Interfaces.* Adv. Mater. **11**, 605–625 (1999).

[23] A. Kahn, N. Koch, and W. Gao: *Electronic Structure and Electrical Properties of Interfaces between Metals and π-Conjugated Molecular Films.* J. Polym. Sci. Part B: Polym. Phys. **41**, 2529–2548 (2003).

[24] D. R. T. Zahn, G. N. Gavrila, and G. Salvan: *Electronic and Vibrational Spectroscopies Applied to Organic/Inorganic Interfaces.* Chem. Rev. **107**, 1161–1232 (2007).

[25] J. Hwang, A. Wan, and A. Kahn: *Energetics of metal–organic interfaces: New experiments and assessment of the field.* Mater. Sci. Eng., R **64**, 1–31 (2009).

[26] S. Braun, W. R. Salaneck, and M. Fahlman: *Energy-Level Alignment at Organic/Metal and Organic/Organic Interfaces.* Adv. Mater. **21**, 1450–1472 (2009).

[27] K. Kudo, M. Yamashina, and T. Moriizumi: *Field Effect Measurement of Organic Dye Films.* Jpn. J. Appl. Phys. **23**, 130 (1984).

[28] J. Zaumseil and H. Sirringhaus: *Electron and Ambipolar Transport in Organic Field-Effect Transistors.* Chem. Rev. **107**, 1296–1323 (2007).

[29] C. D. Simpson, J. Wu, M. D. Watson, and K. Müllen: *From graphite molecules to columnar superstructures – an exercise in nanoscience.* J. Mater. Chem. **14**, 494–504 (2004).

[30] T. Kircher and H.-G. Löhmannsröben: *Photoinduced charge recombination reactions of a perylene dye in acetonitrile.* Phys. Chem. Chem. Phys. **1**, 3987–3992 (1999).

[31] W. E. Ford, H. Hiratsuka, and P. V. Kamat: *Photochemistry of 3,4,9,10-Perylenetetracarboxylic Dianhydride Dyes. 4. Spectroscopic and Redox Properties of Oxidized and Reduced Forms of the Bis(2,5-di-*tert-butyl*phenyl)imide Derivative.* J. Phys. Chem. **93**, 6692–6696 (1989).

[32] H. Proehl, T. Dienel, R. Nitsche, and T. Fritz: *Formation of Solid-State Excitons in Ultrathin Crystalline Films of PTCDA: From Single Molecules to Molecular Stacks.* Phys. Rev. Lett. **93**, 097403 (2004).

[33] A. Hauschild, K. Karki, B. C. C. Cowie, M. Rohlfing, F. S. Tautz, and M. Sokolowski: *Molecular Distortions and Chemical Bonding of a Large π-Conjugated Molecule on a Metal Surface.* Phys. Rev. Lett. **94**, 036106 (2005).

[34] R. Temirov, S. Soubatch, A. Luican, and F. S. Tautz: *Free-electron-like dispersion in an organic monolayer film on a metal substrate.* Nature **444**, 350–353 (2006).

[35] A. Bannani, C. Bobisch, and R. Möller: *Ballistic Electron Microscopy of Individual Molecules.* Science **315**, 1824–1828 (2007).

[36] F. S. Tautz: *Structure and bonding of large aromatic molecules on noble metal surfaces: The example of PTCDA*. Prog. Surf. Sci. **82**, 479–520 (2007).

[37] T. Dienel, C. Loppacher, S. C. B. Mannsfeld, R. Forker, and T. Fritz: *Growth-Mode-Induced Narrowing of Optical Spectra of an Organic Adlayer*. Adv. Mater. **20**, 959–963 (2008).

[38] S. A. Burke, W. Ji, J. M. Mativetsky, J. M. Topple, S. Fostner, H.-J. Gao, H. Guo, and P. Grütter: *Strain Induced Dewetting of a Molecular System: Bimodal Growth of PTCDA on NaCl*. Phys. Rev. Lett. **100**, 186104 (2008).

[39] L. Kilian, A. Hauschild, R. Temirov, S. Soubatch, A. Schöll, A. Bendounan, F. Reinert, T.-L. Lee, F. S. Tautz, M. Sokolowski, and E. Umbach: *Role of Intermolecular Interactions on the Electronic and Geometric Structure of a Large π-Conjugated Molecule Adsorbed on a Metal Surface*. Phys. Rev. Lett. **100**, 136103 (2008).

[40] Y. Wang and C. Wöll: *Chemical reactions on metal oxide surfaces investigated by vibrational spectroscopy*. Surf. Sci. **603**, 1589–1599 (2009).

[41] T. Schmitz-Hübsch, F. Sellam, R. Staub, M. Törker, T. Fritz, C. Kübel, K. Müllen, and K. Leo: *Direct observation of organic–organic heteroepitaxy: perylene-tetracarboxylic-dianhydride on hexa-peri-benzocoronene on highly ordered pyrolytic graphite*. Surf. Sci. **445**, 358–367 (2000).

[42] F. Sellam, T. Schmitz-Hübsch, M. Toerker, S. Mannsfeld, H. Proehl, T. Fritz, K. Leo, C. Simpson, and K. Müllen: *LEED and STM investigations of organic–organic heterostructures grown by molecular beam epitaxy*. Surf. Sci. **478**, 113–121 (2001).

[43] S. C. B. Mannsfeld, K. Leo, and T. Fritz: *Line-on-Line Coincidence: A New Type of Epitaxy Found in Organic-Organic Heterolayers*. Phys. Rev. Lett. **94**, 056104 (2005).

[44] M. Möbus, N. Karl, and T. Kobayashi: *Structure of perylene-tetracarboxylic-dianhydride thin films on alkali halide crystal substrates*. J. Cryst. Growth **116**, 495–504 (1992).

[45] R. Goddard, M. W. Haenel, W. C. Herndon, C. Krüger, and M. Zander: *Crystallization of Large Planar Polycyclic Aromatic Hydrocarbons: The Molecular and Crystal Structures of Hexabenzo[*bc,ef,hi,kl,no,qr*]coronene and Benzo[1,2,3-*bc:*4,5,6-*b'c'*]dicoronene*. J. Am. Chem. Soc. **117**, 30–41 (1995).

[46] K. A. Kerr, J. P. Ashmore, and J. C. Speakman: *The crystal and molecular structure of quaterrylene: a redetermination.* Proc. R. Soc. Lond. A **344**, 199–215 (1975).

[47] M. E. Cass, H. S. Rzepa, D. R. Rzepa, and C. K. Williams: *The Use of the Free, Open-Source Program Jmol To Generate an Interactive Web Site To Teach Molecular Symmetry.* J. Chem. Educ. **82**, 1736–1740 (2005).

[48] M. Schwoerer and H. C. Wolf: *Organic Molecular Solids.* Wiley, Weinheim (2007).

[49] M. Pope and C. E. Swenberg: *Electronic Processes in Organic Crystals.* Oxford University Press, New York (1982).

[50] M. Wewer and F. Stienkemeier: *Laser-induced fluorescence spectroscopy of 3,4,9,10-perylenetetracarboxylic-dianhydrid in helium nanodroplets.* J. Chem. Phys. **120**, 1239–1244 (2004).

[51] M. Schneider: *Vibronische und optische Eigenschaften ultradünner organischer Filme am Beispiel PTCDA/Ag(111).* Dissertation, Bayerische Julius-Maximilians-Universität Würzburg (2002).

[52] M. Hoffmann: *Frenkel and Charge-Transfer Excitons in Quasi-One-Dimensional Molecular Crystals with Strong Intermolecular Orbital Overlap.* Dissertation, Technische Universität Dresden (2000).

[53] U. Gómez, M. Leonhardt, H. Port, and H. C. Wolf: *Optical properties of amorphous ultrathin films of perylene derivatives.* Chem. Phys. Lett. **268**, 1–6 (1997).

[54] M. Knupfer: *Exciton binding energies in organic semiconductors.* Appl. Phys. A **77**, 623–626 (2003).

[55] M. Kasha, H. R. Rawls, and M. Ashaf El-Bayoumi: *The exciton model in molecular spectroscopy.* Pure Appl. Chem. **11**, 371–392 (1965).

[56] M. Kasha: *Molecular Excitons in Small Aggregates.* In: B. DiBartolo (Ed.), *Spectroscopy of the Excited State*, 337–363. Plenum Press, New York (1976).

[57] H. Pröhl: *Optische Eigenschaften ultradünner PTCDA & TiOPc Einzel- und Heteroschichten: Vom Einzelmolekül zum molekularen Festkörper.* Dissertation, Technische Universität Dresden (2006).

[58] M. Hoffmann, K. Schmidt, T. Fritz, T. Hasche, V. M. Agranovich, and K. Leo: *The lowest energy Frenkel and charge-transfer excitons in quasi-one-dimensional structures: application to MePTCDI and PTCDA crystals.* Chem. Phys. **258**, 73–96 (2000).

[59] M. Hoffmann and Z. G. Soos: *Optical absorption spectra of the Holstein molecular crystal for weak and intermediate electronic coupling.* Phys. Rev. B **66**, 024305 (2002).

[60] M. Hoffmann: *Mixing of Frenkel and Charge-Transfer Excitons and Their Quantum Confinement in Thin Films.* In: V. M. Agranovich and G. F. Bassani (Eds.), *Electronic Excitations in Organic Multilayers and Organic Based Heterostructures*, vol. 31 of *Thin Films and Nanostructures*, chap. 5, 221–292. Elsevier, Amsterdam (2003).

[61] K. Schmidt: *Quantum confinement in linear molecular chains with strong mixing of Frenkel and charge-transfer excitons.* Phys. Lett. A **293**, 83–92 (2002).

[62] M. R. Philpott: *Planewise summation of point dipole–dipole interactions for some aromatic hydrocarbon crystals.* J. Chem. Phys. **58**, 588–594 (1973).

[63] H. Mauser: *Spectroscopy of Chemical Reaction Kinetics .1. Theory of Isosbestic Points.* Z. Naturforsch. **B23**, 1021–1025 (1968).

[64] M. Leonhardt, O. Mager, and H. Port: *Two-component optical spectra in thin PTCDA films due to the coexistence of α- and β-phase.* Chem. Phys. Lett. **313**, 24–30 (1999).

[65] A. B. Djurišić, T. Fritz, and K. Leo: *Modeling the optical constants of organic thin films: application to 3,4,9,10-perylenetetracarboxylic dianhydride (PTCDA).* Opt. Commun. **183**, 123–132 (2000).

[66] J. D. E. McIntyre and D. E. Aspnes: *Differential reflection spectroscopy of very thin surface films.* Surf. Sci. **24**, 417–434 (1971).

[67] J. D. Jackson: *Classical Electrodynamics.* Wiley, New York, 3rd edn. (1999).

[68] B. E. A. Saleh and M. C. Teich: *Fundamentals of Photonics.* Wiley Series in Pure and Applied Optics. Wiley, Hoboken, N.J., 2nd edn. (2007).

[69] L. D. Landau and E. M. Lifshitz: *Electrodynamics of Continuous Media*, vol. 8 of *Course of Theoretical Physics.* Pergamon Press, Oxford, England, 2nd edn. (1984).

[70] S. Selci, F. Ciccacci, G. Chiarotti, P. Chiaradia, and A. Cricenti: *Surface differential reflectivity spectroscopy of semiconductor surfaces.* J. Vac. Sci. Technol. A **5**, 327–332 (1987).

[71] R. J. Cole, B. G. Frederick, and P. Weightman: *Substrate dependence of adlayer optical response in reflectance anisotropy spectroscopy.* J. Vac. Sci. Technol. A **16**, 3088–3095 (1998).

[72] E. D. Palik (Ed.): *Handbook of Optical Constants of Solids I.* Academic Press, New York (1985).

[73] E. D. Palik (Ed.): *Handbook of Optical Constants of Solids II.* Academic Press, New York (1991).

[74] M. J. Weber (Ed.): *Handbook of Optical Materials.* CRC Press, Boca Raton (2003).

[75] R. Nitsche and T. Fritz: *Precise determination of the complex optical constant of mica.* Appl. Opt. **43**, 3263–3270 (2004).

[76] H. Proehl, R. Nitsche, T. Dienel, K. Leo, and T. Fritz: *In situ differential reflectance spectroscopy of thin crystalline films of PTCDA on different substrates.* Phys. Rev. B **71**, 165207 (2005).

[77] M. J. Dignam and M. Moskovits: *Optical Properties of Sub-monolayer Molecular Films.* J. Chem. Soc., Faraday Trans. 2 **69**, 56–64 (1973).

[78] R. Nitsche and T. Fritz: *Determination of model-free Kramers-Kronig consistent optical constants of thin absorbing films from just one spectral measurement: Application to organic semiconductors.* Phys. Rev. B **70**, 195432 (2004).

[79] R. Nitsche: *Optical properties of organic semiconductors: From (sub-) monolayers to crystalline films.* Dissertation, Technische Universität Dresden (2005).

[80] J. S. Toll: *Causality and the Dispersion Relation: Logical Foundations.* Phys. Rev. **104**, 1760–1770 (1956).

[81] D. W. Marquardt: *An Algorithm for Least-Squares Estimation of Nonlinear Parameters.* J. Soc. Indust. Appl. Math. **11**, 431–441 (1963).

[82] R. Forker: *Influence of the substrate on the optical properties of HBC nano-layers.* Diploma thesis, Technische Universität Dresden (2005).

[83] Y. Borensztein, C. Beitia, and R. G. Barrera: *Real-Time Investigation of Potassium Growth by Surface Differential Reflectance Spectroscopy.* phys. stat. sol. (a) **170**, 221–226 (1998).

[84] C. Beitia and Y. Borensztein: *Comparative Study of the Adsorption of Oxygen and Hydrogen on Si(111) 7 × 7 by Surface Differential Reflectance Spectroscopy.* phys. stat. sol. (a) **175**, 39–44 (1999).

[85] C. Beitia, Y. Borensztein, R. Lazzari, J. Nieto, and R. G. Barrera: *Substrate-induced multipolar resonances in supported free-electron metal spheres.* Phys. Rev. B **60**, 6018–6022 (1999).

[86] D. E. Aspnes, J. P. Harbison, A. A. Studna, and L. T. Florez: *Application of reflectance difference spectroscopy to molecular-beam epitaxy growth of GaAs and AlAs.* J. Vac. Sci. Technol. A **6**, 1327–1332 (1988).

[87] S. M. Scholz, F. Mertens, K. Jacobi, R. Imbihl, and W. Richter: *Reflectance anisotropy on a metal surface: rhodium (110).* Surf. Sci. **340**, L945–L948 (1995).

[88] P. Weightman, D. S. Martin, and A. Maunder: *RAS: a new probe of surface states.* J. Electron. Spectrosc. Relat. Phenom. **114-116**, 1069–1076 (2001).

[89] Y. Borensztein and N. Witkowski: *Optical response of clean and hydrogen-covered vicinal Si(001) 2 × 1 surfaces.* J. Phys.: Condens. Matter **16**, S4301–S4311 (2004).

[90] P. Chiaradia and R. Del Sole: *Differential-Reflectance Spectroscopy and Reflectance-Anisotropy Spectroscopy on Semiconductor Surfaces.* Surf. Rev. Lett. **6**, 517–528 (1999).

[91] Y. Borensztein: *Linear Optical Spectroscopies for Surface Studies.* Surf. Rev. Lett. **7**, 399–410 (2000).

[92] D. S. Martin and P. Weightman: *Reflection Anisotropy Spectroscopy: An Optical Probe of Surfaces and Interfaces.* Surf. Rev. Lett. **7**, 389–397 (2000).

[93] G. Chiarotti, P. Chiaradia, F. Arciprete, and C. Goletti: *Sum rules in surface differential reflectivity and reflectance anisotropy spectroscopies.* Appl. Surf. Sci. **175-176**, 777–782 (2001).

[94] P. Weightman: *The Potential of Reflection Anisotropy Spectroscopy as a Probe of Molecular Assembly on Metal Surfaces.* phys. stat. sol. (a) **188**, 1443–1453 (2001).

[95] P. Weightman, D. S. Martin, R. J. Cole, and T. Farrell: *Reflection anisotropy spectroscopy.* Rep. Prog. Phys. **68**, 1251–1341 (2005).

[96] K. L. Shaklee, F. H. Pollak, and M. Cardona: *Electroreflectance at a Semiconductor-Electrolyte Interface.* Phys. Rev. Lett. **15**, 883–885 (1965).

[97] J. Feinleib: *Electroreflectance in Metals.* Phys. Rev. Lett. **16**, 1200–1202 (1966).

[98] A. K. Ghosh: *Electroreflectance Spectra of Ge.* Solid State Commun. **4**, 565–568 (1966).

[99] B. O. Seraphin: *Electroreflectance Studies in GaAs.* J. Appl. Phys. **37**, 721–728 (1966).

[100] B. O. Seraphin and N. Bottka: *Band-Structure Analysis from Electro-Reflectance Studies.* Phys. Rev. **145**, 628–636 (1966).

[101] K. L. Shaklee, M. Cardona, and F. H. Pollak: *Electroreflectance and Spin-Orbit Splitting in III-V Semiconductors.* Phys. Rev. Lett. **16**, 48–50 (1966).

[102] J. D. Axe and R. Hammer: *Electroreflectance Spectra due to Free Carriers in Semiconductors.* Phys. Rev. **162**, 700–702 (1967).

[103] G. Chiarotti, G. Del Signore, and S. Nannarone: *Optical Detection of Surface States on Cleaved (111) Surfaces of Ge.* Phys. Rev. Lett. **21**, 1170–1172 (1968).

[104] G. Chiarotti, S. Nannarone, R. Pastore, and P. Chiaradia: *Optical Absorption of Surface States in Ultrahigh Vacuum Cleaved (111) Surfaces of Ge and Si.* Phys. Rev. B **4**, 3398–3402 (1971).

[105] R. E. Hummel, D. B. Dove, and J. A. Holbrook: *Optical Reflectivity Measurements on Alloys by Compositional Modulation.* Phys. Rev. Lett. **25**, 290–292 (1970).

[106] Y. Borensztein, W. L. Mochan, J. Tarriba, R. G. Barrera, and A. Tadjeddine: *Large Anisotropy in the Optical Reflectance of Ag(110) Single Crystals: Experiment and Theory.* Phys. Rev. Lett. **71**, 2334–2337 (1993).

[107] J.-K. Hansen, J. Bremer, and O. Hunderi: *Local-Field Effects at the Ag(110) and Cu(110) Surfaces Studied by Reflection Anisotropy Spectroscopy.* phys. stat. sol. (a) **170**, 271–277 (1998).

[108] D. S. Martin and P. Weightman: *Reflection anisotropy spectroscopy: a new probe of metal surfaces.* Surf. Interface Anal. **31**, 915–926 (2001).

[109] B. Sheridan, D. S. Martin, J. R. Power, S. D. Barrett, C. I. Smith, C. A. Lucas, R. J. Nichols, and P. Weightman: *Reflection Anisotropy Spectroscopy: A New Probe for the Solid-Liquid Interface.* Phys. Rev. Lett. **85**, 4618–4621 (2000).

[110] R. Forker and T. Fritz: *Optical differential reflectance spectroscopy of ultrathin epitaxial organic films.* Phys. Chem. Chem. Phys. **11**, 2142–2155 (2009).

[111] M. Horn-von Hoegen: *Growth of semiconductor layers studied by spot profile analysing low energy electron diffraction - Part I.* Z. Kristallogr. **214**, 591–629 (1999).

[112] S. Mannsfeld: *Ordering in weakly bound molecular layers: Organic-inorganic and organic-organic heteroepitaxy.* Dissertation, Technische Universität Dresden (2004).

[113] C. Günther: *Organische Molekularstrahlepitaxie: Ordnungsprinzipien großer Aromaten auf Schichthalbleitern.* Dissertation, Universität Stuttgart (1998).

[114] S. Mannsfeld: *Investigation of organic thin films with low energy electron diffraction.* Diploma thesis, Technische Universität Dresden (1999).

[115] L. J. Clarke: *Surface Crystallography: An Introduction to Low Energy Electron Diffraction.* Wiley, Chichester (1985).

[116] G. Binnig and H. Rohrer: *Scanning tunneling microscopy.* Helvetica Physica Acta **55**, 726–735 (1982).

[117] G. Binnig, H. Rohrer, C. Gerber, and E. Weibel: *Surface Studies by Scanning Tunneling Microscopy.* Phys. Rev. Lett. **49**, 57–61 (1982).

[118] P. K. Hansma and J. Tersoff: *Scanning tunneling microscopy.* J. Appl. Phys. **61**, R1–R23 (1987).

[119] G. Binnig and H. Rohrer: *Scanning tunneling microscopy.* IBM J. Res. Develop. **30**, 355–369 (1986).

[120] R. Wiesendanger: *Scanning Probe Microscopy and Spectroscopy: Methods and Applications.* Cambridge University Press (1994).

[121] I. Horcas, R. Fernández, J. M. Gómez-Rodríguez, J. Colchero, J. Gómez-Herrero, and A. M. Baro: *WSXM: A software for scanning probe microscopy and a tool for nanotechnology.* Rev. Sci. Instrum. **78**, 013705 (2007).

[122] D. Placencia, W. Wang, R. C. Shallcross, K. W. Nebesny, M. Brumbach, and N. R. Armstrong: *Organic Photovoltaic Cells Based On Solvent-Annealed, Textured Titanyl Phthalocyanine/C$_{60}$ Heterojunctions.* Adv. Funct. Mater. **19**, 1913–1921 (2009).

[123] M. A. Herman and H. Sitter: *Molecular Beam Epitaxy: Fundamentals and Current Status*, vol. 7 of *Springer Series in Materials Science*. Springer-Verlag, Berlin (1989).

[124] F. C. Frank and J. H. van der Merwe: *One-dimensional dislocations. I. Static theory.* Proc. R. Soc. London A **198**, 205–216 (1949).

[125] M. Volmer and A. Weber: *Keimbildung in übersättigten Gebilden.* Zeitschr. f. physik. Chemie (Leipzig) **119**, 277–301 (1926).

[126] I. N. Stranski and L. Krastanow: *Zur Theorie der orientierten Ausscheidung von Ionenkristallen aufeinander.* Monatsh. f. Chemie **71**, 351–364 (1938).

[127] F.-J. Meyer zu Heringdorf, M. C. Reuter, and R. M. Tromp: *Growth dynamics of pentacene thin films.* Nature **412**, 517–520 (2001).

[128] T. Fritz: *Molecular Architecture in Heteroepitaxially Grown Organic Thin Films.* Habilitation thesis, Technische Universität Dresden (1999).

[129] H. J. Lempka, S. Obenland, and W. Schmidt: *The Molecular Structure of* BOENTE*'s "Dicoronylene", as Deduced from PE and UV Spectroscopy.* Chem. Phys. **96**, 349–360 (1985).

[130] W. Hendel, Z. H. Khan, and W. Schmidt: *Hexa-peri-benzocoronene, A Candidate for the Origin of the Diffuse Interstellar Visible Absorption Bands?* Tetrahedron **42**, 1127–1134 (1986).

[131] E. Clar and W. Schmidt: *Correlations between Photoelectron and Ultraviolet Absorption Spectra of Polycyclic Hydrocarbons. The Perylene, Coronene and Bisanthene Series.* Tetrahedron **33**, 2093–2097 (1977).

[132] E. Clar and W. Schmidt: *Correlations between Photoelectron and Ultraviolet Absorption Spectra of Polycyclic Hydrocarbons. The Terrylene and Peropyrene Series.* Tetrahedron **34**, 3219–3224 (1978).

[133] R. Forker, D. Kasemann, T. Dienel, C. Wagner, R. Franke, K. Müllen, and T. Fritz: *Electronic Decoupling of Aromatic Molecules from a Metal by an Atomically Thin Organic Spacer.* Adv. Mater. **20**, 4450–4454 (2008).

[134] H. Proehl, M. Toerker, F. Sellam, T. Fritz, K. Leo, C. Simpson, and K. Müllen: *Comparison of ultraviolet photoelectron spectroscopy and scanning tunneling spectroscopy measurements on highly ordered ultra-thin films of hexa-peri-hexabenzocoronene on Au(111)*. Phys. Rev. B **63**, 205409 (2001).

[135] R. Forker, T. Dienel, T. Fritz, and K. Müllen: *Optical evidence for substrate-induced growth of ultrathin hexa-peri-hexabenzocoronene films on highly oriented pyrolytic graphite*. Phys. Rev. B **74**, 165410 (2006).

[136] Y. Maruyama, T. Iwaki, T. Kajiwara, I. Shirotani, and H. Inokuchi: *Molecular Orientation and Absorption Spectra of Quaterrylene Evaporated Film*. Bull. Chem. Soc. Jpn. **43**, 1259–1261 (1970).

[137] R. Hayakawa, M. Petit, Y. Wakayama, and T. Chikyow: *Growth of quaterrylene thin films on a silicon dioxide surface using vacuum deposition*. Org. Electron. **8**, 631–634 (2007).

[138] R. Hayakawa, M. Petit, Y. Wakayama, and T. Chikyow: *Evolution of Quaterrylene Thin Films on a Silicon Dioxide Surface Using an Ultra-slow Deposition Technique*. J. Phys. Chem. C **111**, 18703–18707 (2007).

[139] R. Hayakawa, M. Petit, T. Chikyow, and Y. Wakayama: *Analysis of carrier transport in quaterrylene thin film transistors formed by ultraslow vacuum deposition*. J. Appl. Phys. **104**, 024506 (2008).

[140] R. Hayakawa, M. Petit, T. Chikyow, and Y. Wakayama: *Interface engineering for molecular alignment and device performance of quaterrylene thin films*. Appl. Phys. Lett. **93**, 153301 (2008).

[141] W. Mönch: *Semiconductor Surfaces and Interfaces*. Springer, Berlin, 3rd edn. (2001).

[142] L. Segev, A. Salomon, A. Natan, D. Cahen, L. Kronik, F. Amy, C. K. Chan, and A. Kahn: *Electronic structure of Si(111)-bound alkyl monolayers: Theory and experiment*. Phys. Rev. B **74**, 165323 (2006).

[143] P. W. Anderson: *Localized Magnetic States in Metals*. Phys. Rev. **124**, 41–53 (1961).

[144] D. M. Newns: *Self-Consistent Model of Hydrogen Chemisorption*. Phys. Rev. **178**, 1123–1135 (1969).

[145] F. S. Tautz, M. Eremtchenko, J. A. Schaefer, M. Sokolowski, V. Shklover, and E. Umbach: *Strong electron-phonon coupling at a metal/organic interface: PTCDA/Ag(111)*. Phys. Rev. B **65**, 125405 (2002).

[146] R. Franke, S. Franke, C. Wagner, T. Dienel, T. Fritz, and S. C. B. Mannsfeld: *Epitaxial nanolayers of quaterrylene: Influence of the substrate on the growth of the first and second monolayers.* Appl. Phys. Lett. **88**, 161907 (2006).

[147] R. Franke: *Epitaxial nanolayers of large organic molecules: Quaterrylenes on organic and inorganic substrates.* Dissertation, Technische Universität Dresden (2007).

[148] S. C. B. Mannsfeld and T. Fritz: *Understanding organic–inorganic heteroepitaxial growth of molecules on crystalline substrates: Experiment and theory.* Phys. Rev. B **71**, 235405 (2005).

[149] S. C. B. Mannsfeld and T. Fritz: *Advanced Modelling of Epitaxial Ordering of Organic Layers on Crystalline Surfaces.* Mod. Phys. Lett. B **20**, 585–605 (2006).

[150] F. Jäckel, M. D. Watson, K. Müllen, and J. P. Rabe: *Tunneling through nanographene stacks.* Phys. Rev. B **73**, 045423 (2006).

[151] D. Kasemann, C. Wagner, R. Forker, T. Dienel, K. Müllen, and T. Fritz: *Line-on-Line Organic–Organic Heteroepitaxy of Quaterrylene on Hexaperi-hexabenzocoronene on Au(111).* Langmuir **25**, 12569–12573 (2009).

[152] M. Keil, P. Samorí, D. A. dos Santos, J. Bigerson, R. Friedlein, A. Dkhissi, M. Watson, K. Müllen, J. L. Brédas, J. P. Rabe, and W. R. Salaneck: *High levels of alkali-metal storage in thin films of hexa-perihexabenzocoronene.* J. Chem. Phys. **116**, 10854–10860 (2002).

[153] M. Keil, P. Samorí, D. A. dos Santos, T. Kugler, S. Stafström, J. D. Brand, K. Müllen, J. L. Brédas, J. P. Rabe, and W. R. Salaneck: *Influence of the Morphology on the Electronic Structure of Hexa-perihexabenzocoronene Thin Films.* J. Phys. Chem. B **104**, 3967–3975 (2000).

[154] M. Adachi and Y. Nagao: *Design of Near-Infrared Dyes Based on π-Conjugation System Extension 2. Theoretical Elucidation of Framework Extended Derivatives of Perylene Chromophore.* Chem. Mater. **13**, 662–669 (2001).

[155] T. M. Halasinski, J. L. Weisman, R. Ruiterkamp, T. J. Lee, F. Salama, and M. Head-Gordon: *Electronic Absorption Spectra of Neutral Perylene ($C_{20}H_{12}$), Terrylene ($C_{30}H_{16}$), and Quaterrylene ($C_{40}H_{20}$) and Their Positive and Negative Ions: Ne Matrix-Isolation Spectroscopy and Time-Dependent Density Functional Theory Calculations.* J. Phys. Chem. A **107**, 3660–3669 (2003).

[156] X. H. Qiu, G. V. Nazin, and W. Ho: *Vibrationally Resolved Fluorescence Excited with Submolecular Precision.* Science **299**, 542–546 (2003).

[157] E. Ćavar, M.-C. Blüm, M. Pivetta, F. Patthey, M. Chergui, and W.-D. Schneider: *Fluorescence and Phosphorescence from Individual C_{60} Molecules Excited by Local Electron Tunneling.* Phys. Rev. Lett. **95**, 196102 (2005).

[158] S. Picozzi, A. Pecchia, M. Gheorghe, A. Di Carlo, P. Lugli, B. Delley, and M. Elstner: *Schottky barrier height at an organic/metal junction: A first-principles study of PTCDA/X (X=Al, Ag) contacts.* Phys. Rev. B **68**, 195309 (2003).

[159] M. Eremtchenko, D. Bauer, J. A. Schaefer, and F. S. Tautz: *Polycyclic aromates on close-packed metal surfaces: functionalization, molecular chemisorption and organic epitaxy.* New J. Phys. **6**, 4 (2004).

[160] Y. Zou, L. Kilian, A. Schöll, T. Schmidt, R. Fink, and E. Umbach: *Chemical bonding of PTCDA on Ag surfaces and the formation of interface states.* Surf. Sci. **600**, 1240–1251 (2006).

[161] S. Duhm, A. Gerlach, I. Salzmann, B. Bröker, R. L. Johnson, F. Schreiber, and N. Koch: *PTCDA on Au(111), Ag(111) and Cu(111): Correlation of interface charge transfer to bonding distance.* Org. Electron. **9**, 111–118 (2008).

[162] E. Kawabe, H. Yamane, R. Sumii, K. Koizumi, Y. Ouchi, K. Seki, and K. Kanai: *A role of metal d-band in the interfacial electronic structure at organic/metal interface: PTCDA on Au, Ag and Cu.* Org. Electron. **9**, 783–789 (2008).

[163] P. C. Rusu, G. Giovannetti, C. Weijtens, R. Coehoorn, and G. Brocks: *Work Function Pinning at Metal–Organic Interfaces.* J. Phys. Chem. C **113**, 9974–9977 (2009).

[164] T. Schmitz-Hübsch, T. Fritz, F. Sellam, R. Staub, and K. Leo: *Epitaxial growth of 3,4,9,10-perylene-tetracarboxylic-dianhydride on Au(111): A STM and RHEED study.* Phys. Rev. B **55**, 7972–7976 (1997).

[165] S. Mannsfeld, M. Toerker, T. Schmitz-Hübsch, F. Sellam, T. Fritz, and K. Leo: *Combined LEED and STM study of PTCDA growth on reconstructed Au(111) and Au(100) single crystals.* Org. Electron. **2**, 121–134 (2001).

[166] I. Chizhov, A. Kahn, and G. Scoles: *Initial growth of 3,4,9,10-perylene-tetracarboxylic-dianhydride (PTCDA) on Au(111): a scanning tunneling microscopy study.* J. Cryst. Growth **208**, 449–458 (2000).

[167] T. Wagner, A. Bannani, C. Bobisch, H. Karacuban, M. Stöhr, M. Gabriel, and R. Möller: *Growth of 3,4,9,10-perylenetetracarboxylic-dianhydride crystallites on noble metal surfaces.* Org. Electron. **5**, 35–43 (2004).

[168] L. Kilian, E. Umbach, and M. Sokolowski: *Molecular beam epitaxy of organic films investigated by high resolution low energy electron diffraction (SPA-LEED): 3,4,9,10-perylenetetracarboxylicacid-dianhydride (PTCDA) on Ag(111).* Surf. Sci. **573**, 359–378 (2004).

[169] L. Kilian, E. Umbach, and M. Sokolowski: *A refined structural analysis of the PTCDA monolayer on the reconstructed Au(111) surface – "Rigid or distorted carpet?".* Surf. Sci. **600**, 2633–2643 (2006).

[170] J. Ikonomov, O. Bauer, and M. Sokolowski: *Highly ordered thin films of perylene-3,4,9,10-tetracarboxylic acid dianhydride (PTCDA) on Ag(100).* Surf. Sci. **602**, 2061–2068 (2008).

[171] P. Fenter, F. Schreiber, L. Zhou, P. Eisenberger, and S. R. Forrest: *In situ studies of morphology, strain, and growth modes of a molecular organic thin film.* Phys. Rev. B **56**, 3046–3053 (1997).

[172] A. J. Lovinger, S. R. Forrest, M. L. Kaplan, P. H. Schmidt, and T. Venkatesan: *Structural and morphological investigation of the development of electrical conductivity in ion-irradiated thin films of an organic material.* J. Appl. Phys. **55**, 476–482 (1984).

[173] S. R. Forrest, M. L. Kaplan, and P. H. Schmidt: *Organic-on-inorganic semiconductor contact barrier diodes. I. Theory with applications to organic thin films and prototype devices.* J. Appl. Phys. **55**, 1492–1507 (1984).

[174] T. Ogawa, K. Kuwamoto, S. Isoda, T. Kobayashi, and N. Karl: *3,4:9,10-Perylenetetracarboxylic dianhydride (PTCDA) by electron crystallography.* Acta Cryst. B **55**, 123–130 (1999).

[175] T. Schmitz-Hübsch, T. Fritz, R. Staub, A. Back, N. R. Armstrong, and K. Leo: *Structure of 3,4,9,10-perylene-tetracarboxylic-dianhydride grown on reconstructed and unreconstructed Au(100).* Surf. Sci. **437**, 163–172 (1999).

[176] R. Nitsche, H. Proehl, and T. Fritz: *Differential reflection spectroscopy of ultrathin highly ordered films of PTCDA on Au(111).* In: F. Charra, V. M. Agranovich, and F. Kajzar (Eds.), *Organic Nanophotonics*, vol. 100 of *NATO SCIENCE SERIES: II: Mathematics, Physics and Chemistry*, 103–117. Kluwer Academic Publisher, Dordrecht (2003).

[177] R. Forker, C. Golnik, G. Pizzi, T. Dienel, and T. Fritz: *Optical absorption spectra of ultrathin PTCDA films on gold single crystals: Charge transfer beyond the first monolayer.* Org. Electron. **10**, 1448–1453 (2009).

[178] L. Romaner, G. Heimel, J.-L. Brédas, A. Gerlach, F. Schreiber, R. L. Johnson, J. Zegenhagen, S. Duhm, N. Koch, and E. Zojer: *Impact of Bidirectional Charge Transfer and Molecular Distortions on the Electronic Structure of a Metal-Organic Interface.* Phys. Rev. Lett. **99**, 256801 (2007).

[179] L. Romaner, D. Nabok, P. Puschnig, E. Zojer, and C. Ambrosch-Draxl: *Theoretical study of PTCDA adsorbed on the coinage metal surfaces, Ag(111), Au(111) and Cu(111).* New J. Phys. **11**, 053010 (2009).

[180] C. Golnik: *Optische Absorptionsspektroskopie von ultradünnen organischen Filmen: PTCDA auf den Metalleinkristallen Au(111), Ag(111) und Al(111).* Diploma thesis, Technische Universität Dresden (2008).

[181] T. Dienel: *Molekulare Systeme im Wechselspiel von Struktur und Ladung.* Dissertation, Technische Universität Dresden (2009).

[182] E. V. Tsiper, Z. G. Soos, W. Gao, and A. Kahn: *Electronic polarization at surfaces and thin films of organic molecular crystals: PTCDA.* Chem. Phys. Lett. **360**, 47–52 (2002).

[183] S. K. M. Henze, O. Bauer, T.-L. Lee, M. Sokolowski, and F. S. Tautz: *Vertical bonding distances of PTCDA on Au(111) and Ag(111): Relation to the bonding type.* Surf. Sci. **601**, 1566–1573 (2007).

[184] A. Gerlach, S. Sellner, F. Schreiber, N. Koch, and J. Zegenhagen: *Substrate-dependent bonding distances of PTCDA: A comparative x-ray standing-wave study on Cu(111) and Ag(111).* Phys. Rev. B **75**, 045401 (2007).

[185] N. Hiroshiba, R. Hayakawa, M. Petit, T. Chikyow, K. Matsuishi, and Y. Wakayama: *Growth and structural characterization of molecular superlattice of quaterrylene and N,N'-dioctyl-3,4,9,10-perylenedicarboximide.* Org. Electron. **10**, 1032–1036 (2009).

List of Figures

List of Tables

Publications

Many substantial aspects of this dissertation have been published in peer-reviewed scientific journals and/or presented at international conferences. In the following, all hitherto realized contributions are listed chronologically.

Articles

A1 R. Forker, T. Dienel, T. Fritz, and K. Müllen: *Optical evidence for substrate-induced growth of ultrathin hexa-peri-hexabenzocoronene films on highly oriented pyrolytic graphite.* Phys. Rev. B **74**, 165410 (2006). `DOI:10.1103/PhysRevB.74.165410`

A2 C. Wagner, R. Franke, T. Dienel, R. Forker, R. Jacob, and T. Fritz: *Degradation and segregation: Thermal stability and highly ordered epitaxial thin films of large aromatic molecules.* Appl. Phys. Lett. **91**, 113111 (2007). `DOI:10.1063/1.2779100`

A3 T. Dienel, R. Forker, K. Leo, and T. Fritz: *Optical Differential Reflectance Spectroscopy of Molecular Thin Films on a Metal: Evidence for Strong Oscillator Strength Increase.* J. Phys. Chem. C **111**, 14593-14596 (2007). `DOI:10.1021/jp075128i`

A4 T. Dienel, H. Proehl, R. Forker, K. Leo, and T. Fritz: *Metal-Induced Photoluminescence Quenching of Organic Molecular Crystals.* J. Phys. Chem. C **112**, 9056-9060 (2008). `DOI:10.1021/jp709718t`

A5 T. Dienel, C. Loppacher, S. C. B. Mannsfeld, R. Forker, and T. Fritz: *Growth-Mode-Induced Narrowing of Optical Spectra of an Organic Adlayer.* Adv. Mater. **20**, 959-963 (2008). `DOI:10.1002/adma.200701684`

A6 R. Forker, D. Kasemann, T. Dienel, C. Wagner, R. Franke, K. Müllen, and T. Fritz: *Electronic Decoupling of Aromatic Molecules from a Metal by an Atomically Thin Organic Spacer.* Adv. Mater. **20**, 4450-4454 (2008). `DOI:10.1002/adma.200801112`

A7 (Invited Review) R. Forker and T. Fritz: *Optical differential reflectance spectroscopy of ultrathin epitaxial organic films.* Phys. Chem. Chem. Phys. **11**, 2142-2155 (2009). `DOI:10.1039/b814628d`

A8 R. Forker, C. Golnik, G. Pizzi, T. Dienel, and T. Fritz: *Optical absorption spectra of ultrathin PTCDA films on gold single crystals: Charge transfer beyond the first monolayer.* Org. Electron. **10**, 1448-1453 (2009). `DOI:10.1016/j.orgel.2009.08.005`

A9 D. Kasemann, C. Wagner, R. Forker, T. Dienel, K. Müllen, and T. Fritz: *Line-on-Line Organic–Organic Heteroepitaxy of Quaterrylene on Hexa-peri-hexabenzocoronene on Au(111).* Langmuir **25**, 12569-12573 (2009). `DOI:10.1021/la901760j`

A10 C. Wagner, D. Kasemann, C. Golnik, R. Forker, M. Esslinger, K. Müllen, and T. Fritz: *Repulsion between molecules on a metal: Monolayers and submonolayers of hexa-peri-hexabenzocoronene on Au(111).* Phys. Rev. B (accepted, 2009).

A11 A. A. Levin, T. Leisegang, R. Forker, M. Koch, D. C. Meyer, and T. Fritz: *Preparation and crystallographic characterization of crystalline modifications of 3,4:9,10-perylenetetracarboxylic dianhydride (PTCDA), $C_{24}H_8O_6$ at room temperature.* Cryst. Res. Technol. (accepted, 2010).

A12 T. Dienel, A. Krause, R. Alle, R. Forker, K. Meerholz, and T. Fritz: *Alkali metal doped organic molecules on insulators: Charge impact on the optical properties.* Submitted to Adv. Mater. (2010).

Talks

T1 R. Forker, T. Dienel, K. Müllen, and T. Fritz: *Optical Evidence for Substrate Induced Growth of Ultra-thin Hexa-peri-hexabenzocoronene Layers on HOPG.* DPG Frühjahrstagung, 26–31 March 2006 in Dresden, Germany.

T2 R. Forker, T. Dienel, K. Müllen, and T. Fritz: *Optical Spectroscopy of Ultrathin Stacked Nanolayers Grown by Multiple Organic Heteroepitaxy.* DPG Frühjahrstagung, 26–30 March 2007 in Regensburg, Germany.

T3 D. Kasemann, R. Franke, R. Forker, and T. Fritz: *Epitaxial Heterolayers of Quaterrylene and HBC on Au(111).* DPG Frühjahrstagung, 26–30 March 2007 in Regensburg, Germany.

T4 R. Forker: *Optical Spectroscopy of Stacked Organic Heterolayers.* Minerva School "Unique Molecular Effects in Electronic Materials and Devices", 29 April – 4 May 2007 in Safed, Israel.

T5 T. Dienel, R. Forker, A. Krause, and T. Fritz: *Optical Spectroscopy of Organic Interfaces with Submonolayer Sensitivity.* International Conference on Materials for Advanced Technologies (ICMAT), 1–6 July 2007 in Singapore.

T6 R. Forker, G. Pizzi, C. Golnik, T. Dienel, and T. Fritz: *Direct Optical Observation of Charge Transfer between Metals and Epitaxial Organic Layers.* DPG Frühjahrstagung, 25–29 February 2008 in Berlin, Germany.

T7 T. Dienel, A. Krause, R. Forker, and T. Fritz: *Charged Molecules on Insulators: Optical Spectroscopy of PTCDA Ions.* DPG Frühjahrstagung, 25–29 February 2008 in Berlin, Germany.

T8 R. Forker, G. Pizzi, T. Dienel, C. Golnik, and T. Fritz: *Optical Observation of Charge Transfer between Metals and Epitaxial Organic Layers.* Eighth International Symposium on Functional π-Electron Systems (Fπ8), 21–25 July 2008 in Graz, Austria.

T9 R. Forker, C. Golnik, C. Wagner, M. Esslinger, and T. Fritz: *In-situ optical spectroscopy of ultrathin quaterrylene films epitaxially grown on graphite and mica.* DPG Frühjahrstagung, 22–27 March 2009 in Dresden, Germany.

T10 C. Wagner, D. Kasemann, M. Esslinger, R. Forker, C. Golnik, and T. Fritz: *A quantitative model for the monolayer growth of hydrocarbons on noble metals: HBC on Ag(111) and Au(111).* DPG Frühjahrstagung, 22–27 March 2009 in Dresden, Germany.

T11 R. Forker: *Electronic Coupling Effects and Charge Transfer between Organic Molecules and Metal Surfaces.* Invited talk given at the Seminar zur Oberflächenforschung, Institut für Physikalische und Theoretische Chemie, Universität Bonn, 30 October 2009 in Bonn, Germany.

Posters

P1 R. Forker, T. Dienel, R. Nitsche, K. Müllen, T. Fritz, and K. Leo: *Influence of the Substrate on the Optical Properties of Molecular HBC-Layers.* DPG Frühjahrstagung, 4–9 March 2005 in Berlin, Germany.

P2 T. Dienel, R. Forker, K. Müllen, and T. Fritz: *Optical Evidence for Substrate Induced Growth of Ultra-thin Hexa*-peri-*hexabenzocoronene Layers on HOPG*. Seventh International Symposium on Functional π-Electron Systems (Fπ7), 15–20 May 2006 in Osaka, Japan.

P3 R. Forker, T. Dienel, K. Müllen, and T. Fritz: *Optical Spectroscopy of Ultrathin Stacked Nanolayers Grown by Multiple Organic Heteroepitaxy*. 383$^{\text{rd}}$ WE-Heraeus-Seminar "Physics of highly ordered organic interfaces and layers", 22–24 January 2007 in Bad Honnef, Germany.

P4 D. Kasemann, R. Franke, C. Wagner, R. Forker, and T. Fritz: *Epitaxial Heterolayers of Quaterrylene and HBC on Au(111)*. 383$^{\text{rd}}$ WE-Heraeus-Seminar "Physics of highly ordered organic interfaces and layers", 22–24 January 2007 in Bad Honnef, Germany.

P5 C. Wagner, R. Franke, S. Franke, T. Dienel, R. Forker, and T. Fritz: *Ordering of large aromatic hydrocarbons on surfaces: The growth of quaterrylene derivatives*. International Conference on Nano Science and Technology (ICN+T), 2–6 July 2007 in Stockholm, Sweden.

P6 C. Wagner, D. Kasemann, R. Forker, M. Esslinger, and T. Fritz: *Tailoring and properties of highly ordered organic–organic heterojunctions: Epitaxy of large aromatic hydrocarbons*. Max Bergmann Seminar, 4–6 November 2008 in Dresden, Germany.

P7 A. Krause, T. Dienel, R. Forker, and T. Fritz: *First optical investigation of the charged states of PTCDA in solid state*. DPG Frühjahrstagung, 22–27 March 2009 in Dresden, Germany.

P8 C. Golnik, R. Forker, and T. Fritz: *Optical observation of charged organic molecules on metal surfaces*. DPG Frühjahrstagung, 22–27 March 2009 in Dresden, Germany.

Danksagung

Gern möchte ich an dieser Stelle einige Dankesworte an diejenigen richten, auf deren Unterstützung ich während des Entstehens dieser Dissertation habe bauen können. Ich danke im Besonderen:

- Prof. Dr. Karl Leo für die Betreuung meiner Arbeit. Seine Leitung ermöglichte stets eine ausgezeichnete Infrastruktur und eine freundliche Arbeitsatmosphäre am Institut für Angewandte Photophysik. Weiterhin haben er sowie Prof. Dr. Clemens Laubschat und PD Dr. Torsten Fritz durch ihren Zuspruch wesentlich zu meiner Aufnahme in die Promotionsförderung der Studienstiftung des deutschen Volkes beigetragen.

- Prof. Dr. Moritz Sokolowski für die bereitwillige Übernahme des zweiten Gutachtens meiner Dissertation und das damit verbundene Interesse an dieser Arbeit.

- PD Dr. Torsten Fritz für die exzellente unmittelbare Betreuung meiner Arbeit, für ausführliche, hilfreiche Diskussionen und Anregungen sowie für seine freundschaftliche Auffassung des kollegialen Miteinanders in der Arbeitsgruppe OMBE unter seiner Leitung.

- Prof. Dr. Neal R. Armstrong für die Einladung zu einem Forschungsaufenthalt an der University of Arizona in Tucson (USA). Die herzliche Gastfreundschaft und die erstklassige fachliche Betreuung, die mir von September bis Dezember 2007 zuteil wurden, möchte ich besonders betonen. Von den dortigen Kollegen seien Dr. Kenneth W. Nebesny, Dr. Paul A. Lee und Diogenes Placencia hervorgehoben, letzterer auch für sein Anliegen, mir den amerikanischen Lebensstil näher zu bringen.

- Meinen Kollegen in der Arbeitsgruppe OMBE für inspirierende, vielseitige Ideen und Experimente sowie für zahlreiche fachübergreifende Gespräche und Exkursionen, die oft über das rein Fachliche hinausgingen. Zu meinen Mitstreitern zählen bzw. zählten Dr. Thomas Dienel, Moritz Eßlinger, Dr. Robert Franke, Sebastian Franke, Christian Golnik, Rainer Jacob, Daniel Kasemann, Andreas Krause, Dr. Stefan C. B. Mannsfeld, Dr. Robert Nitsche, Dr. Holger Pröhl und Christian Wagner. Meine

Mithilfe bei der Betreuung der Diplomarbeiten von Christian, Daniel und Andreas sowie des Forschungsaufenthaltes von Giovanni Pizzi wurde mit großem Elan und Begeisterungsfähigkeit im Laboralltag honoriert, was die Zusammenarbeit ausgesprochen angenehm und ergiebig gestaltete.

○ Den hilfsbereiten Mitarbeitern des **iapp** , denen die sehr wohlwollende, entgegenkommende Stimmung dort zu verdanken ist. In guter Erinnerung bleiben mir vor allem Dr. Susanne C. Schneider (verheiratet Kehr), Oliver Mieth und Selina Olthof, zu deren Freunden ich mich rechnen darf.

○ Meiner Familie und meinen Freunden für ihre Geduld und ihr Vertrauen, welche als Grundlage und Ansporn unschätzbare Bedeutung besitzen.

○ Der Studienstiftung des deutschen Volkes für die dreijährige Unterstützung im Rahmen eines Promotionsstipendiums.

Abschließend ist es mir eine große Freude, meiner Freundin Andrea für ihre Liebe und ihr Bestreben, meine Leidenschaft für physikalische und technische Themen nachzuvollziehen, besonders herzlich zu danken.

Erklärung

Diese Dissertation wurde am Institut für Angewandte Physik/Photophysik der Fakultät Mathematik und Naturwissenschaften an der Technischen Universität Dresden unter wissenschaftlicher Betreuung von Prof. Dr. Karl Leo angefertigt.

Hiermit versichere ich, dass ich die vorliegende Arbeit ohne unzulässige Hilfe Dritter und ohne Benutzung anderer als der angegebenen Hilfsmittel angefertigt habe; die aus fremden Quellen direkt oder indirekt übernommenen Gedanken sind als solche kenntlich gemacht. Die Arbeit wurde bisher weder im Inland noch im Ausland in gleicher oder ähnlicher Form einer anderen Prüfungsbehörde vorgelegt.

Ich versichere weiterhin, dass bislang keine Promotionsverfahren stattgefunden haben.

Ich erkenne die Promotionsordnung der Fakultät Mathematik und Naturwissenschaften an der Technischen Universität Dresden vom 20.03.2000, in der Fassung der vom Fakultätsrat am 19.06.2002 und 12.07.2002 beschlossenen und mit Erlass des Sächsischen Staatsministeriums für Wissenschaft und Kunst vom 18.03.2003 genehmigten Änderungen gemäß Satzung vom 16.04.2003 sowie gemäß der Änderungssatzung vom 17.07.2008, an.

Roman Forker
Dresden, den 15.09.2009